Hybrid FRET Systems for Energy Harvesting Applications

Thesis Submitted to the Faculty of Science,

University of Calicut in partial fulfillment of the requirements

for the Degree of

DOCTOR OF PHILOSOPHY

By

Rajita Ramanarayanan

Under the guidance of

Dr. Sindhu. S

Department of Nanoscience and Technology

University of Calicut

Certificate

This is to certify that the thesis entitled **"Hybrid FRET Systems for Energy Harvesting Applications"** is a bona-fide record of research work carried out by Smt. Rajita Ramanarayanan, under my supervision in partial fulfillment of the requirements for the award of the degree of Doctor of Philosophy in Nanoscience and Technology of the University of Calicut. The plagiarism check is carried out and this work or part thereof has not been presented before for the award of any other degree. Also certify that she has incorporated the suggestions and corrections pointed out by the examiners in the revised thesis.

Dr. Sindhu .S (Supervising Guide)
Assistant Professor Department of Nanoscience and Technology (DNST), University of Calicut

DECLARATION

Certified that the thesis bound herewith is an authentic record of the work on **"Hybrid FRET Systems for Energy Harvesting Application"** carried out by me under the supervision of Dr. Sindhu S, Assistant Professor, Department of Nanoscience and Technology, University of Calicut in partial fulfilment of the requirements for the award of the degree of the Doctor of Philosophy of the University of Calicut, and further that no part thereof has been presented before for any other degree.

Calicut University

Rajita Ramanarayanan

Acknowledgements

Iam grateful to the Faculty Development Program (FDP) programme of UGC for funding my research. This PhD journey was truly an interesting and enriching experience for me which was only possible through the guidance and support I have received from many people.

First of all, I express my sincere gratitude to my supervisor Dr Sindhu.S for providing me the opportunity to work in solar cells, for the continuous feedback, encouragement and confidence in my abilities throughout my work. It was a great opportunity working with you Madam.

I express my gratitude to the office staff Dhanya, Sangeeta and Thasneema of Department of Nanoscience and Technology for their help during my research period. I would also like to acknowledge my colleagues and students of Government College, Koyilandy for their concern and support.

Many thanks to my labmates Niveditha, Nijisha, Bhabhina, Darsana, Jyothilakshmi and Jabeen for their help and an enjoyable working atmosphere. Their enthusiasm and warmth helped me sail through difficult situations in my Phd Journey.

I would also like to thank the MTech students of Department of Nanoscience and Technology for the wonderful time spent with them. Special thanks to Sreed Sharma, PhD scholar, CIDET, Mexico who helped me with the XPS analysis. I also express my gratitude to the research scholars of Physics Department for their help in characterisations.

To my parents Ramanarayanan and Ramani for their love, encouragement and unconditional support to all endeavours of my life. To my dear sister Rashmi and nephew Aromal whose endless love and encouragement helped me in keeping my spirits high all these years. Lastly to my husband Arun and dear son Karthik for their love, understanding and constant support in completing this doctoral work.

Table of Contents

List of Figures

List of Tables

List of Abbreviations

1. DSSC	Dye Sensitized Solar Cells
2. QD	Quantum Dot
3. FRET	Förster Resonance energy transfer
4. QY	Quantum Yield
5. UV-Vis	UV-Visible Spectroscopy
6. PL	Photoluminescence
7. FTIR	Fourier Transform Infrared
8. DLS	Dynamic Light Scattering
9. XPS	X-ray Photon Spectroscopy
10. XRD	X-ray diffraction
11. SEM	Scanning Electron Microscopy
12. EDAX	Energy Dispersive X-ray
13. TEM	Transmission Electron Microscopy
14. SAED	Selected Area Electron Diffraction
15. EIS	Electrochemical Impedence Spectroscopy
16. TCSPC	Time Correlated Single Photon Counting
17. Ag	Silver
18. Au	Gold
19. Pt	Platinum
20. I^-	Iodide
21. I^-_3	Iodide
22. $HAuCl_4$	Chloroauric acid

23. Methylene Blue	MB
24. N719	Di-tetrabutylammonium cis-bis(isothiocyanato)bis(2,2′-bipyridyl-4, 4′-dicarboxylato) ruthenium (II)
25. F.T.O	Fluorine doped Tin Oxide
26. TCO	Transparent Conducting Oxide
27. TiO_2	Titanium Dioxide
28. SPR	Surface Plasmon Resonance
29. GQD	Graphene Quantum Dot
30. Voc	Open circuit voltage
31. J_{sc}	Short circuit current

List of Publications

1. **Rajita Ramanarayanan**, Bhabhina Ninnora Meethal, Nijisha Pullanjiyot, Niveditha Chokiveetil, Sindhu Swaminathan, Metal photocatalysis by red and black nanogold colloids: A rational design through green pathway, *Material Research Express* (2019).
2. **Rajita Ramanarayanan**, Niveditha Chokiveetil, Nijisha Pullanjiyot, Bhabhina Ninnora Meethal, Sindhu Swaminathan, The deterministic role of resonance energy transfer in the performance of bio-inspired colloidal silver nanoparticles incorporated dye sensitized solar cells, *Mater. Res. Bull.*, 2019
3. **Rajita Ramanarayanan**, Bhabhina N M, Dharsana M V, **Niveditha C V**, Sindhu S, Green synthesis of zinc oxide nanoparticles using extract of Averrhoa bilimbi(L) and their photoelectrode applications, *Mater. Today Proceedings*, 5 (2018) 16472–16477.
4. **Rajita Ramanarayanan**, Nijisha P, Niveditha C V, Sindhu S, Natural dyes from red amaranth leaves as light-harvesting pigments for dye-sensitized solar cells, *Mater. Res. Bull.*, 2017, **90**, 156-161.
5. C. V. Niveditha, M. J. Jabeen Fatima, **Rajita Ramanarayanan,** Sindhu Swaminathan , Size Control through Scan Rate Modulation: MappingWater Splitting Efficiency of Micro to Nano Size Cuboidal Copper Oxide Particles, *Journal of The Electrochemical Society*, 165 (14) H908-H915 (2018).
6. Niveditha C V, Nizamudeen A C, **Rajita Ramanarayanan**, Jabeen Fatima M J and Sindhu S, Showcasing the electrode-electrolyte interfacial potential on hydrogen generation by metal oxide electrodes, *Material Research Express*, 5 (2018)1-8.
7. Bhabhina Ninnora Meethal, **Rajita Ramanarayanan**, Sindhu Swaminathan, Surface modification of oxygen-deficient ZnO nanotubes by interstitially incorporated carbon: a superior catalytic platform for sustainable water and surface treatments, *Applied Nanoscience*, 2018, 1-11.

8. Niveditha C V, Aswini R, Jabeen Fatima M J, **Rajita Ramanarayan**, Nijisha P and Sindhu S, Feather like highly active Co_3O_4 electrode for supercapacitor application: A potentiodynamic approach, *Material Research Express*,5 (2018)
9. Niveditha C V, Jabeen Fatima. M J, **Rajita Ramanarayanan**, Bhabhina Ninnora Meethal Sindhu S, Effect of number of cycles in potentiodynamic deposition of *p*-type copper oxide and its supercapacitor applications, *Mater. Today Proceedings*, 5 (2018) 16433–16442.
10. Bhabhina Ninnora Meethal, Nijisha Pullanjiyot, Niveditha C V, **Rajita Ramanarayanan**, Sindhu S, Inorganic-organic semiconductor hybrid nanocomposite for anticorrosion applications, *Mater. Today Proceedings*, 5 (2018) 16394–16401.

Book Chapters

11. 1. Rajita Ramanarayanan, Sindhu S, Emphasising the role of Silver nanoparticles in the enhancement of photocatalytic efficiency of TiO_2 , **RECENT ADVANCES IN THEORETICAL AND EXPERIMENTAL PHYSICS**,**ISBN 978-93-5321-814-0,40-48.**

Conference Presentations

1. *Natural dye extracted from red spinach (Amaranthus mangostanus) as photo-sensitizer for Dye Sensitized Solar Cell* at **International Conference on Computing, Communication, Nanophotonics, Nanoscience, Nanomaterials and Nanotechnology (12C4N-2K16) held on 7th-8th April, 2016 at Holy Grace Academy, Thrissur (Oral Presentation).**

2. *Green synthesis of zinc oxide nanoparticles using extract of Averrhoa bilimbi(L) and their photo electrode applications* at **International Conference on Advanced Materials (SCICON-16) held on 19-21 December, 2016 at Amrita Vishwa Vidyapeetham, Coimbatore (Poster Presentation).**

3. *A Green approach towards the synthesis of zinc oxide nanoparticles* at **Two day National Seminar on Green approach to chemistry research Alchemy 2018 held on Feb 27-28 at MAMO College, Manassery, Calicut (Oral Presentation).**
4. Rajita Ramanarayanan, Sindhu S, *Black Black gold nanoparticles for improved photocatalytic degradation of Methylene Blue dye at* **International Conference on Chemistry and Physics of Materials ICCPM 2018 on 19-21 December 2018 at St Thomas College,Thrissur (Oral Presentation).**
5. Rajita Ramanarayanan, Sindhu S ,*Emphasising the role of Silver nanoparticles in the enhancement of photocatalytic efficiency of* TiO_2, **MESMAC International conference 2019 held at MES College, Mambad on 15-17 January 2019 (Oral Presentation).**

CHAPTER 1

INTRODUCTION

INTRODUCTION

The need for energy has been a driving force for human civilisation since time immemorial starting from the discovery of fire. With the passage of time fossil fuels occupied the centre stage leading to tremendous achievements in improving the standard of living of the common man. The scarcity of fossil fuels and the increasing pollution rates due to green house emissions have forced the scientific world to look for alternate sources of energy .Due to the ever growing demands and exploding population energy shortage has been a serious topic of discussion among academicians and social scientists in the last few decades worldwide. India with its fast growing economy and population faces a tough challenge and a great opportunity to successfully explore various non-conventional sources of energy like solar,wind, biomass, geothermal, tidal etc.

Among the nonconventional energy resources only solar and wind energy have lead to wide commercial applications. Inspite of these advances wind energy suffers from serious limitations of high installation cost and proper geographical location to facilitate efficient energy conversion. Hence the responsibility for providing clean and green energy everywhere solely rests on solar energy due to its abundant availability. The rate of energy received by the earth from solar energy is approximately $3x\ 10^{24}$ joules which is sufficient to fulfil the growing energy demands[1]in India, by virtue of its favourable location near tropic of canceris blessed with ample amount of sunlight throughout the year. India receives solar energy about 5000 trillion kWh per

year with 2300–3200 hours of sun shine in most parts of India which on proper utilisation is sufficient enough to solve the present energy crisis[2].

The effective utilisation of natural resources particularly sunlight for energy harvesting applications is an active area of research for the past few decades. The two prominent methods of light harvesting are photovoltaics and photocatalysis. Though both depend on the electron –hole generation, the electron –hole pairs are driven in a circuit to get current in photovoltaics whereas they participate in a redox reaction in photocatalysis. The discovery of photocatalysis is credited to Fujishima and Honda for their path breaking discovery of photocatalytic splitting of water on TiO_2 electrode under ultraviolet light[3]. Photocatalysis is defined as a process where light and the catalyst interact with each other to drive a chemical reaction. The photocatalysis involves the generation of excited electrons in a catalyst (metal, semiconductor and metal-semiconductor) with simultaneous generation of holes upon illumination by light. The photoexcited electrons and holes induces formation of highly reactive hydroxyl ions whose interaction with organic compounds in water/air form biodegradable products[4]. Photocatalysis is responsible for a variety of applications like water/air purification, hydrogen evolution, anti-bacterial and anti-fogging studies[5]

The concept of photovoltaic cells was first proposed by French Physicist E. Becquerel which is defined as a physical/chemical phenomenon which generates electric current/voltage on exposure to sunlight. There are two major technologies associated with harnessing sunlight for human needs; one is the photovoltaic solar technology using semiconductor solar cells which convert sunlight to electricity. Second type is the solar thermal technology which traps

sunlight and uses it for various applications. The thermal technology operating at low temperature (below 100˚C) directly uses solar radiation whereas the high temperature technology involves concentration of the heat of sunlight to elevated temperatures and conversion of heat to other forms of energy (mechanical) for electricity generation[6].

The solar power can be used for small units like individual homes to big industries, from urban belts to remote areas making it flexible to be used for all kinds of needs of the society.

1.1 **Generations of Photovoltaic cells**

The first generation solar cells include the following type of cells made of crystalline silicon (Si) wafers of about 200-400 μm [7].

a) Single Crystal Cells where a single crystal is used

b) Multi Crystal Cells/ poly crystalline where crystal grains are present

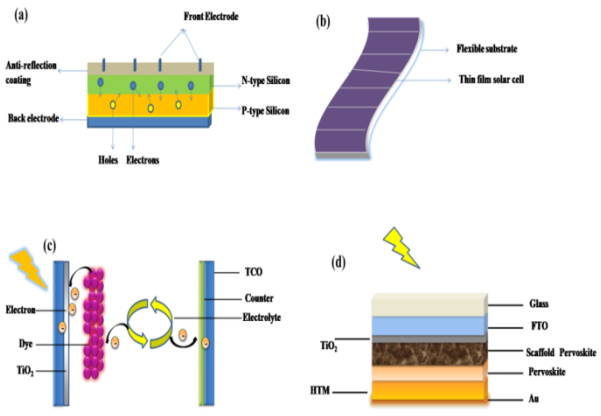

Fig.1.1 Generations of Solar cells (a) Silicon (b) Thin film (c) DSSC (d) Perovskite

The basic Si solar (Fig.1.1a) cell is a p-n junction made up of p-type and n-type semiconductor separated by a depletion layer used for charge generation; collection and transport. When light fall on the p-n junction, electrons are excited from valence band to the conduction band and holes created in the valence band. These electron- hole pairs generated diffuse towards the region of lower concentration leading to charge and subsequently current flow. Metallic contacts are present at the front and rear ends for the proper channelling of electrons and holes. Silicon is a non-toxic, abundant, most researched material for photovoltaic applications with a bandgap of about 1.12 eV with absorption of about 1160 nm[8]. The maximum theoretical efficiency for solar cells having a band gap of 1.1 eV has been calculated to 30 % by Shockley-Quiessner limit[9].The silicon solar cells exhibit high efficiencies among solar cells with about 26% efficiencies commercially available in market[10].

The fabrication of Silicon for solar cells is a highly specialised process involving time and money prompting the scientific community to think of alternate solar cell technologies. Among the two types of silicon solar cells, monocrystalline show high efficiency, but polycrystalline are said to commercially successful due to their ease of preparation. The fundamental loss mechanisms in these cells are the inability to absorb photons with energy less than the bandgap, thermalization of photon energies exceeding the bandgap and contact losses[11].

The amorphous silicon (α-Si) has gained prominence inspite of its low efficiencies (4-5%) because the silicon crystals are grown randomly without much stringent procedures which makes its processing cheaper compared to

crystalline silicon cells. Though unstability is an issue with amorphous solar cells, they have advantages like resistance to temperature and climate variations [12].

The second generation solar cells comprise of thin film solar cells made up of Cadmium/sulphide/ Telluride (CdTe/ CdS), Copper Indium Gallium Selenide (CIGS), and amorphous Silicon (α-Si).Here the light absorbing layer is thinner and flexible (Fig.1.1b) compared to the first generation silicon solar cells. These solar cells though present less efficiencies compared to first generation cells, have an advantage of commercial viability as they can prepared through large scale production. Moreover these cells can be assembled on various glass/polymer and flexible substrates[13].

Among thin film solar cells CdTe is one of the most promising candidates because of its direct bandgap (1.5 eV), good light absorption, chemical stability and a promising efficiency of around 15 % [14]. The CdTe solar cell suffers from drawbacks of toxicity of cadmium and the relative scarcity of the materials in nature.

CIGS solar cell consisting of copper indium gallium selenide is a quaternary direct bandgap semiconductor which offers a higher efficiency of 10-12% compared to other thin film solar cells. They exhibit longer cell life without much degradation thus making it a potential candidate for long term cost efficient solar cells[15].

In general, the advantages of second generation solar cells are they have high absorption coefficient, simple synthesis protocol (do not need vacuum always), cost effectiveness and can be assembled on a variety of substrates. The

disadvantages are toxicity issues and scarcity of the materials used in solar cell in future.

The third generation solar cells aim to combine the efficiency of first generation solar cells with the cost effective production techniques of second generation[16].

The third generation solar cells comprise of the following types

a) Nanocrystal/ Quantum Dot (QD) based solar cells
b) Polymer based solar cells
c) Dye-Sensitized Solar Cells (DSSC)
d) Concentrated Solar Cells

Nanocrystal based cells are also known as Quantum dot cells are semiconductor materials from transiton metal groups in the size of few nanometers. When a photon strikes the semiconductor (QD), electron-hole pairs are generated. The semiconductor quantum dot as sensitizers have advantages of band gap tunability, high absorption coefficient, inorganic nature and multiple exciton generation possibility making it a promising material in solar cell technology[17]. The QD based solar cells are due to their excellent photophysical properties are predicted to show good efficiencies due to their unique property of multiple exciton generation involving formation of more than one electron –hole pair upon absorption of a single photon. The size/morphology, QD synthesis methods, device architecture etc play a vital role in the efficiency of QD sensitized solar cells[18].

Polymer solar cells (PSC) are a class of solar cells which are likely to show great promise in future low cost photovoltaic technologies. These type of solar cells are light weight, flexible and can be fabricated on plastic substrates. These devices use conjugated polymers which have good absorption in visible region, can be tuned optically through molecular design and possess very good charge carrier mobilities [19].

Dye sensitized solar cells (DSSC) are light weight, less toxic, efficient solar cells first proposed by O' Regan, M. Grätzel in 1991 with an efficiency exceeding 7%. Higher efficiencies of 12.3% were reported for a liquid electrolyte DSSC with a zinc porphyrin dye and cobalt based electrolyte in 2011[20]. Typically a DSSC (Fig.1.1c) comprises of a photoanode containing a broad bandgap oxide semiconductor (TiO_2 / ZnO / SnO_2) deposited on a transparent conducting substrate (FTO/ITO), a sensitizing dye/ QD, an electrolyte (I^- / I^-_3) and a counter electrode (generally Pt/ Carbon materials) . Each part of the DSSC has a major role in the efficiency and cost of DSSC. Hence ample research has been conducted in the development of structurally different photoanodes, dyes with high absorption coefficient, highly efficient redox electrolytes and various combinations of counter electrodes for an optimum cell performance[21]. Though efficiency above 10 % has been reported by various groups, DSSC has its shortcomings due to shorter shelf life and degradation issues.

Perovskite based solar cell are made of pervoskite structure material (ABX_3) where X generally is a halide which is used as a light harvesting layer. Perovskites are the recent front runners of solar cell technology, which have promising efficiencies comparable to silicon solar cells. Perovskite structures

(Fig.1.1d) come in various architectures depending on the nature of the perovskite layer that is as light absorbing layer or e^-/ h^+ transport layer [22]. Though perovskite were used as sensitizers similar to a DSSC model, newer solar cells are following different architecture similar to thin film assembly for better results.

Concentrated solar cells / Concentrated Photovoltaics (CPV) use lenses / mirrors to concentrate the light energy obtained from sunlight. These solar cells use light energy from a large space and concentrate it over a small area of the PV cell [23].This method is very effective in utilising the available solar energy in the most effective way. The advantage of CPV is use of lesser materials, lower cost, high efficiency and applicable to all types of cell configurations [24]. However these cells work under direct beam of sunlight and not applicable for diffuse light conditions.

Tandem cells are another class of solar cells consisting of p-n junctions in different semiconductor materials of increasing bandgap are placed on top of each other in increasing order with highest bandgap material interacting with the light first[25]. By the careful choice of bandgap, thickness, doping characteristics optimum efficiency is obtained by the effective splitting of solar light by the different cells.

The fourth generation (4 G) PV technology uses the low cost/ flexibility of polymer thin film solar cells with the stability of inorganic nanostructures. These inorganic nanostructures impart charge transport/charge dissociation, improved energy harvesting cross-section to the device. The 4 G Photovoltaics envisages improved charge transport and optical coupling in PSCs with the

incorporation of inorganic systems like carbon based materials(carbon nanotubes, graphene) metal nanoparticles, metal oxide and nanohybrids (carbon-metal oxide) [26].The use of inorganic nanostructures in organic cells with proper optimisation is anticipated to revolutionise the affordable solar technology market.

1.1 Operational principle of DSSC

The DSSC is not based on p-n junction principle of the traditional solar cells where the basic semiconductor material performs the charge generation /transfer for energy conversion. In a DSSC photogeneration and electron transport occurs in different materials exploring a new way to improve light harvesting.

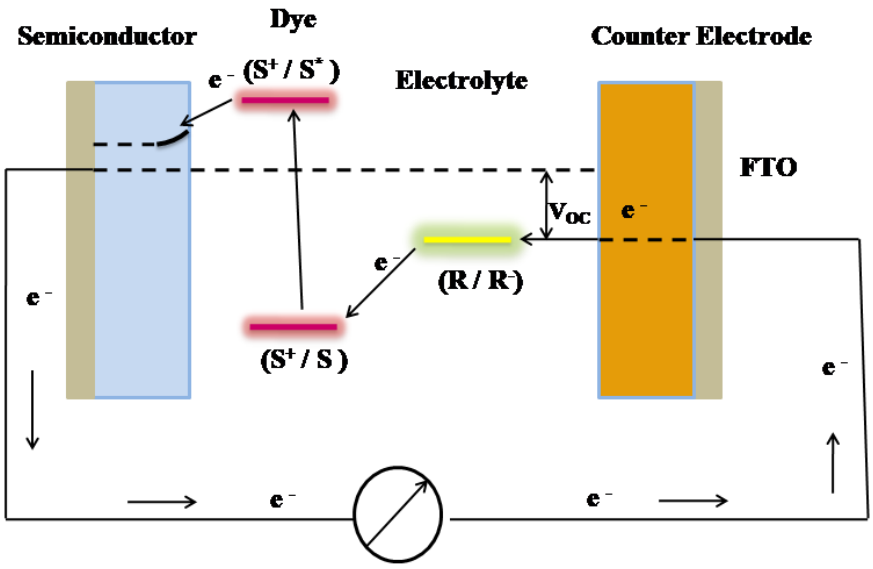

Fig.1.2 Working principle of DSSC

The illumination by light causes the photoexcitation of the dye generating excited electrons which are transferred to the conduction band of the semiconductor which get transported to the transparent conducting oxide

(TCO) and flows through the circuit as shown in Fig. 1.2. The dye is regenerated by the electrolyte (redox couple) whose electron is restored at the counter electrode thus completing the circuit as shown in Fig. 1.2. The cycle operation of DSSC can be summarized by equations below [27].

Working Electrode: $S + h\upsilon = S^*$

$$S^* = S^+ + e^-$$

$$2\,S^+ + 3\,I^- = 2\,S + I^-_3$$

Counter Electrode: $I^-_3 + 2\,e^- = 3\,I^-$

The architecture of a typical DSSC consists of a TCO substrate, dye adsorbed semiconductor thin film (anode) and electrolyte sandwitched between the anode and the counter electrode.

TCO are substrates with high transparency to visible light, low resistance and ability to protect the cell from dust and moisture. This layer plays a crucial role in the movement of electrons generated in the cell to the external circuit. The commonly used TCO are Fluorine doped Tin oxide (FTO), Indium doped Tin oxide (ITO) and Al-Zinc oxide (AZO). In spite of its advantages ITO is costly ,uses scarce and toxic elements making FTO a feasible choice for light applications[9].

Photoanodes are composed of nanostructured thin films of wide gap semiconductors like TiO_2, ZnO, Nb_2O_5, SnO_2 etc. They adsorb the sensitized dye and facilitate movement of electrons to the external circuit. Hence the performance of any DSSC is largely influenced by the properties of the photoanode material. Large surface area, transparency to visible light, optimum

carrier density and good electron transport are the defining qualities of an ideal photoanode material [28]. Varied morphology of the anode material like spheres, rods, tubes etc obtained through different synthetic protocol have been experimented in DSSC to get improved efficiencies. TiO_2 is the most commonly used photoanode due to its higher conduction band edge, dye loading ability and electron affinity.

Though recombination losses are a major cause of concern in DSSC, use of blocking layer and $TiCl_4$ treatments can minimise the effect to a great extent[29]. The incorporation of noble metals (Ag/ Au) in photoanodes like TiO_2, ZnO helps to obtain competitive efficiencies by reducing recombination losses and increasing absorption of light by virtue of its surface plasmon resonance. The role of noble metals like gold, silver in enhancing the various parameters of a DSSC has been extensively reported[30].

The sensitizing dye in a DSSC is attached to the wide band gap semiconductor surface generally by dip coating method. Light absorption is determined by molar extinction coefficient of the dye and surface area adsorption of the semiconductor oxide by the dye [31]. The commonly used sensitizing dyes are ruthenium based complexes such as N3, N719, etc which have a broad absorption spectra ($\Delta \lambda$= 350 nm), but low molar extinction coefficients (10,000- 20,000 M^{-1} cm^{-1}) and limited NIR light harvesting. However, organic dyes come with a high molar extinction coefficient and lower absorption spectra compared to ruthenium based dyes. An ideal sensitizer of a solar cell under 1 Sun illumination should be able to absorb all photons below the threshold wavelength of 920 nm[32]. Further it should have various attachment groups to anchor itself to the semiconductor surface and

inject electrons upon excitation with a quantum yield nearly unity. The excited state should be well matched with the conduction band of the semiconductor to ensure efficient transfer of electrons. The dye should have a positive redox potential to be regenerated by the electrolyte after electron transfer and stable enough to endure many cycles in the cell due to continuous exposure to natural light.

Another class of sensitizers used in solar cells are QDs which have an advantage of high optical absorption coefficients, large dipole moment and multiple exciton characteristics[33]. The commonly used QDs broadly come under three groups cadmium-chalcogenide QDs (CdS,CdSe,CdTe) (b) lead-chalcogenide QDs (PbS, PbSe)(c) antimony sulfide Sb_2S_3QDs.Though efficiencies above 5% have been reported by some groups, the efficiencies in general are still low due to losses at the TiO_2 /QD and TiO_2 / electrolyte interface and lesser anchoring of QD on to the semiconductor surface compared to the dyes.

Redox electrolyte provides electrons to the oxidised dye and regenerates the dye, thus acting as a crucial medium in the functioning of the DSSC. The mobility and electron kinetics of the redox couple determines the efficiency of a solar cell to a great extent .Based on the physical state, the electrolytes are classified into liquid, quasi-solid/gel and solid state electrolyte.

Among the liquid electrolyte iodide/triodide (I^-/ I_3^-) is the most popular due to its fast oxidation of I^- at the photoanode/electrolyte interface aiding dye regeneration and slow reduction at the electrolyte/ counter interface. Additionally it is cheap, easy to prepare and possess high stability[34]. However it is corrosive against noble metals (Ag/Au/Pt) leading to instability

of the cell. The upper limit of V_{oc} of 0.9 V seriously hampers the further development of liquid based cells paving way to cobalt based electrolytes which present a better V_{oc}.

The quasi-solid electrolytes are prepared by locking the liquid electrolytes in a polymer matrix helps overcoming the volatilization and leakage effects of liquid electrolytes[35] . In spite of the above advantages, the gel electrolytes suffer from lower efficiencies and thermodynamic instability at higher temperatures.

Solid state electrolytes including various hole transporting materials (HTM) are being extensively investigated as future electrolytes for DSSC[36]. Many p-type materials like CuI, CuSCN, $CsSnI_3$ and organic polymers are being successfully used as solid state electrolyte in solar cells. Inspite of their high mobility solid state electrolytes suffer from comparatively lower efficiencies in general to liquid based cells due to the poor penetration of the electrolyte into the photoanode. By attaining higher diffusion into the photoanode along with high conductivity, HTM seem to be promising materials for new generation electrolytes.

The counter electrode (CE) in a DSSC does the important work of accepting electrolyte from the external circuit and completing the redox reaction. The noble metals are the obvious choices for CE materials for their good electrocatalytic behaviour and high conductivity[37].Pt is being extensively used in liquid electrolyte DSSC and Au, Ag in solid state electrolytes solar cell. The high cost and corrosive behaviour of noble metals have lead to the exploration and successful application of carbon based

materials and inorganic compounds for low cost production of CE materials for DSSC. Similarly conductive polymer materials are being explored to be used in flexible DSSC and nanocomposites of carbon/organic/inorganic materials are being explored to match upto to the advantages of existing Pt counter in DSSC.

1.2 Various strategies for light harvesting in solar cells

An efficient solar energy conversion involves the optimised performance of the major four factors of light absorption,charge separation, migration and recombination parameters. Among the various semiconductor materials available, titanium dioxide (TiO_2) has been extensively used in all forms of light energy harvesting namely solar cells, photocatalysis, and hydrogen evolution. Inspite of its advantages like cost effectiveness, wide band gap, easy availability, relative stability etc, TiO_2 needs to be modified due to its low absorption in the visible region.

To eventually improve solar energy harnessing, a single material is insufficient, paving way for the development of hybrid structures of different materials combined in an effective way to incorporate the advantages of the both. These modifications include doping by elements like nitrogen, tin, niobium etc, surface modification using metal nanoparticles and co-sensitization using different sensitizers.

Though doping has been successfully done in various studies[38], the presence of mid-gap levels tend to compromise on charge mobility and lead to high charge recombination[39]. The metal nanostructures have been successfully used to improve carrier generation, optical absorption and suppressing loss mechanisms in solar devices. The metal nanostructures possess a unique property of LSPR (Localised surface plasmon resonance)

which is majorly responsible for the heightened optical and electronic responses in light based devices.

Surface plasmons are collective oscillations of free electrons which are generated when nanoparticles are irradiated by electromagnetic radiations. The generation of surface plasmons in a small space is LSPR. When the frequency of this oscillaton is the same as the frequency of the light that incident on it, the plasmon is said to be on resonance with the incident light[40] and is responsible for the strong optical absorption. Both absorption and scattering of light by the metal nanoparticles with spectral properties are influenced by the shape, size, dielectric properties and the local environment of the nanostructures. Noble metals like gold, silver in their nanoregime exhibit strong absorption in the visible region which has been exploited to manipulate light to suit various photonic applications.

The metal nanostructures affect the efficiency of the solar cells through two major mechanisms[41].

(a) Radiative effects which include far field scattering and near field enhancement mechanisms.

(b) Non-radiative effects like hot electron transfer and plasmon resonant energy transfer.

The light incident on a nanomaterial is scattered into far field to improve the light trapping by the device[42]. The photons undergo multiple scattering and are reabsorbed by the sensitizer. This technique is useful to trap the photons which directly have not been absorbed by the sensitizer by tuning LSPR wavelengths according to sensitizer's absorption. Light scattering properties are largely dependent on the size of the nanoparticle as predicted by

Mie's theory. The scattering cross-section (σ) of a metal nanoparticle of size (a) is given by

$$\sigma = \frac{8\pi}{3} k^4 a^6 \left| \frac{\epsilon_{metal} - \epsilon_{medium}}{\epsilon_{metal} - 2\epsilon_{medium}} \right|^2$$

where ϵ is the dielectric permittivity of metal and medium and k = $\frac{2\pi}{\lambda}$

From the above equation it is evident that the cross-section increases with increase in size and a > 30 nm sizes seem to be ideal cases for far field scattering effects in solar cells as per previous reports.

The scattering effects are also affected by shape effects due to the ability to polarise light by non-spherical nanostructures with sharp edges like cubes, pyramids etc. Similarly the composition of the nanomaterials and permittivity of the surrounding medium also affect the far field scattering effects in a solar cell. Among the commonly used metal nanoparticles like gold (Au) and silver (Ag), silver shows higher carrier generation in solar devices due to its lower optical losses across all wavelengths of the solar spectrum. Similarly TiO_2 coated nanoparticles show enhanced scattering effects due to the higher dielectric constant of TiO_2.

The plasmonic metal nanostructures act as amplifiers by enhancing the electromagnetic field to many fold in their immediate vicinity. The increase in intensity increases the number of photons available to be absorbed by the solar cell. The enhanced electromagnetic field increases the electron-hole pair generation in the sensitizer facilitating a better transfer of electrons to the conduction band of TiO_2. Electromagnetic near fieldsgenerated by LSPR are greatly influenced by size, morphology and composition[43]. The non-

spherical nanostructures owing to high concentration of charges at the corners and at the corners significantly enhance local EM field due to a phenomenon called lightning rod effect. The Ag nanoparticles show stronger near field effects when compared to Au due to the wavelength dependent behaviour of the real and imaginary dielectric functions of the respective metals.

Hot electron transfer (HET) is the excitation of the metal surface electrons by EM radiation generating highly energetic electrons (hot electrons) which overcome the schottky barrier and enter the conduction band of the semiconductor. However HET can occur only when the Fermi levels of the metal and semiconductor are equilibrated[44]. In a plasmon induced hot electron transfer (PHET), plasmon decays into a hot electron-hole pair via Landau damping on the time scales of Femto seconds. The hot electrons generated are then transferred to the adjacent semiconductor to enhance charge generation. The efficient production of hot electrons is governed by the morphology, size and composition of metal nanostructures. It has been reported that the size limit of hot electron generation in Ag/Au is below 20 nm which matches with the path length of the electron.

Plasmon Resonant Energy Transfer (PRET) is an important non-radiative phenomenon which is involved in plasmonic enhancement in a solar cell. PRET occurs when resonant energy is transferred from the metal to the semiconductor in the vicinity via dipole-dipole coupling. PRET occurs when there is a spectral overlap between the LSPR spectrum and semiconductor absorption. The transferred plasmon energy creates electron-hole pairs in the acceptor which may be a semiconductor or any other photoactive material in a solar cell[45]. PRET is also known as resonance energy transfer (RET) or

Plasmon induced resonance energy transfer (PIRET) and does not require band alignment like HET.

PRET competes with FRET in which excited carriers are transferred from the semiconductor to the plasmonic nanostructure. The PRET efficiency is more significant when the dephasing time of the plasmonic component is more than that of the acceptor (semiconductor) component. However FRET occurs in the reverse case when dephasing time of the plasmonic nanostructure is less than that of the semiconductor. Further as PRET dominates FRET subsides and vice versa conserving the total energy.

1.4 Basic FRET mechanism

The distribution of molecules in dark condition is given by Boltzmann distribution equation $\frac{Nj}{No} = \frac{Pj}{Po} e_{KT}^{-\Delta E}$ where ΔE is the energy difference between the excited and ground level and k is the Boltzmann constant. Here Nj, No are the energy levels and Pj, Po are their populations respectively.

The energy difference between the vibrational levels is around 3 kcal/ mol which makes it possible for molecules to go to excited state from ground state at room temperature conditions. The excitation of ground level molecules takes place fast (of the order of 10^{-15} sec). But the thermal losses of the order 10^{-12}sec occur between the vibrational levels and hence emission takes place from the lowest excited state. This reason amounts to the difference in between the excitation and emission wavelength, known as stokes shift.

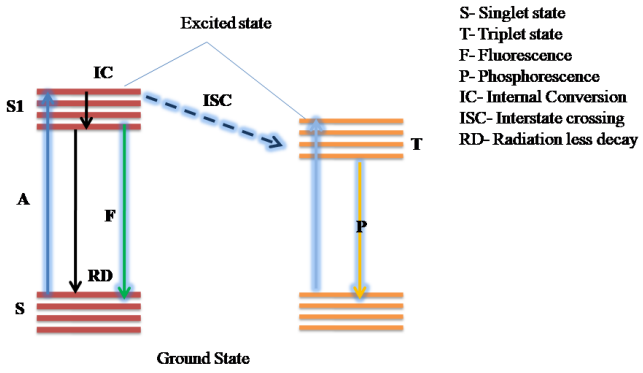

Fig.1.3 Jablonski diagram showing various transitions

A molecule which reaches an excited state can reach ground state in multiple pathways as shown in Jablonski diagram (Fig.1.3). The molecule in ground state on absorption of photon of a given energy gets excited to a higher state S1. The excited state consists of multiple vibrational energy levels represented by horizontal lines. The excited molecule decays to the lower vibrational level via internal conversion process. Internal conversion is a radiationless process where molecular spin is preserved but energy is converted to heat. The molecule can radiatively come to ground state by emission of light (fluorescence) occurring in the timescale of 1- 10 ns[46]. The system undergoes interstate crossing to triplet state by spin inversion and then undergoes a radiation to ground state via phosphorescence. Though both fluorescence and phosphorescence are forms of luminescence, they differ from their respective energies and timescales. Further fluorescence occurs in singlet excited state whereas phosphorescence occurs from triplet state.

However if there is another molecule in the close vicinity of the excited molecule there is a possibility of the excited molecule known as donor

transferring its energy via non-radiative way to the molecule known as acceptor. This process is known as resonance energy transfer (RET). As this transfer is detected in fluorescence quenching experiments it is called Fluorescence Resonance energy transfer (FRET). However the Fluorescence term is misleading as the phenomenon is not radiative and hence has been replaced by Förster in honour of T. Förster who explained the phenomena through quantum mechanics[47]. For a FRET to occur one of the important criteria is the quantum yield of the Donor and Acceptor.

Quantum yield (QY) is generally defined as the ratio of photons emitted as fluorescence to the photons absorbed in the incident radiation[48]. All the radiative and non-radiative processes that are responsible for depopulation of an excited state contribute to QY. A number of physical and chemical processes cause decrease in emission/fluroscence intensity known as quenching. Quenching can be of two types namely dynamic and static respectively. Dynamic/collisional quenching occurs when an excited flurophore is in contact with another molecule to facilitate an energy transfer[49]. Static quenching occurs when a flurophore forms a stable complex with the other molecule. Quenching in emission spectra is the first indication of a FRET mechanism. The energy transfer from an excited flurophore (Donor) to a nearby molecule is summarized through the equation below[50].

$D^* + A = D + A^*$ Where D, A are donor and acceptor respectively

The energy transfer occurs without a photon emission and does not require the acceptor to be fluorescent. The energy transfer becomes apparent by the quenching of fluorescence and decrease in the lifetime of the donor. For a

FRET mechanism to occur the following conditions are mandatory. They are (i) there should be an overlap of the emission spectrum of the donor and absorption spectrum of the acceptor. (ii) Donor-acceptor separation around 1-10 nm. (iii) orientations of the dipole moments of the donor-acceptor pair[51].

The efficiency of the FRET process (E_T) depends on the inverse sixth power of the distance between the donor and acceptor pair (R) and is given by

$$E_T = \frac{{R_0}^6}{{R_0}^6 + R^6}$$

Where R_0 the Förster radius, is the distance at which the efficiency of energy transfer is 50%. The Förster radius (R_0 in Angstrom) is given by

$$R_0 = 0.211[k^2 n^{-4} Q_D \, J(\lambda)]^{1/6}$$

Where Q_D is the fluorescence quantum yield of the donor in the absence of acceptor, n is the refractive index of the solution, k^2 is the dipole angular orientation of the molecules and J is the spectral overlap integral of the donor – acceptor pair[52]. Here $k^2$is given by the equation

$$k^2 = (2\cos\theta_D \cos\theta_A - \sin\theta_D \sin\theta_A \cos\varphi)^2$$

where$\theta_D$and $\theta_A$are the angles of the dipoles of D and A with the axis joining them and$\varphi$is the angle between the corresponding planes of donor emission and acceptor absorption dipoles with different orientations. Though the value of k^2 varies from 0 to 4 according to the relative orientation of the dipoles but the differentially averaged value of 2/3 is taken for calculation purposes as orientation is difficult to determine in most of the cases.

The spectral overlap integral is given by

$$J = \int_0^\infty I_D(\lambda) \in_A (\lambda)\lambda^4 d\lambda$$

Where ϵ is the molar absorption coefficient in M^{-1} cm^{-1}, λ is the wavelength of the light in nm and I_D is the intensity of the fluorescence spectrum of the donor normalized on the wavelength scale.

The theoretical possibility of the phenomenon was proposed by J Perrin and F. Perrin who reported that energy transfer via dipole-dipole interactions, can take place between two neighbouring molecules[53].T. Förster developed the idea further based on Fermi-golden rule approach where the transfer of excitation energy from donor to acceptor is promoted via coulomb interaction[54].

According to the Fermi golden rule the transfer rate of energy in a donor-acceptor system is given by

$$\kappa_{transfer} \; \alpha \left| \langle \varphi_{D_a} \varphi_{A_b} | V | \varphi_{D_b} \varphi_{A_a} \rangle \right|^2$$

Where $\kappa_{transfer}$ the non-radiative transfer rate and V is is the interaction term proportional to third power of the intermolecular distance. As the rate of energy transfer is proportional to the square of this coupling, it leads to the inverse sixth power dependence of the radiative rate given by

$$\kappa_{transfer} = \frac{1}{\tau_D}\left(\frac{R_0}{R}\right)^2$$

Where τ_D is the lifetime of the donor in the absence of the acceptor. The rate of transfer equation leads to the FRET efficiency expression (E_T) is expressed as

$$E_T = 1 - \frac{\tau_{DA}}{\tau_D} = 1 - \frac{I_{DA}}{I_D}$$

Where τ_{DA} is the lifetime of the donor in the presence of the acceptor. Here I_{DA} and I_D are the intensities of fluorescence spectrum of the donor in the presence and absence of the acceptor.

FRET between two different molecules have been discussed so far, but if the excitation spectrum of a flurophore overlaps with its emission spectrum, then FRET can occur between identical molecules known as HOMO FRET[55]. There difference occurs in the polarization of the two molecules inspite of similar spectral conditions.

1.5 FRET applications

FRET has immense applications in biology for detecting conformational changes and folding of proteins and other cell parameters. It is being used as a power technique for imaging in clinical diagnostics and providing important information in cell biology research. Biosensors based on this mechanism are specially designed to detect and identify the relevant biological molecules, quantifying the amount of certain elements present in the system[56]. They are also used as pH probes for various cell studies because of their sensitivity in molecular range. Apart from a wide range of biological applications, FRET mechanism has been reported to show chemical sensing and light harvesting properties. The energy transfer property has been harnessed in solar cells to improve efficiency in different combinations of QD/ Dye- QD/Dye/ metal nanoparticles (MNP) hybrid assemblies[57]. In this work we focus on the role of energy transfer as described by FRET theory in photoconversion mechanism. FRET plays a vital role in exciton transport, light harvesting and charge transport in solar cells. The spectral absorption range is extended using photoactive materials like QDs and Dyes which transfer absorbed energy to the

sensitizer of the DSSC. However FRET also competes with the charge transfer mechanism, thus turning into a potential loss mechanism in the case of metal nanoparticles [58]. The deterministic role of FRET in photoelectron efficiency coupled with proper optimisation helps in achieving improved energy harvesting systems.

1.6 Aim and Objective of the Thesis

This work focuses on the judicious selection and development of hybrid FRET systems for light energy harvesting to be utilized in solar cell structure. Different combinations based on semiconductor, dye, metal nanoparticles and quantum dots are to be used for the fabrication of hybrid FRET systems for light harvesting applications.

- To synthesize Ag/Au MNPs, dyes via different green protocols, to be used as acceptors for the Donor-Acceptor FRET system in solar cells.
- To optimize various parameters like shape, size and concentration of the metal nanoparticles, dipping time of the metal oxide electrode in metal colloids, are to be done to obtain better efficiencies in DSSC.
- To confirm FRET and the effect of FRET in the overall efficiency of the four different combinations namely Semiconductor (TiO_2)-Ag, Dye-Au, GQD-CdSe QD, Dye-Dye hybrid systems.

1.8 Outline of the thesis

- First chapter discusses the different types of light harvesting technologies, various solar cell design and architecture of DSSC. Further

various plasmonic enhancement mechanisms due to metal nanoparticles are discussed and finally the theory of FRET mechanism is elucidated in detail.

- Second chapter discusses the various characterisation techniques employed to study the materials and mechanisms involved in this work.
- Third chapter deals with the novel synthesis protocols used for synthesis of nanomaterials / dyes used in this work. Silver nanoparticles , gold nanoparticles and natural dyes were synthsized using a green protocol and their characterisations conducted in detail.
- Fourth chapter discusses the role of FRET in the Ag-TiO_2 hybrid systems to be used as photoanode in DSSC. It is seen that FRET plays a complementary role to plasmonic enhancement in a Ag-TiO_2 photoanode DSSC. The charge and energy transfer mechanisms of TiO_2-Ag-Dye interfaces have been elucidated in detail.
- Fifth chapter discusses the size/shape dependence of Au nanoparticles in the photocatalysis of dye in a Dye-Au hybrid system. Here the FRET between dye and Au plays a supplementary role to plasmonic enhancements in the direct photocatalysis of the dye.
- Sixth chapter discusses the energy transfer between a GQD-CdSe hybrid system where GQD acts as a donor and CdSe acts as an acceptor in different device architectures.
- Seventh chapter explores a novel Dye-Dye hybrid system with Rhodamine B as donor and Chlorophyll obtained from natural dye as acceptor.
- Last chapter summarises the work done in this investigation and discusses future plans with the materials synthesized for different energy harvesting applications.

References

[1] M. Grätzel, Photoelectrochemical cells, Nature. 414 (2001) 737–740.

[2] S.K. Gupta, R.S. Anand, Development of Solar Electricity Supply System in India : An Overview, J. Sol. Energy. 2013 (2013).

[3] A. Fujishima, K. Honda, Electrochemical photolysis of water at a semiconductor electrode, Nature. 238 (1972) 37–38.

[4] R. Saravanan, F. Gracia, A. Stephen, Basic Principles, Mechanism, and Challenges of Photocatalysis, in: Nanocomposites Visible Light. Photocatal., Springer, 2017: pp. 19–41.

[5] Bhabhina. N. M, Rajita. R, Sindhu. S, Surface modification of oxygen-deficient ZnO nanotubes by interstitially incorporated carbon : a superior photocatalytic platform for sustainable water and surface treatments, Appl. Nanosci. (2018) 1–11.

[6] N.K. Sharma, P.K. Tiwari, Y.R. Sood, Solar energy in India : Strategies , policies , perspectives and future potential, Renew. Sustain. Energy Rev. 16 (2012) 933–941.

[7] M.T. Kibria, A. Ahammed, S.M. Sony, F. Hossain, A Review : Comparative studies on different generation solar cells technology, (2014) 51–53.

[8] E. Płaczek-Popko, Top PV market solar cells 2016, Opto-Electronics Rev. 25 (2017) 55–64.

[9] A. Gopi, S. Lingamoorthy, S. Soman, K. Yoosaf, R. Haridas, S. Das, Modulating FRET in Organic-Inorganic Nanohybrids for Light Harvesting Applications, J. Phys. Chem. C. 120 (2016) 26569–26578.

[10] A.W.Y.H.-B. Martin A. Green, Keith Emery, Yoshihiro Hishikawa, Wilhelm Warta, Ewan D. Dunlop, Dean H. Levi, Solar cell efficiency tables (version 49), Prog. PHOTOVOLTAICS Res. Appl. (2016) 1–11.

[11] C. Battaglia, A. Cuevas, S. De Wolf, High-efficiency crystalline silicon solar cells: status and perspectives, Energy Environ. Sci. 9 (2016) 1552–1576.

[12] S. Sharma, K.K. Jain, A. Sharma, Solar Cells : In Research and Applications — A Review, Mater. Sci. Appl. (2015) 1145–1155.

[13] A.G. Aberle, Thin-film solar cells, Thin Solid Films. 517 (2009) 4706–4710.

[14] N. Romeo, A. Bosio, V. Canevari, A. Podestà, Recent progress on CdTe/CdS thin film solar cells, Sol. Energy. 77 (2004) 795–801.

[15] F. Kessler, D. Rudmann, Technological aspects of flexible CIGS solar cells and modules, Sol. Energy. 77 (2004) 685–695.

[16] G. Conibeer, Third-generation photovoltaics, Mater. Today. 10 (2007) 42–50.

[17] O.E. Semonin, J.M. Luther, M.C. Beard, Quantum dots for next-generation photovoltaics, Mater. Today. 15 (2012) 508–515.

[18] A.J. Nozik, M.C. Beard, J.M. Luther, M. Law, R.J. Ellingson, J.C. Johnson, Semiconductor quantum dots and quantum dot arrays and applications of multiple exciton generation to third-generation photovoltaic solar cells, Chem. Rev. 110 (2010) 6873–6890.

[19] A.C. Mayer, S.R. Scully, B.E. Hardin, M.W. Rowell, M.D. Mcgehee, Polymer-based solar cells A significant fraction of the cost of solar panels comes from the, Mater. Today. 10 (2007) 28–33.

[20] M.G. Brian O' Regan, A low -cost ,high-efficiency solar cell based on dye-sensitized colloidal TiO2 films, Nature. 353 (1991) 737–740.

[21] M. Ye, X. Wen, M. Wang, J. Iocozzia, N. Zhang, C. Lin, Z. Lin, Recent advances in dye-sensitized solar cells: From photoanodes, sensitizers and electrolytes to counter electrodes, Mater. Today. 18 (2015) 155–162.

[22] M.K. Assadi, S. Bakhoda, R. Saidur, H. Hanaei, Recent progress in perovskite solar cells, Renew. Sustain. Energy Rev. 81 (2018) 2812–2822.

[23] W. Guter, J. Schöne, S.P. Philipps, M. Steiner, G. Siefer, A. Wekkeli, E. Welser, E. Oliva, A.W. Bett, F. Dimroth, Current-matched triple-junction solar cell reaching 41.1% conversion efficiency under concentrated sunlight, Appl. Phys. Lett. 94 (2009) 2007–2010.

[24] M. Khamooshi, H. Salati, F. Egelioglu, A. Hooshyar Faghiri, J. Tarabishi, S. Babadi, A review of solar photovoltaic concentrators, Int. J. Photoenergy. 2014 (2014) 1–17.

[25] A.C. Tamboli, D.C. Bobela, A. Kanevce, T. Remo, K. Alberi, M. Woodhouse, Low-Cost CdTe / Silicon Tandem Solar Cells, IEEE J. Photovoltaics. 7 (2017) 1767–1772.

[26] K.D.G.I. Jayawardena, L.J. Rozanski, C.A. Mills, M.J. Beliatis, N.A. Nismy, S.R.P. Silva, 'Inorganics-in-Organics': recent developments and outlook for 4G polymer solar cells, Nanoscale. 5 (2013) 8411–8427.

[27] J. Wu, Z. Lan, J. Lin, M. Huang, Y. Huang, L. Fan, G. Luo, Electrolytes in dye-sensitized solar cells, Chem. Rev. 115 (2015) 2136–2173.

[28] C.C. Raj, R. Prasanth, A critical review of recent developments in nanomaterials for photoelectrodes in dye sensitized solar cells, J. Power

Sources. 317 (2016) 120–132.

[29] A. Sedghi, H.N. Miankushki, Influence of TiCl4 treatment on structure and performance of dye-sensitized solar cells, Jpn. J. Appl. Phys. 52 (2013) 1–7.

[30] Y.H. Jang, Y.J. Jang, S. Kim, L.N. Quan, K. Chung, D.H. Kim, Plasmonic Solar Cells: From Rational Design to Mechanism Overview, Chem. Rev. 116 (2016) 14982–15034.

[31] M.K. Nazeeruddin, E. Baranoff, M. Grätzel, Dye-sensitized solar cells: A brief overview, Sol. Energy. 85 (2011) 1172–1178.

[32] M. Grätzel, Conversion of sunlight to electric power by nanocrystalline dye-sensitized solar cells, J. Photochem. Photobiol. A Chem. 164 (2004) 3–14.

[33] W. Wang, G. Jiang, J. Yu, W. Wang, Z. Pan, N. Nakazawa, Q. Shen, X. Zhong, High Efficiency Quantum Dot Sensitized Solar Cells Based on Direct Adsorption of Quantum Dots on Photoanodes, ACS Appl. Mater. Interfaces. 9 (2017) 22549–22559.

[34] G. Boschloo, A. Hagfeldt, C.O.N. Spectus, Characteristics of the Iodide / Triiodide Redox Mediator in Dye-Sensitized Solar Cells, Acc. Chem. Res. 42 (2009) 1819–1826.

[35] P. Wang, S.M. Zakeeruddin, P. Comte, I. Exnar, M. Grätzel, Gelation of ionic liquid-based electrolytes with silica nanoparticles for quasi-solid-state dye-sensitized solar cells, J. Am. Chem. Soc. 125 (2003) 1166–1167.

[36] Y. Duan, Q. Tang, Y. Chen, Z. Zhao, Y. Lv, M. Hou, P. Yang, B. He, L. Yu, Solid-state dye-sensitized solar cells from poly(ethylene

oxide)/polyaniline electrolytes with catalytic and hole-transporting characteristics, J. Mater. Chem. A. 3 (2015) 5368–5374.

[37] J. Wu, Z. Lan, J. Lin, M. Huang, Y. Huang, L. Fan, G. Luo, Y. Lin, Y. Xie, Y. Wei, Counter electrodes in dye-sensitized solar cells, Chem. Soc. Rev. 46 (2017) 5975–6023.

[38] A.K. Chandiran, F. Sauvage, M. Casas-Cabanas, P. Comte, S.M. Zakeeruddin, M. Graetzel, Doping a TiO 2 Photoanode with Nb 5+ to Enhance Transparency and Charge Collection Efficiency in Dye-Sensitized Solar Cells, J. Phys. Chem. C. 114 (2010) 15849–15856.

[39] M. Vafaei, M.R. Mohammadi, Impact of chromium doping on physical, optical, electronic and photovoltaic properties of nanoparticle TiO photoanodes in dye-sensitized solar cells, New J. Chem. (2017) 1–36.

[40] W.L. Barnes, A. Dereux, T.W. Ebbesen, subwavelength optics, Nature. 424 (2003) 824–831.

[41] W.R. Erwin, H.F. Zarick, E.M. Talbert, R. Bardhan, Environmental Science Light trapping in mesoporous solar cells with plasmonic nanostructures, Energy Environ. Sci. 9 (2016) 1577–1601.

[42] K. Tanabe, Field Enhancement around Metal Nanoparticles and Nanoshells : A Systematic Investigation, J. Photochem. Photobiol. A Chem. 112 (2008) 15721–15728.

[43] D.B. Ingram, S. Linic, Photoelectrodes : Evidence for Selective Plasmon-Induced Formation, J. Am. Chem. Soc. (2011) 5202–5205.

[44] Y.K. Lee, H. Lee, C. Lee, E. Hwang, Hot-electron-based solar energy conversion with metal – semiconductor nanodiodes, J. Phys. Condens. Matter. 28 (2016) 1–13.

[45] J. Chen, S. Shen, P. Guo, M. Wang, J. Su, D. Zhao, L. Guo, Plasmonic Ag@SiO2 core/shell structure modified g-C3N4 with enhanced visible light photocatalytic activity, J. Mater. Res. 29 (2014) 64–70.

[46] M.P.U. Maria-Chantal Chirio-Lebrun, Fluorescence resonance energy transfer (FRET): theory and experiments, Biochem. Educ. 26 (1998) 320–323.

[47] R.M. Clegg, THE HISTORY OF FRET : From conception through the labors of birth, (1996) 1–45.

[48] A.E. Markus Grabolle, Monika Spieles, Vladimir Lesnyak, Nikolai Gaponik, U. Resch-Genger, Determination of the Fluorescence Quantum Yield of Quantum Dots : Suitable Procedures and Achievable Uncertainties, Anal. Chem. 81 (2009) 6285–6294.

[49] S.A. Selvaraj Naveenraj, Ramalinga Viswanathan Mangalaraja, Jerry J. Wu, Abdullah M. Asiri, Gold Triangular Nanoprisms and Nanodecahedra : Synthesis and Interaction Studies with Luminol toward Biosensor Applications, Langmuir. 2 (2016) 11854–11860.

[50] H.E.A. Kramer, P. Fischer, The Scientific Work of Theodor Fçrster : A Brief Sketch of his Life and Personality, ChemPhysChem. 12 (2011) 555–558.

[51] D.L. Andrews, D.S. Bradshaw, Resonance Energy Transfer, (2009) 1–25.

[52] S. Sadhu, K.K. Haldar, A. Patra, Size Dependent Resonance Energy Transfer between Semiconductor Quantum Dots and Dye Using FRET and Kinetic Model, J. Phys. Chem. C. 114 (2010) 3891–3897.

[53] B.R. Masters, Paths to F¨ orster's resonance energy transfer (FRET)

theory, Eur. Phys. J. H. 139 (2014) 87–139.

[54] S. Saini, H. Singh, B. Bagchi, Fluorescence resonance energy transfer (FRET) in chemistry and biology : Non-Förster distance dependence of the FRET rate, Indian Acad. Sci. 118 (2006) 23–35.

[55] D.M. Jameson, Förster Resonance Energy Transfer, in: Introd. to Fluoresc., 2014: pp. 145–160.

[56] S.A. Hussain, An Introduction to Fluorescence Resonance Energy Transfer (FRET), (2009) 1–4.

[57] L. Etgar, J. Park, C. Barolo, V. Lesnyak, S.K. Panda, P. Quagliotto, S.G. Hickey, M.K. Nazeeruddin, A. Eychmüller, G. Viscardi, M. Grätzel, Enhancing the efficiency of a dye sensitized solar cell due to the energy transfer between CdSe quantum dots and a designed squaraine dye, RSC Adv. 2 (2012) 1–5.

[58] K. Feron, W.J. Belcher, C.J. Fell, P.C. Dastoor, Organic solar cells : Understanding the role of f̈orster resonance energy transfer , Int. J. Mol. Sci. 13 (2012) 17019–17047.

CHAPTER 2

CHARACTERISATION TECHNIQUES

CHARACTERISATION TECHNIQUES

2.1 Introduction

The advances in fundamental sciences, design of new materials and techniques in the improvement of devices depends on the accuracy and reliability of the measuring instruments to a great extent. The measuring instruments use a variety of probes from light of different wavelengths (x-rays to infrared) to electrons and protons to investigate a nanomaterial [1]. This chapter briefly describes characterisation techniques which are backbone of any doctoral work in experimental studies in nanoscience. The instrumentation used in studying the various physical properties of nanomaterials and solar cell characterization are described in this chapter. The methodology used in basic characterisation of nanomaterials to characterisation techniques to quantify various parameters in solar cells has been listed below.

- UV-Vis Spectroscopy
- Fluorescence Spectroscopy (PL)
- Fourier Transform Infrared Technique (FTIR)
- Dynamic Light Scattering (DLS)
- X-ray Photon Spectroscopy (XPS)
- X-ray diffraction (XRD)
- Scanning Electron Microscopy (SEM)
- Transmission Electron Microscopy (TEM)
- Solar Cell Characterisations
- Lifetime measurements

2.2 Characterisation Methods

2.2.1 Ultraviolet-Visible (UV-Vis) Spectroscopy

Optical microscopy in various forms is used to study the nature of nanomaterials in the preliminary level. Optical microscopy employs two different ways to obtain the desired information about the specimen that is from transmitted light through the sample and reflected light from the sample[2].

The UV-Vis spectrometer instrument measures absorption/transmittance/ reflectance in UV, visible and IR range. The commonly used spectrometers uses dual beam design where the sample and the reference are measured over the same spectral range.

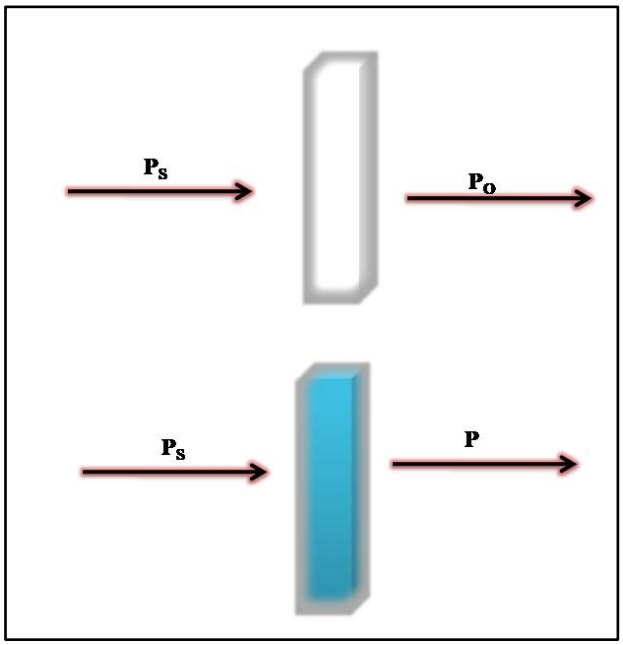

Fig.2.1 Sample and reference in a UV –Setup

Let the intensity from the source is P_S and the intensity after passing from a solvent be P_O and the intensity from the sample with absorbance A is P as

shown in Fig.2.1. The relationship between the absorbance and transmittance is given by

$$A = -logT = -log\frac{P}{P_0}$$

The absorption of light by a sample is directly proportional to the distance the light travels through the sample and the concentration of the absorber. The linear relation between the absorbance of the sample and concentration of the sample is given by Beer-Lambert law

$$A = \epsilon lc$$

Where A is the absorbance of the sample, ϵ is the molar absorptivity, l is the length of the sample, c is the concentration of the sample.

DRS is a good sampling tool to extract information about various size and electronic structure of powdered and crystalline materials. Due to the variety of sample shapes/sizes the light falling on a sample is reflected, transmitted and scattered in different directions as shown in Fig.2.2. The reflected beam can be specular that is mirror like or scattered within the sample known as diffuse reflectance[3].

The diffuse reflection is used as an experimental tool to characterize various materials and their properties. The dilution of the sample with a non-absorbing material like $BaSO_4$ improves the spectra by better penetration of light into the sample and suppression of specular reflections which affect the accuracy of the spectrum. The samples having smaller size also exhibit good diffuse reflectance spectra making it very suitable for nanoparticle range.

Diffuse reflectance finds wide applications in paper, dye, ceramics and textile industries [4]. It is a vital tool for measuring optical properties of materials which have good scattering properties and not suitable for absorption spectroscopy.

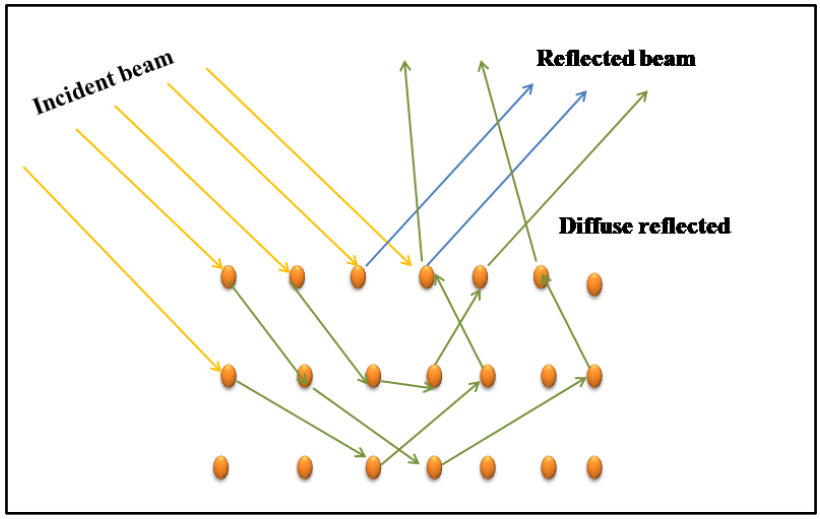

Fig.2.2 Principle of Diffuse reflectance spectroscopy

2.2.2 Photoluminescence (PL) Spectroscopy

PL spectroscopy is a non-destructive experimental method to determine the electronic structure of a wide range of materials. When photons of higher energy interact with a semiconducting material, the electrons are excited to the conduction band paving way for the formation of holes in the valence band [5].

The electron hole recombination causes emission of photons characteristic of the nature of the material. PL spectrum gathers information about the electronic structure, defect states of the sample under consideration. PL

spectroscopy is used to measure micrometer depth variations in crystal quality and purity of the sample.

2.2.3 FTIR measurements

FTIR spectroscopy works on the principle of vibrational excitation of molecular bonds by absorption of infrared light energy. The interaction of infrared radiation with matter is used to identify and understand the chemical composition of samples, which may be solid, liquid, thin films etc. When IR radiation passes through the sample some of it is absorbed and transmitted and the spectrum is expressed as transmittance versus frequency[6]. The instrument recording the IR spectrum is the Fourier transform infrared spectrometer which converts the signals to a measurable output. The FTIR uses different techniques transmission (T), Attenuated Total Reflection (ATR), specular reflection and diffuse reflectance techniques to gather information about a sample.

The FTIR spectrum of guava leaf is shown in the Fig.2.3 showing peaks of various compounds present in the leaf. The frequency in horizontal axis is given by reciprocal centimetres (cm^{-1}) for convenience where each wavenumber corresponds to a bonding characteristic of the chemical constituents of the leaf.

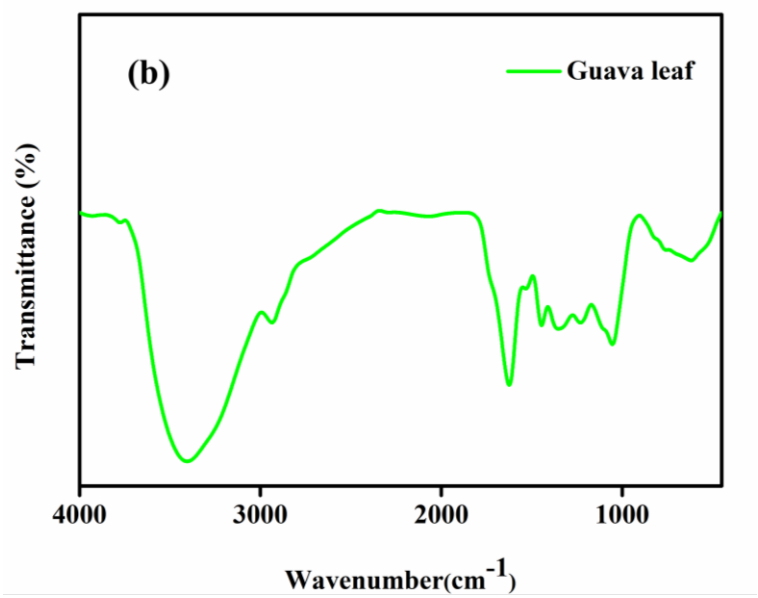

Fig.2.3 FTIR spectrum of guava leaf

FTIR is being widely used as a diagnostic tool in life sciences [7], chemical identification in food industry, research, forensics and gas leaks in petroleum industry.

2.2.4 Dynamic Light Scattering (DLS) measurements

DLS or Photon Correlation Spectroscopy (PCS) or Quasi-elastic Light Scattering (QELS) uses scattered light to measure the rate of diffusion of the particle. This technique measures the average size of particles in a system utilising the principle of Brownian motion of the particles suspended in a liquid[8]. DLS measurements are taken by recording the fluctuations in the intensity of the particles in the sample under study. The size of a nanoparticle measured through DLS measurement is expressed as hydrodynamic radius which again depends on the velocity of the Brownian motion.

$$d(H) = \frac{\mathrm{kT}}{3\pi\eta\mathrm{D}}$$

Where d (H) = hydrodynamic diameter, k is the Boltzmann coefficient,ŋ is the viscosity, T is the absolute temperature and D is the translational diffusion coefficient.

A typical DLS instrument consists of monochromatic laser beam targeted into a solution with nanoparticles in Brownian motion causes a Doppler Shift when the light hits the moving particle. This change in intensity/frequency upon hitting the particles is used to compute the size distribution and hydrodynamic radius of the nanoparticle using the autocorrelation function.

However due to the aggregation of particles and other effects in the solution the hydrodynamic radius varies in value of the actual value of size of the nanoparticles. The DLS has been successfully employed to find contaminants and other elements present in the drinking water across various countries[9].

2.2.5 XPS measurements

XPS was developed by Nobel Laureate K. Siegbahn in 1960s to identify and quantify the elements present on the surface of the sample. It is a highly sensitive instrument which can trace the chemical elements and the nature of bonding between them upto few nm from the surface. XPS works on the principle of photo-excitation and subsequent ejection of electrons from their bound state by X-rays of sufficient energy[10].

The principle of XPS based on the photoelectric theory proposed by Einstein for a single atom hit by a photon of energy hυ is presented below

$$h\vartheta + E_i = E_f + K.E$$

$$h\vartheta - K.E = E_f - E_i = B.E$$

Here E_i and E_f are the initial and final energies of the system respectively. K.E is the kinetic energy of the photoelectron and B.E is the binding energy.

The XPS spectra determined from experiment is a plot of no of counts versus the binding energy. The XPS spectrum consists of energy peaks corresponding to various elements and the area of these individual peaks gives information about the amount of the element present in sample. By virtue of its high resolution XPS is conducted in a high vacuum environment so that the ejected photoelectrons are readily collected by the electron analyser.

2.2.6 XRD measurements

XRD is an efficient analytical technique to determine the crystalline nature and hence the cell parameters/ structure of materials. It is based on the constructive interference of diffracted beams coming from a crystal lattice due to the interaction of the x-rays with the material[11].

Let us consider a set of planes separated by distance d as shown in the Fig.2.4. The path difference for diffracted rays from adjacent planes is 2d Sinθ. The constructive interference of radiation from successive plane occurs when the path difference is an integral multiple of wavelength as expressed by Bragg's law

$$2dSin\theta = n\lambda$$

Bragg's condition is valid when the wavelength of light is comparable to lattice spacing d. Hence electromagnetic radiations of short wavelength like x-rays are used for the analysis instead of visible light as the lattice spacing size is very small.

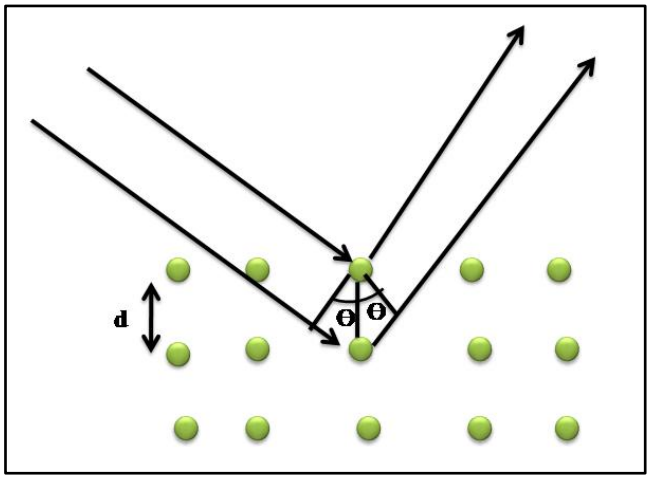

Fig.2.4 Bragg's principle of X-ray Diffraction

The Fig. 2.5 shows a typical X-ray diffraction pattern of ZnO with the characteristic peaks indexed using standard reference JCPDS data. From the graph lattice size, d spacing, *h k l* planes and information about crystallite structure can be obtained by comparing with the reference JCPDS data. The presence of other elements/ impurities in the sample can be observed due to additional peaks apart from regular peaks of the sample.

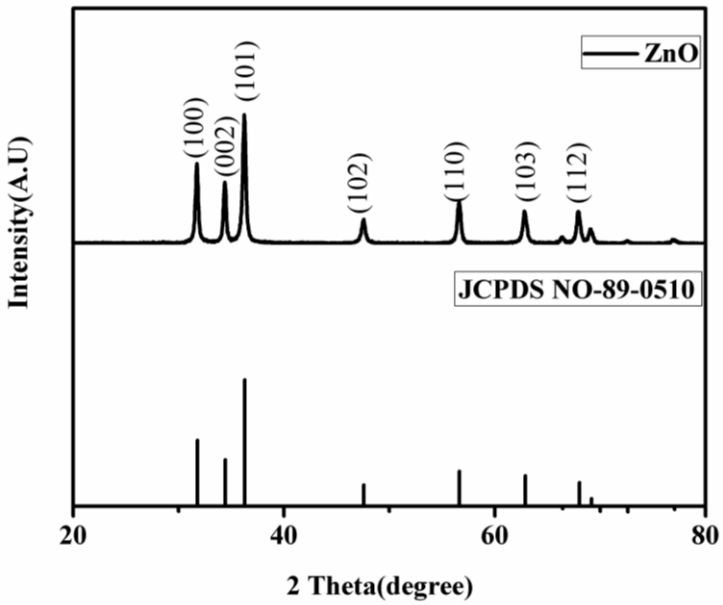

Fig.2.5 XRD data of ZnO along with JCPDS

2.2.7 SEM measurements

The basic principle of SEM involves by targeting electron beam onto a sample surface and obtaining the secondary/backscattered beam to obtain information about the sample. SEM analysis is suitable for magnification around 50 nm and gives vital information about surface morphology. A SEM instrument consists of an electron gun as source of electron, electromagnetic lenses to focus the electrons and a detector to collect the secondary electrons. The samples are analysed after by applying conductive layers of gold on their surface. Further the collected electron signals are converted to images for study by the computer display. The instrument is operated in vacuum to ensure proper collection of the electrons and to avoid damage to the sample [12] .

SEM is an excellent technique to observe the topography, agglomeration, size, surface functionalisations and shape of nanoparticles. A typical SEM image showing flake like morphology and uniform distribution is shown in Fig.2.6. Field Emission-SEM is an advanced instrument which has narrower electron beams of high and low energy to obtain the best spatial resolution and upto 1 million times magnification.

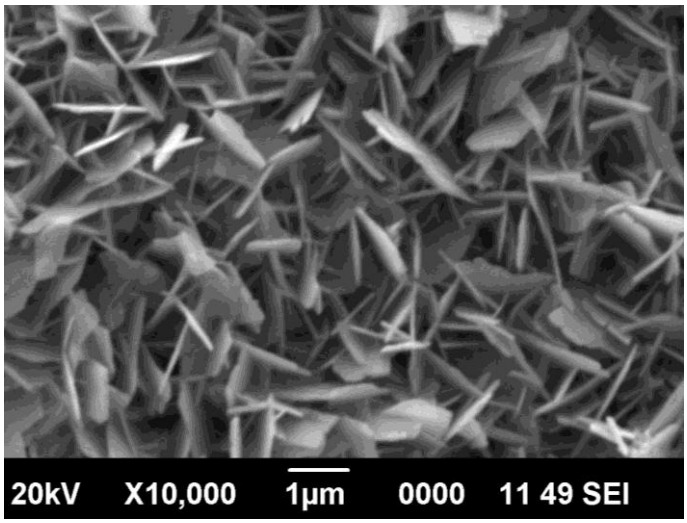

Fig.2.6 SEM image of ZnO nanoparticles

EDAX uses the X-rays to determine the elemental composition of the samples under consideration. This technique detects the x-rays coming from the nanoparticles due to the impinging of the sample by fast electrons. The EDAX spectrum consists of peaks of the individual elements constituting the sample and comes as an attachment to the SEM analysis[13].

EDAX is used for finding doped elements or surface chemical composition of samples, trace elements in contaminant analysis and purity determination of pharmaceutical products. A typical EDAX spectrum of silver incorporated TiO_2 is shown in Fig.2.7.

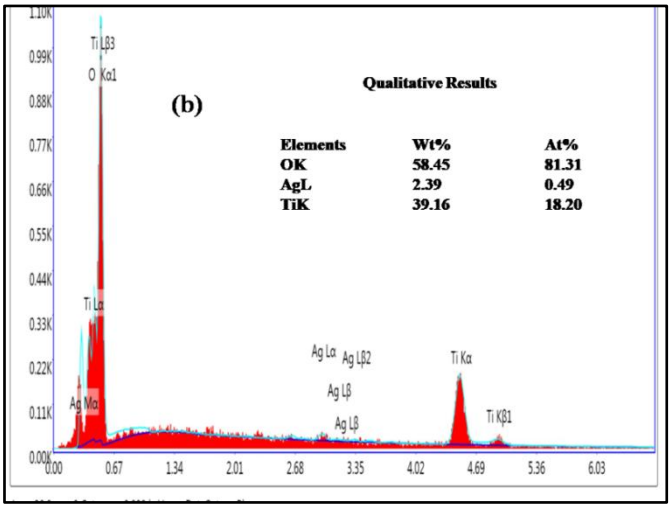

Fig.2.7 EDAX spectrum of Ag-TiO_2

2.2.8 Transmission Electron Microscopy (TEM) measurements

The TEM is a high resolution instrument to obtain images of nanoparticles using electrons instead of light as in conventional microscopy. TEM produces the best resolution for obtaining nanoparticle size, morphology and grain size as the wavelength of electrons is much smaller than that of light making TEM images many orders of magnitude superior than that from a light microscope[14].

A typical TEM instrument consists of an electron gun from which beam of electrons is focused into a small, thin sample by the use of the condenser lens. The collimated beam when strikes the specimen, parts of it are transmitted depending upon the thickness and nature of the specimen. The transmitted portion is focused into an image on phosphor screen or charge coupled device (CCD) camera by the objective lens[15]. Commercially available TEM instruments are capable of provide magnification of 150,000 X with minimum distortion.

Selected Area Diffraction Pattern (SAED) is an experimental technique performed along with TEM to obtain crystallite nature of the specimen. The atoms in the crystalline sample act as diffraction grating to the incoming electron beam forming a diffraction pattern.By observing the SAED pattern of a sample, the crystalline nature of the sample and lattice parameters can be obtained like XRD[16]. But SAED differs from XRD as it is limited to a very small area of the sample. The TEM image of Silver nanoparticles along with SAED pattern concerned with this work is presented in Fig.2.8

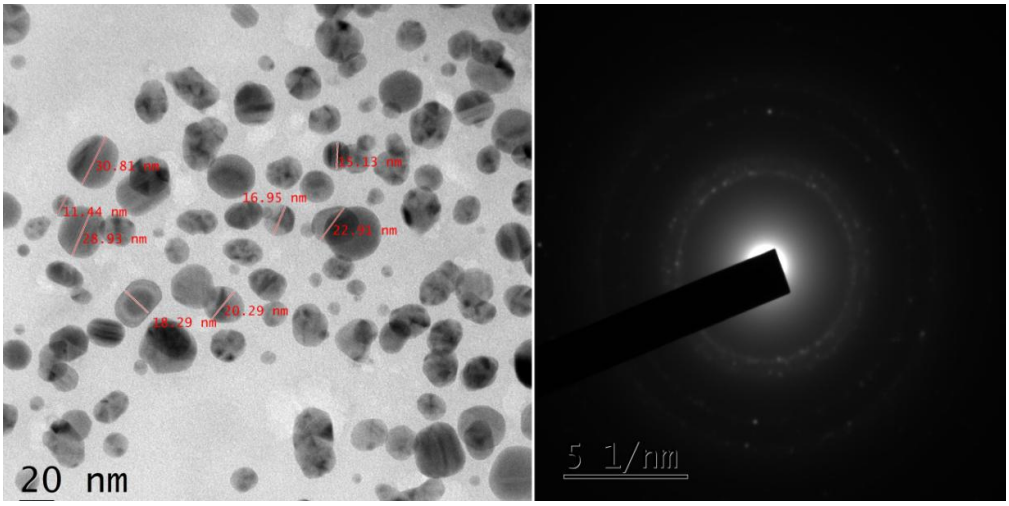

Fig.2.8 TEM image and SAED pattern of silver nanoparticles

2.2.9 Solar Cell Characterisations

The implementation of standard characterization techniques is essential to improve and understand the impacts of each device component for further optimization and stabilization of the DSSC. The efficiency of a solar cell is calculated from the current –voltage (I-V) curves obtained by illuminating the sample by a Solar simulator. The energy conversion is measured per unit area under light illumination.

A solar cell efficiency not only depends on the intrinsic parameters like charge transport/transfer/ recombination but also the external parameters like the device assembly, proper sealing and masking of the photoanode surface[17]. The Current –Voltage (I-V) curve obtained from a cell is shown below in Fig. 2.9

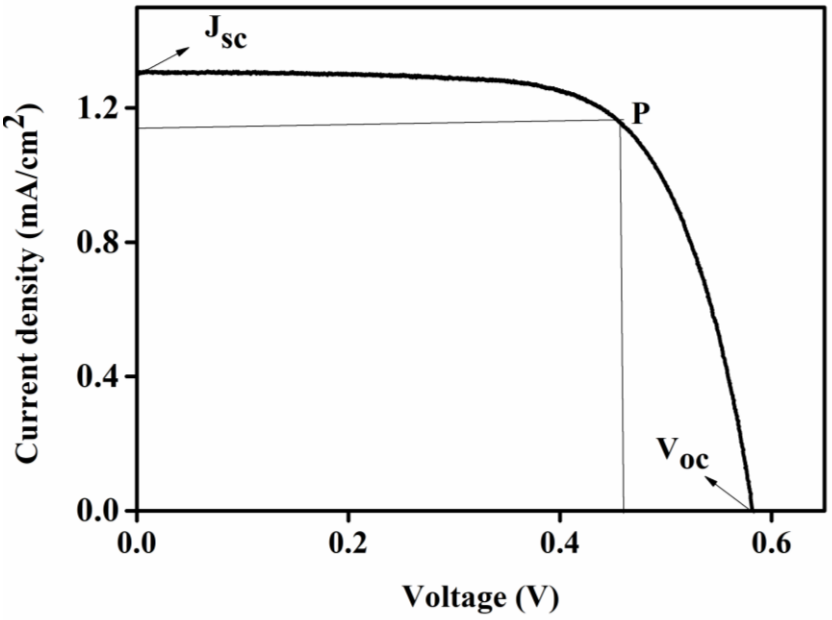

Fig.2.9 J-V Curve of a solar cell

The power conversion efficiency (ŋ) of a DSSC under 1 Sun illumination (AM 1.5) is expressed as

$$\eta = \frac{P_{out}}{P_{in}} = \frac{P_{max}}{100}$$

Where P_{max} is the product of current and voltage at the maximum power point P as indicated in the Fig.2.9. The fill factor (FF) of the solar cell is given by

$$FF = \frac{P_{max}}{V_{oc} \times J_{sc}}$$

Where V_{oc} is the open circuit voltage when the photocurrent is zero and J_{sc} is the short circuit current density at zero voltage[18].

EIS (electrochemical impedance spectroscopy) is a dynamic technique which distinguishes various complex processes occurring at the various interfaces of the DSSC and their impact on the cell efficiency.

EIS involves the investigation of charge transfer dynamics at the various electrode/electrolyte interfaces which is responsible for the photoelectrochemical properties of materials for various applications like solar cells, batteries etc. Electrochemical impedance spectroscopy (EIS) employs steady state method to measure current response an ac voltage as a function of the frequency. The application of very small ac voltages allows to distinctly determine electronic and ionic processes in a DSSC[19].

The EIS studies of a sample are expressed in Nyquist Plot which consists of three semicircles of decreasing frequency corresponding to Pt counter electrode-electrolyte interface resistance (R_1), the electron transfer at the oxide/dye/electrolyte interface (R_2) and Warburg resistance related to diffusion of electrolyte (R_3). Further R_s is the sheet resistance corresponding to FTO film. The first two semicircles occur in the high frequency and middle frequency regions and last semicircle corresponds to low frequency region [20]. The impedance of each interface is plotted after fitting the EIS data with software in terms of an equivalent circuit as shown in Fig. 2.10.

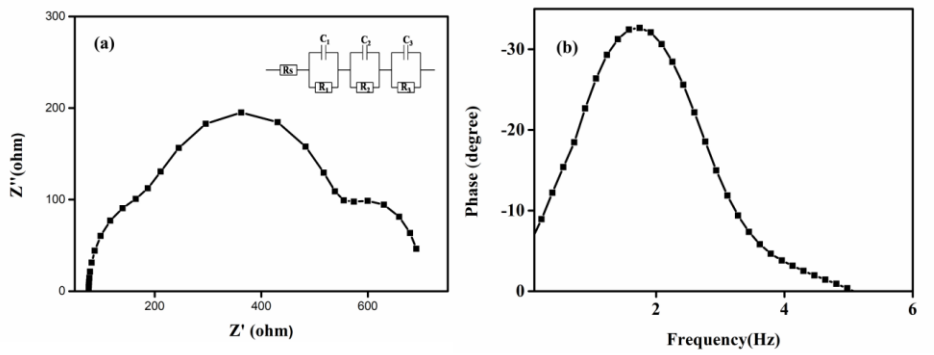

Fig.2.10 (a) Nyquist plot (b) Bode plot of a Solar cell

Bode plot is extracted from EIS parameters and is a plot of frequency response of the solar cell[21]. The charge recombination lifetime (τ_e) obtained from the bode plot is

$$\tau_e = {}^{1}/_{2\pi f_{max}}$$

Where f_{max} is the value of maximum frequency obtained from the bode plot.

2.2.10 Time Correlated Single Photon Counting (TCSPC) measurements

The fluorescence lifetime of a specimen is the time spent by an excited molecule in higher energy state before it reaches to ground state. It is measured as the time taken for the molecules to decay to 1/e of the original population due to various quenching mechanisms.

Lifetime depends on the intrinsic property of the fluorescent molecule and is affected by the presence of impurities which can quench the sample. Fluorescence lifetimes are measured by either time domain or frequency domain method. In time domain method the sample is excited by a short pulse of light whereas it is excited by an intensity modulated light in frequency domain method. Both methods have their advantages and shortcomings, but

time domain method is said to be less expensive and reliable[21].Time Correlated Single Photon Counting (TCSPC), a time domain method is commonly employed to measure decay time measurements using pulsed laser excitation corresponding to the emission peak. As the name suggests TCSPC uses single photon at one time to ensure good resolution and minimum degradation to the sample. The plot is drawn as intensity versus time which normally varies from microseconds to picoseconds[22]. The decay times are fitted exponentially and the average lifetime is calculated as

$$\tau_{avg} = \sum_{i}^{n} \alpha_i \tau_i$$

Though lifetime measurements are used widely in research it serves as a clinching evidence for FRET mechanism involving energy transfer between two molecules, a donor and an acceptor. The energy transfer efficiency (E_T) is expressed as ratio of lifetimes of the samples in the presence and absence of the acceptor

$$E_T = \frac{\tau_{DA}}{\tau_D}$$

Where τ_{DA} and τ_D are the lifetimes of donor in presence and absence of acceptor respectively.

References:

[1] T. Pradeep, Nano: The Essentials, Tata Mc-Graw Hill Education Private Limited, 2007.

[2] K.N. Elton, Characterisation of Materials, John Wiley & Sons, Inc., 2003.

[3] G. Kortum, Reflectance Spectroscopy:Principles,Methods,Applications, Springer-Verlag Berlin Heidelberg, 1969.

[4] R.W. Frei, H. Zeitlin, Diffuse Reflectance Spectroscopy, C R C Crit. Rev. Anal. Chem. 2 (1971) 179–246.

[5] A.R.B. Ruquan Ye, Photoluminiscence spectroscopy and its applications, Phys. Methods Chem. Nano Sci. (2012) 295–305.

[6] A.A. Ismail, F.R. van de Voort, J. Sedman, Fourier transform infrared spectroscopy: Principles and applications, Tech. Instrum. Anal. Chem. 18 (1997) 93–139.

[7] M. Taha, M. Hassan, S. Essa, Y. Tartor, Use of Fourier transform infrared spectroscopy (FTIR) spectroscopy for rapid and accurate identification of Yeasts isolated from human and animals, Int. J. Vet. Sci. Med. 1 (2013) 15–20.

[8] B.J.B. and R. Pecora, Dynamic Light Scattering, Am. Assoc. Phys. Teach. 67 (2000) 16–24.

[9] S.K. Brar, M. Verma, Measurement of nanoparticles by light-scattering techniques, TrAC - Trends Anal. Chem. 30 (2011) 4–17. http://dx.doi.org/10.1016/j.trac.2010.08.008.

[10] P.G. Zambonin, E. Desimoni, X-Ray Photoelectron Spectroscopy: Principles, Instrumentation, Data Processing and Molten Salt

Applications, in: G. Mamantov, R. Marassi (Eds.), Molten Salt Chem. An Introd. Sel. Appl., Springer Netherlands, Dordrecht, 1987: pp. 425–445.

[11] A.L. Ryland, X-ray diffraction, J. Chem. Educ. 35 (1958) 80–83.

[12] A.K. Singh, Experimental Methodologies for the Characterization of Nanoparticles, in: Eng. Nanoparticles, 2016: pp. 125–170.

[13] B. Sarecka-Hujar, R. Balwierz, A. Ostrozka-Cieslik, R. Dyja, D. Lukowiec, A. Jankowski, Scanning electron microscopy and X-ray energy dispersive spectroscopy – useful tools in the analysis of pharmaceutical products, J. Phys. Conf. Ser. 931 (2017) 1–5.

[14] W.D. Pyrz, D.J. Buttrey, Particle size determination using TEM: A discussion of image acquisition and analysis for the novice microscopist, Langmuir. 24 (2008) 11350–11360.

[15] Arthur Beiser, Concepts of Modern Physics, McGraw-HIll, 2003.

[16] W. Zhou, H.F. Greer, What Can Electron Microscopy Tell Us beyond Crystal Structures?, Eur. J. Inorg. Chem. 2016 (2016) 941–950.

[17] J. Salinger, Measurement of Solar Cell Parameters with Dark Forward I-V Characteristics, Acta Polytech. 46 (2006) 25–27.

[18] M. Pazoki, U.B. Cappel, E.M.J. Johansson, A. Hagfeldt, G. Boschloo, Characterization techniques for dye-sensitized solar cells, Energy Environ. Sci. 10 (2017) 672–709.

[19] E. Barsoukov, J.R. Macdonald, Fundamentals of Impedence Spectroscopy, in: Impedance Spectrosc. Theory,Experiment Appl., Third Edit, John Wiley & Sons, Inc., 2018: pp. 1–20.

[20] Q. Wang, J.-E. Moser, M. Grätzel, Electrochemical Impedance

Spectroscopic Analysis of Dye-Sensitized Solar Cells, J. Phys. Chem. B. 109 (2005) 14945–14953.

[21] B. Liu, W. Li, B. Wang, X. Li, Q. Liu, Y. Naruta, W. Zhu, Influence of different anchoring groups in indoline dyes for dye-sensitized solar cells: Electron injection, impedance and charge recombination, J. Power Sources. 234 (2013) 139–146.

[22] S. Kundu, A. Patra, Nanoscale Strategies for Light Harvesting, Chem. Rev. 117 (2017) 712−757.

CHAPTER 3

GREEN SYNTHESIS OF METAL NANOPARTICLES AND EXTRACTION OF NATURAL DYES

GREEN SYNTHESIS OF METAL NANOPARTICLES AND EXTRACTION OF NATURAL DYES

The synthesis and characterisations of gold (Au) and silver (Ag) nanoparticles and natural dye has been reported in this chapter. These metal nanoparticles and natural dye have been synthesized to attain the objectives of the thesis and are novel in terms of design protocol. The methodology adopted to obtain these materials along with the effect of various parameters like volume of the reducing agent, nature of the solvent has been described in detail in this chapter.

3.1 Green Synthesis of Silver Nanoparticles (Ag NP)

3.1.1 Introduction

Silver nanoparticles by virtue of their rare combination of superior optical, catalytic, antimicrobial properties are in great demand for the development of new generation devices. These nanoparticles possess strong absorption in the visible region due to surface plasmon resonance paving way to diverse applications in photonics and energy harvesting applications. These opto-electronic properties are greatly influenced by their synthesis methods, nature of the reducing agent and ambient conditions [1].The conventional synthesis procedures of silver nanoparicles involves chemical methods like sodium citrate, borohydride method, reverse micelles methods and physical methods like laser ablation, radiolytic methods etc [2]. In the past decade environment friendly green synthesis of silver has gained momentum and is being widely

reported for its simple and cost effective protocol. Green synthesis involves the use of biological microorganisms/plant extracts as reducing agent in the preparation of nanoparticles [3, 4]. This work reports the use of leaf extract of guava for the green synthesis of silver nanoparticles. Though guava leaf as reducing agent has been previously reported [5,6],our work assumes importance as it uses a complete green method by using water based extract of guava leaf without using any other chemical reducing agent like sodium hydroxide or ammonia. Moreover the synthesis takes place in few minutes and has been conducted in room temperature.

3.1.2 Experimental

3.1.2.1 Materials

- Silver nitrate (99.9%) (Merck)
- Distilled water (Millipore System)
- Fresh mature leaves of Guava tree

3.1.2.2 Method

The leaf extract was prepared by boiling and stirring 3 grams of fresh cleaned guava (*Psidium guajava)* leaves for 30 minutes in distilled water using a hotplate (IKA RCT Basic). The extract was cooled and filtered using filter paper and stored at 4^{o} C for further uses. The extract can be stored for about 2-3 weeks.

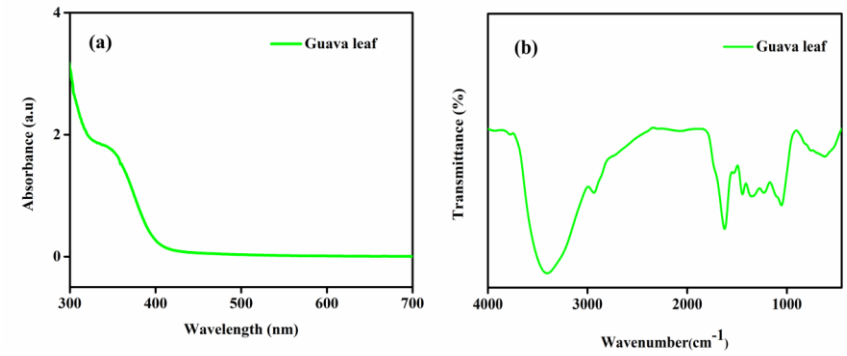

Fig. 3.1 (a) UV-Vis absorption spectrum and (b) FTIR spectrum of guava leaf extract

The UV-Vis spectrum of the guava leaf extract shows a bump at 341 nm and almost zero absorbance throughout the visible region. Hence it can be ideally used as a reducing agent as the peak in the visible region will be solely due to the metal nanoparticle formation. The FTIR spectra of the guava leaf extract show peaks at 3398 (–OH), 2936 (-COOH), 1617 (C=C), 1440 (C–C=C), 1355 (N–O), 1233 and 1051 (C–O), and 631 (R– CH) cm−1 represents the different functional groups present in the leaf extract used for the green synthesis. The presence of these functional groups confirms the existence of flavonoids, tannins, eugenol, quercetin as established by previous reports [7].

For synthesis of silver nanoparticles 1 mL of the extract was added to various volumes (5, 10 and 20) mL of 1 mM of $AgNO_3$ solution and stirred using pipette to ensure uniform mixing. The colour change of the silver salt solution to pale yellow and then yellowish brown implies the formation of silver nanoparticles. The scheme of the synthesis is depicted in Fig. 3.2.The samples are coded as Ag1, Ag2 and Ag3 respectively for particles formed with 5, 10 and 20 mL of the precursor solution.

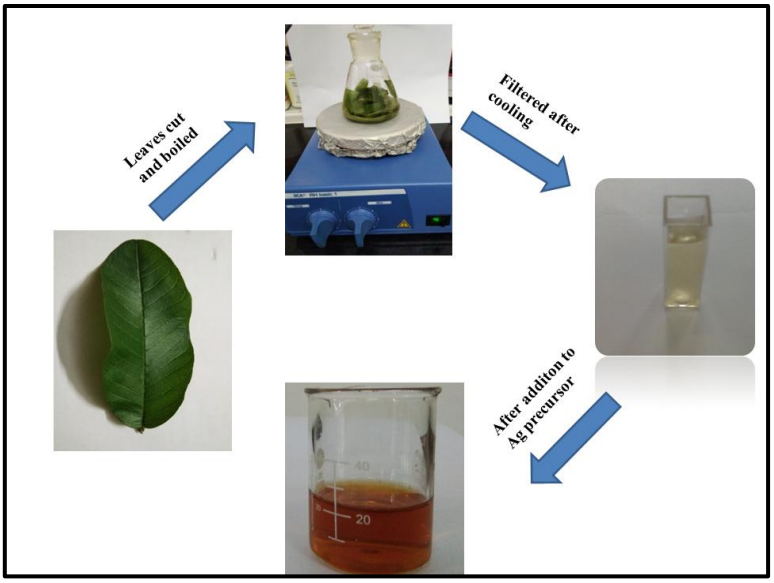

Fig. 3.2 Scheme of synthesis showing formation of Ag nanoparticles

3.1.3 Results and Discussion

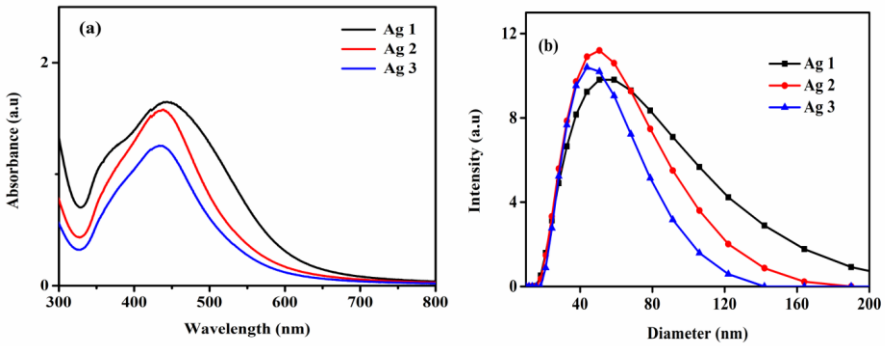

Fig.3.3 (a) UV-Vis spectrum of Ag NPs (b) DLS measurements of Ag NPs

The size and distribution of nanoparticles showed dependence to the amount of guava leaf extract to precursor solution during the synthesis. From the UV-Vis spectral measurements the peak broadening and increase in absorbance intensity with variation of extract quantity is observed from Fig.3.3 (a). The absorbance peak value varies from 435 nm (Ag 3), 438 nm (Ag 2) to 444 nm (Ag 1) nanoparticles. The 1 to 5 ratio (Ag1) showed the highest absorbance intensity corresponding to higher concentration of the extract in the

reaction solution. Further a shift in absorbance peak toward red end of spectrum with increase in concentration of extract is observed. Ag1 showed an extra bump at around 350 nm corresponding to the absorbance peak of guava leaf extract. The bump is seen decreasing with decrease in the concentration of extract in the solution for Ag2 and Ag3. The shifting of surface plasmon peak corresponds to the increase in size as demonstrated by mean free path corrected Mie theory [8].The peak broadening is attributed to increase in polydispersity as reported by Agnihotri e*t al* in the case of co-reduction of silver nanoparticles [9].Thus lower concentration of guava leaf extract yields smaller and more monodisperse silver nanoparticle populations consistent with the previous reports on the dependence of size on the concentration of the reducing /stabilising agent over nanoparticle size and size distributions[10].These findings are supported by DLS measurements which show narrower distribution for Ag3 sample. Hence 1 to 20 volume ratio (Ag3) was chosen for further experiment and analysis.TEM measurements show uniform distribution of nearly spherical nanoparticles in the range of sizes from 10-30 nm as shown in Fig. 3.4.

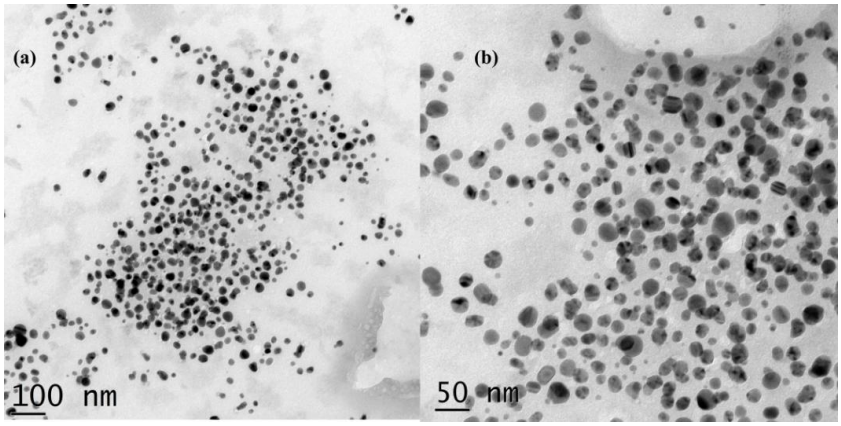

Fig. 3.4 TEM images of Ag 3 NPs (a) 100 nm scale (b) 50 nm scale

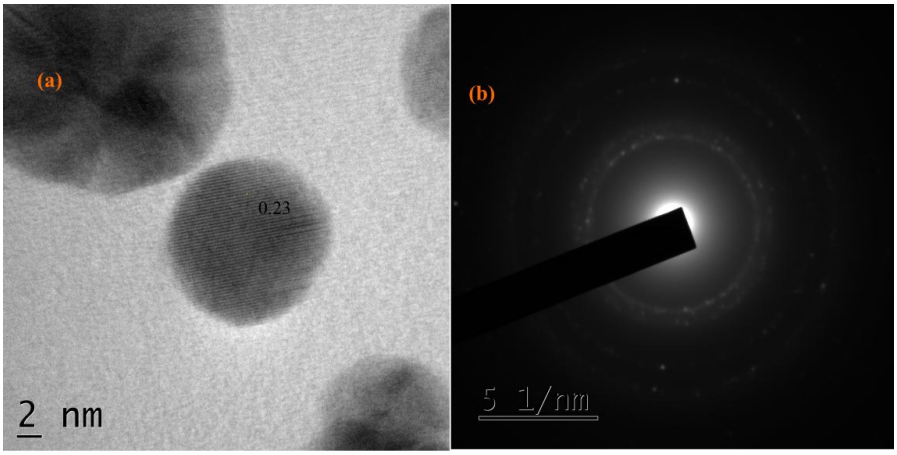

Fig. 3.5 HRTEM image of Ag3 NPs (a) fringe spacing (b) SAED pattern

The HRTEM image shows (Fig. 3.5) the fringe spacing of 0.23 nm corresponding to 111 plane of silver emphasing its crystalline nature [11]. The presence of bright circular rings in the SAED pattern confirms the polycrystalline nature of the synthesized sample.

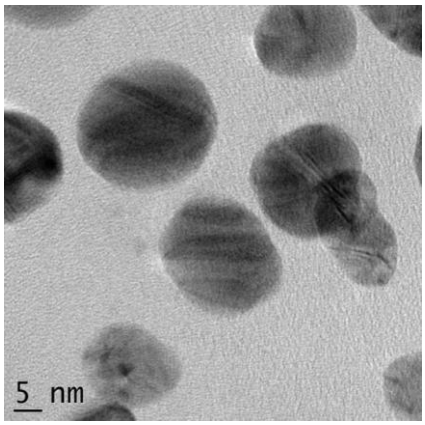

Fig.3.6 Twinning effect of Ag3 nanoparticles

It is seen that certain regions of the nanoparticle are darker than others due to a defect in fcc crystals known as twinning. Twinning arises due to sharing of a common crystallographic plane by two subgrains [12]. The presence of twinning in the Ag nanoparticles further proves the crystallite nature of the synthesized silver nanoparticles.

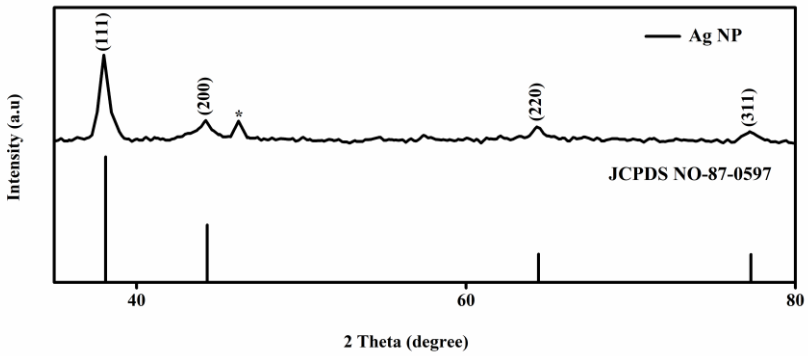

Fig.3.7 XRD spectrum of Ag3 NPs with JCPDS data

The XRD pattern of the synthesized silver nanoparticles using guava leaf extract is recorded and the spectrum is shown in Fig.3.7.The peaks are broadened indicating smaller crystallite size of the nanoparticles. The peaks are indexed as (111), (200), (220), (311) planes of FCC silver by comparing with the JCPDS data. Apart from these peaks corresponding to Ag NPs an additional unassigned peak around 46 degrees is also seen. This peak may be due to the formation of bio-organic components /metallo-proteins that are present in the leaf extract. Similar findings have been reported previously also [13].

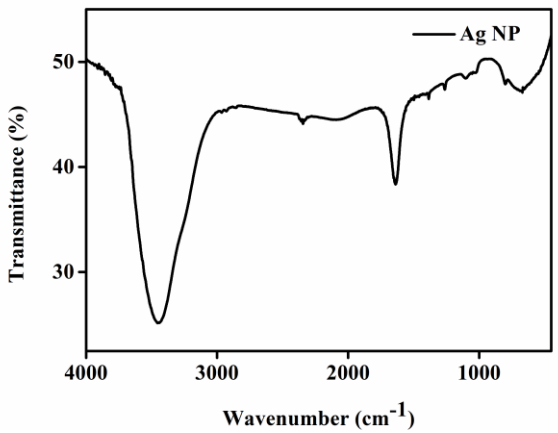

Fig. 3.8 FTIR spectrum of Ag3 NPs

FTIR peaks at 3439(–OH), 2973(C–H), 1635(C=O), 1367 (N–O), 1015 (C–O), 680 (R–CH) in Fig.3.8 represent the different functional groups present with nanoparticles after reduction. The OH peak at 3441 cm^{-1} is sharper compared to guava leaf FTIR in Fig.3.1b due to the consumption of OH ions in the reduction of Ag^{+} ions. The enol form present in tannins and flavonoids is changed to the quinonoid form after reduction resulting in the shifting of the –OH group peak to a higher frequency from 3398 to 3439cm^{-1}.Further a shift towards higher frequency has been noticed in all the FTIR peaks of Ag NPs confirming the reduction of the silver nitrate solution by the leaf extract [6].

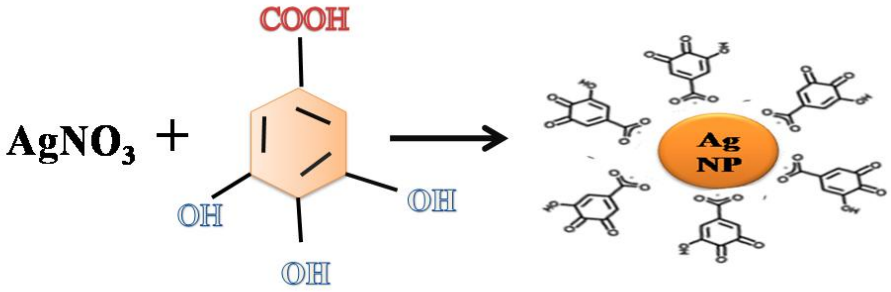

Scheme1. Mechanism of formation of Ag Nanoparticles

The free hydroxyl groups present in the reducing agent are responsible for the reduction of metal and carboxylic groups act as capping agent. The $AgNO_3$ is dissociated into Ag^{+} and nitrate ions which reacts with hydroxyl groups attached to the aromatic ring carbon atoms facilitating reduction of silver ions to silver nanoparticles. Thus, the gallic acid underwent two-electron oxidation to the corresponding quinone form and the nanoparticles formed were stabilized through the interaction of the carboxylic acid group as shown in Scheme1.

3.1.4 Conclusion

Stable Silver nanoparticles have been synthesized through an environment friendly green chemistry approach. The leaf extract of guava leaf was used as a reducing and stabilising agent and the whole reaction takes place in room temperature. The UV –Vis and DLS measurements were conducted to measure the tentative size and distribution of the synthesized AG NPs. It was found that 1 to 20 ratio (Ag 3) of leaf extract to precursor solution showed lower size and size distribution compared to 1 to 5 and 1 to 10 volume ratios. TEM analysis shows that the nanoparticles are quasi-spherical and sizes range from 10-30 nm. These nanoparticles show fringes indicating its crystalline structure which is further confirmed from XRD measurements. Finally the role of biomolecules as reducing /capping agent is demonstrated by FTIR measurements. These highly stable colloids of silver nanoparticles are highly suitable for various industrial and biological applications.

3.2 Synthesis of Gold nanoparticles (Au NP)

3.2. 1 Introduction

The synthesis of coloured gold colloids has fascinated human mind and captured the attention of the scientific community due to its extremely appealing nature [14]. Gold nanoparticles have shown tremendous application in catalysis, biotechnology, medicine, industry and solar cells because of their unique optical, electrical and catalytic properties [15]. To utilise and optimise the various physical and chemical properties it is necessary to control their shape, size, structure, composition and dielectric environment [16]. The plasmonic gold nanoparticles (AuNPs) characterized by their strong interaction

with resonant photons due to surface plasmon resonance (SPR) have seen a burst of research activity in the area of synthesis and functionalisation of nanoparticles to get desired structures with novel functionalities [17]. Due to these versatile properties, colloidal solutions of gold have different colours in visible spectrum when they are well spaced in comparison to aggregated ones.

The ruby red colour symbolised colloidal gold solutions containing uncoagulated particles with diameters less than 40 nm supported by a sharp absorption band around 530 nm [18]. SPR peak could be systematically tuned by changing the size and structure of AuNPs which could be used to design unique nanostructures that interact with the entire solar spectrum. An important development in this regard is assembly of nanoparticles into aggregates of different shapes and sizes by employing various strategies like *in situ* formation of gold aggregates and induced formation of already formed gold nanoparticles by external agents [19-24]. In addition black coloured stable gold nanoparticles have been reported by Liu *et al.* [25] which show broadband absorption and interesting 3D morphology synthesized using reverse emulsion system. The highlight of this work is the rarely reported synthesis of black gold colloid using green chemistry approach. In the recent times green chemistry methods have been used extensively for the synthesis of metal nanoparticles because of their eco-friendly approach [26, 27]. Inspite of many reports on green synthesis of gold nanoparticles [28-32] there is plenty of scope for research owing to the rich biodiversity of plants. The increase in size of gold nanoparticles by changing the concentration of reducing agent has been reported previously using trisodium citrate [33]. Here the multiple role of leaf extract of *Psidium guajava* as a reducing, stabilising and aggregation inducing agent has been

explored. Though the green synthesis of gold nanoparticles have been reported previously [34], this paper reports one of the fastest synthesis (almost instantaneous) of monodisperse red gold nanoparticles and black gold superstructures with a simple lab procedure having high rate of reproducibility and reliability for large scale productions in future.

3.2.2 Experimental

3.2.2.1 Materials

- $HAuCl_4$ (Spectrochem, India)
- Distilled water (Millipore System)
- Fresh mature leaves of Guava tree

3.2.2.2 Method

The fresh mature leaves of guava were washed, cut into small pieces and dried in air for some time to remove excess of water. Leaf extract was prepared by boiling and stirring the leaves in distilled water following the same procedure as reported in section 3.1.2.2 of this chapter [35].

For synthesis of gold nanoparticles 1 mL (Au1), 2 mL (Au2) and 3 mL (Au3) of extract were added to 3 ml of 1 mM of $HAuCl_4$ solution and stirred for two minutes at room temperature to ensure uniform mixing. The instant colour change of the pale yellow gold salt solution implies the formation of gold nanoparticles. The sample Au1 shows reddish pink colour whereas samples Au2 and Au3 show black colour indicating variation from Au1 (Fig. 3.9).

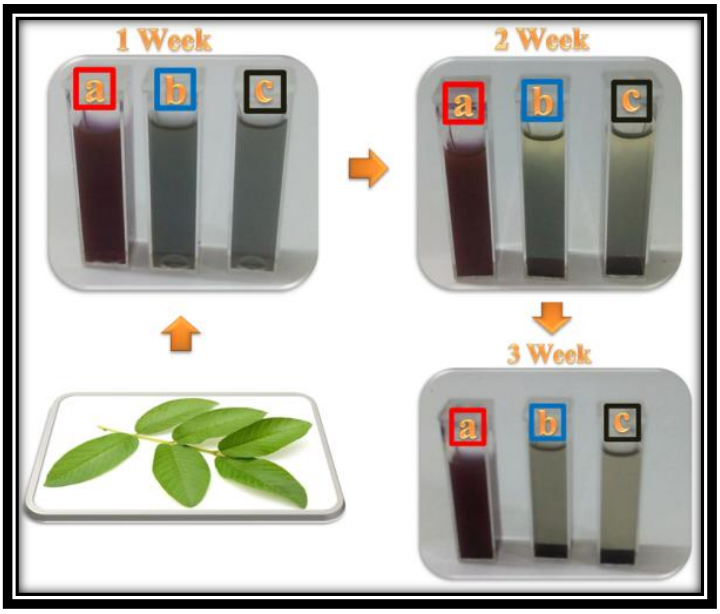

Fig.3.9 Guava leaf synthesised gold nanoparticles (a) Au1 (b) Au2 (c) Au3

3.2.3 Results and Discussion

Structure and crystallinity of Au nanoparticles are confirmed using XRD measurements by dropcasting them on a glass substrate. The diffraction peaks can be indexed to the (111), (200), (220) and (311) reflections of the cubic structure of the metallic gold, confirming its crystalline structure (Fig. 3.10). The minor peaks are not clear due to the amorphous nature of the glass substrate on which the aqueous solution has been dropcasted.

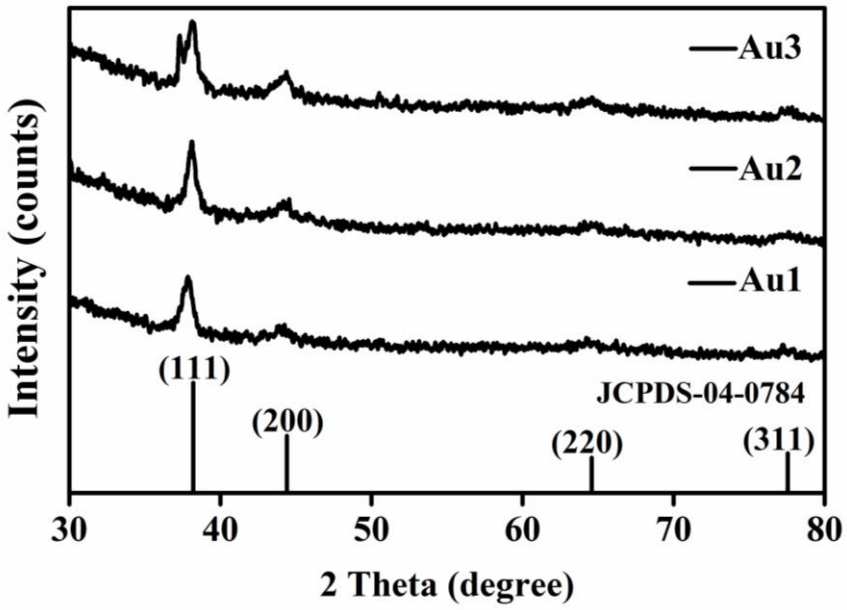

Fig. 3.10 XRD of gold colloids drop-casted on glass substrate

The presence of biomass residues present in the guava leaf extract are responsible for the extra peak at 38◦ in Au3 sample [25].From the XRD measurements, crystallite size (D) was found using Debye-Scherrer formula

$$D = 0.9\lambda/\beta Cos\theta \qquad (1)$$

Where λ is the wavelength of x-ray radiation, β is the full width at half maximum and θ is the Bragg angle. The crystallite size calculated for the samples vary from 11.6 nm to 13.7nm for Au1, Au2 and Au3 due to the difference in size/shape of the samples.

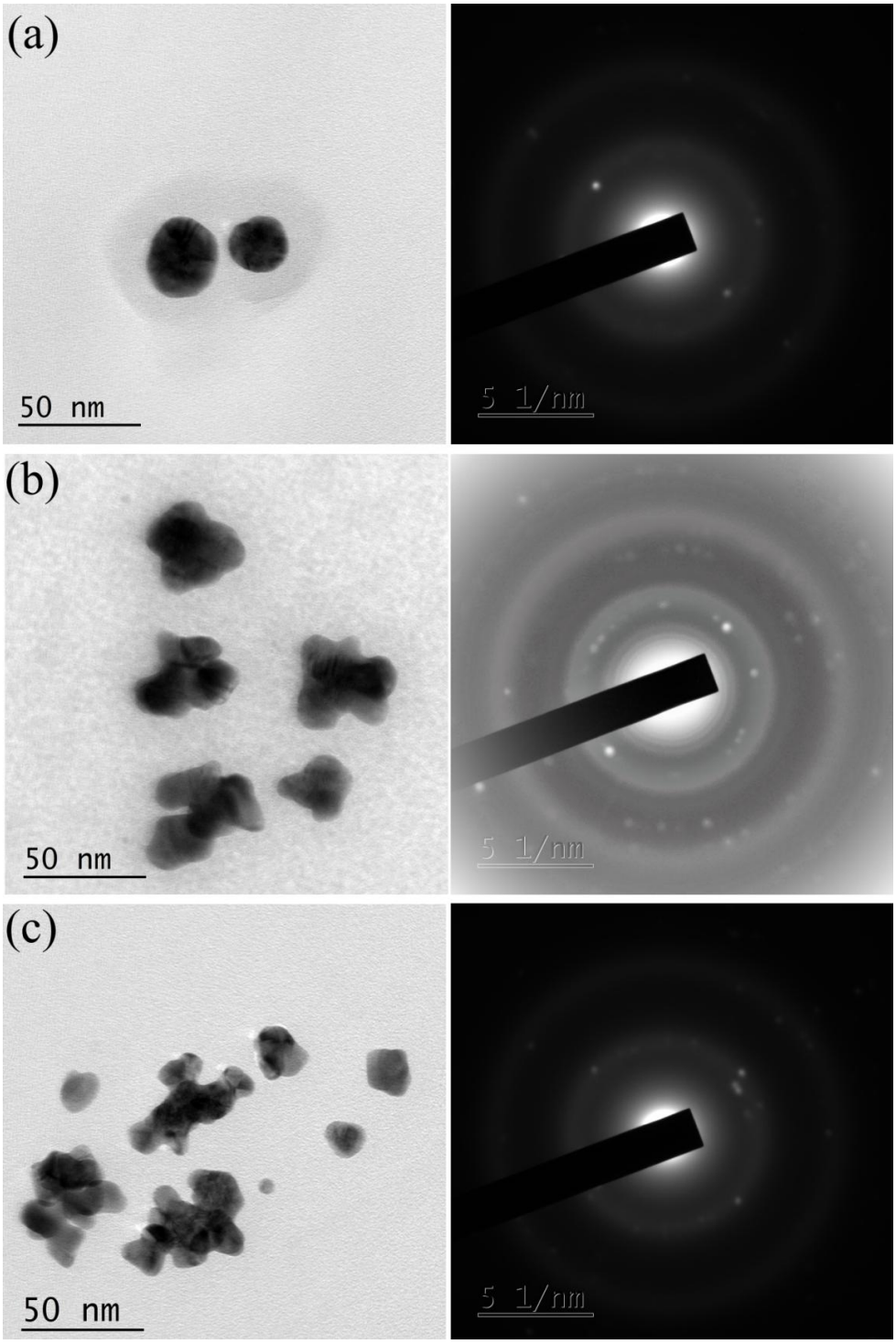

Fig. 3.11 TEM images and SAED of (a) Au1 (b) Au2 (c) Au3

In order to identify the effect of concentration of reducing agent on the size of Au NPs, TEM images (Fig.3.11) were obtained along with the SAED pattern. Consequently the organic layer acts as a barrier providing electrostatic repulsion and a steric hindrance between Au NPs thus preventing individual particles from coagulating. The Au1 NPs showed well separated quasi-spherical sized particles and show an outer coating due to the biomolecules of the reducing agent adsorbed onto the gold surface.g. The closer view shows about 5-6 nanoparticles in each nanostructure in Au2 and about 10-15 nanoparticles in each aggregate of Au3. The individual nanoparticles in the aggregate are smaller than Au1 nanoparticles (Fig.3.12a). The increase in reducing agent causes decrease in size of individual nanoparticles which is in agreement with the literature available on green synthesis of gold nanoaparticles [36]. There is almost no gap between adjacent particles which indicates that there is a strong cross-linking interaction directing the nanoparticles into self assembled aggregates.

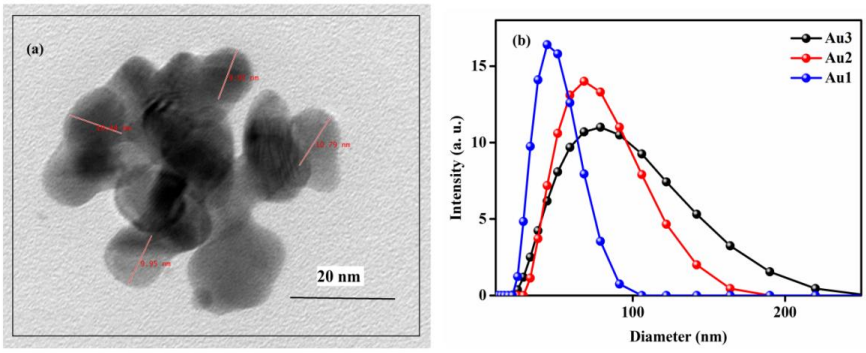

Fig. 3.12 **(**a) Aggregate structure of Au3 (b) DLS size distribution of Au 1, Au2, Au3

The DLS measurements reveal the hydrodynamic diameters of Au NPs and aggregates (Fig.3.12b). The DLS diameters are usually bigger than TEM data but give an idea of the distribution. The Au1 colloid shows a narrow

distribution (below 100 nm) indicating monodisperse particles of similar sizes. The distribution broadens gradually for Au2 and Au3, as size increase from isolated nanoparticles to self assembled aggregates.

The FTIR spectra of the guava leaf extract and of the synthesized Au NPs have been shown in Fig.3.13. FTIR peaks at 3422 (OH), 2927(OH), 1619 (C=O), 1221 and 1063 (C-O) and 611(R-CH) cm^{-1} represent the various functional groups present in the guava extract (Fig.3.13a). The synthesized Au NPs show peaks at 3449 (OH), 1640 (C=O), 1036 (C-O) and 666 (R-CH) cm^{-1}corresponding to different peaks present with the extract after reduction. The binding of carboxylic moiety to the nanoparticle surface is expressed by the disappearance of the band at 2927 cm^{-1} in Fig. 3.13(b) corresponding to OH stretching vibration of carboxylic group. In both FTIR spectra the OH peak at around 3100-3400 cm^{-1} is dominant due to the presence of OH groups in gallic acid, flavonoids and eugenol present in the extract of guava leaf [6, 37]. The broad absorption band in 3100-3400 cm^{-1} in Au2 and Au3 could be due to the intermolecular hydrogen bonded network of phenolic groups present on the surface of the nanoparticle.

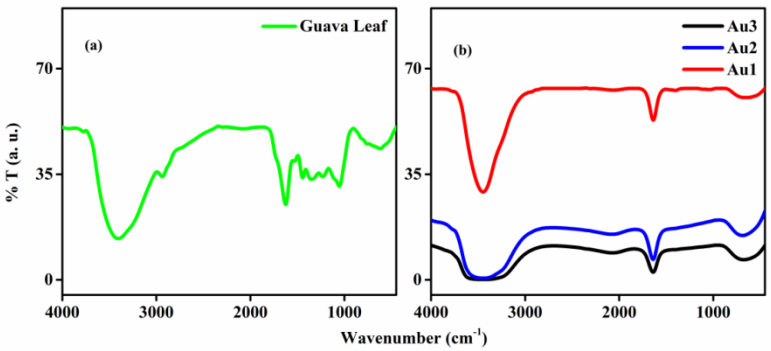

Fig. 3.13 FTIR spectra of (a) Guava leaf extract (b) Au1, Au2 and Au3

On the basis of FTIR analysis a mechanism is being proposed for the self-assembly of gold nanoparticles. The phytochemicals gallic acid and quercetin (flavonoid) are reported to show aggregation of Au NPs when their quantity as reducing agent is increased [38, 39].Both of these phytochemicals contain hydroxyl and carboxyl groups responsible for hydrogen bonding with similar groups of the adjacent molecules. Here the hydroxyl groups in the gallic acid are presumed to take part in the reduction of gold ions to metallic gold by undergoing oxidation to its quinine analogue and the carboxylic acid bind to the surface of the Au nanoparticles by taking the role of a capping agent to keep the system stabilized. The gold nanoparticles generally will have surface functional groups yielding a negative charge resulting in repulsive interparticle forces ensuring colloidal stability. In the case of Au1 the decrease in pH of the medium (from pH 5 of the extract to pH 3 of the colloid) shows that most of the gallic acid underwent two electron oxidation to corresponding quinone form yielding better stability. With further addition of the extract both gallic acid and its quinone form co-exists in the solution. The strong intermolecular and intramolecular hydrogen bonding between these two are likely to be responsible for the formation of aggregates and consequently lesser stability of Au2 and Au3. In the schematic diagram (Fig.3.14) Au1 has been shown capped by quinone form but Au2 and Au3 is represented using both quinone and gallic acid and the hydrogen bonding has been depicted. Thus at higher concentration of the extract the repulsive forces decreases, interparticle distance becomes narrower through hydrogen bonding to form self assembled aggregates. A similar work, where increase in capping agent causing formation of aggregated nanostructures has been reported by Sen et al [40]. The capping agent in that

work was MPA and colour of aggregated nanostructures was light blue. As guava leaf is rich in various phytochemicals, we are able to obtain unique black coloured gold aggregates due to the synergetic effect of the reducing and capping agents present in the leaf extract. The proposed model is further justified as the size of the aggregates increases with increased concentration of the extract.

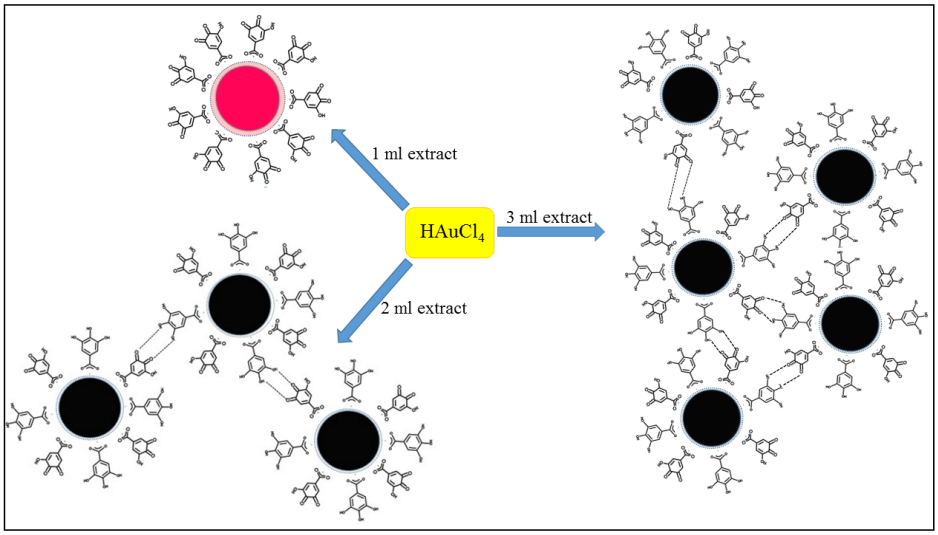

Fig. 3.14 Schematic of self assembled Au nanostructures through hydrogen bonding

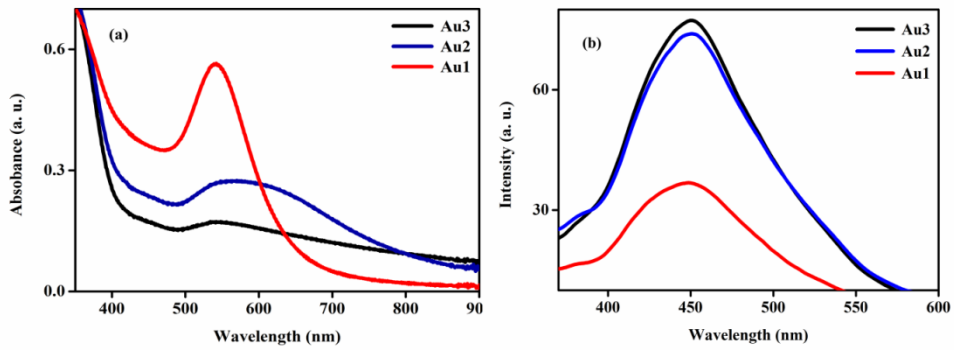

Fig. 3.15 (a) UV-Vis spectra of the gold colloids (b) PL spectra of Au1, Au2 and Au3

The reduction of precursor salt can be visually assessed by the instant change of colour from pale yellow precursor solution to red or black depending

on the concentration of plant extract added. The formation of nanoparticles was confirmed from UV-vis absorbance spectrum (Fig. 3.15a) as it is a conventional method to probe the stability, surface chemistry and aggregation behaviour of the AuNPs formed. The monodispersed Au1 nanoparticles exhibit a well defined sharp peak around 539 nm showing good agreement with the reported SPR band of Au NP [41]. Broad peaks with reduced intensity had been observed with increasing extract quantity indicating the formation of aggregates in solution. The dense organic molecules present in the extract adsorbed on the surface of Au NPs significantly change the interface conditions leading to a sharp decrease in the intensity of SPR absorption. The broadening in SPR is due to the damping of the SPR caused by the combined effect of increase in particle size and shape of Au NPs in colloidal solutions. The formation of gold particle assembly leads to an increase in dielectric constant of the surrounding medium, hence shifting the plasmon peak to a lower energy [42].The Au1 shows very good stability for few weeks and Au2 and Au3 show stability for a week at room temperature, but they are stable for a longer period when kept at 4°C.

The PL studies conducted at an excitation wavelength of 340 nm showed that all the Au colloids were found to be luminescent in the visible range showing peak around 450 nm (Fig.3.15b). The luminescent emission of guava extract in the above range is likely to responsible for the fluorescent emission of the gold colloids. The aggregates, Au2 and Au3 showed higher PL emission when compared to monodisperse Au1. The fluorescent properties of the gold colloids can be exploited as nanosensor, detectors and as fluorescent probe in cancer cell imaging applications [43-45].

3.2.4 Conclusions

An environment friendly green approach has been used to synthesize red and black gold colloidswith different size and morphologies using the leaf extract of guava tree. The phytochemicals present in the extract acts as a reducing, capping and aggregation inducing agent for the gold nanostructures in the red and black colloids. At lower extract concentrationred colloids with near spherical particles around 20-30 nm are obtained. But as the concentration of leaf extract is increased, black colloid having aggregates composed of sizes between 35-55 nm are formed. The colour change that occurs from aggregation leads to varied optical properties offering possibilities for diverse applications in optoelectronics. At lower extract concentration most of the gallic acid is oxidized to its quinone form by reducing the gold ions to form stable red colloids. Formation of black gold aggregates at high extract concentration is contributed by the strong intermolecular and intramolecular hydrogen bonding between gallic acid and its quinone present in the medium. Tunability of various physical and optical properties by varying the size and shape of metallic colloids are likely to open up new directions in several domains of current research and technologies.

3.3 Synthesis of Natural Dyes

3.3.1. Introduction

Dye sensitized solar cells (DSSC) provides a technically and commercially viable alternative concept to the conventional solar cell technologies since first reported by O Regan and Grätzel [46]. In DSSC a wide bandgap oxide semiconductor acts a photoanode which accepts electrons from the

photoexcited dye/sensitizer. The dye molecule is regenerated by the redox system which itself is regenerated at the counter electrode by the electrons passing through the load. Hence the efficiency of DSSC can be improved by increasing absorption of photons by a photo sensitizer/dye to a large extent [47]. The ideal sensitizer for a solar cell converting standard Air Mass (AM1.5) should absorb all light below a threshold wavelength of about 920 nm. In addition, it must have strong adsorption to the semiconductor metal oxide surface, efficient electron injection onto the conduction band of metal oxide, must be rapidly regenerated to avoid recombination process and be fairly stable. The best photovoltaic performance both in terms of conversional yield and stability has been achieved by the poly-pyridyl complex of Ruthenium [48].

However the use of expensive Ruthenium complexes extracted from scarce natural resources provides ample space for researchers to experiment with natural pigments as sensitizing dyes for conversion of solar energy to electrical energy. The natural dyes have an added advantage of being in abundant supply, environment friendly and relatively cheap methods of preparation [49]. These pigments are extracted from fruit, leaves, flowers and roots of plants. A plant pigment is a type of coloured chemical substance produced by plants which absorb visible radiation between 380 to 780 nm.

The major types of plant pigments classified according to colour are chlorophylls, anthocyanins, betalains and cartenoids. Chlorophylls absorb red and blue light from sunlight and hence appear green. The chlorophyll molecules ($C_{55}H_{70}MgN_4O_6$) are large in size. They are not soluble in aqueous solution that fills the plant cells, but attached to disc like structures called

chloroplasts inside cells. Chlorophyll is an attractive candidate for being photosensitizer and efficiencies above 4% have been reported [50].The photoelectric conversion efficiencies of DSSC with chlorophyll dye as sensitizer extracted from spinach [51] and pomegranate leaves [52] are 0.49 and 0.59 % respectively.

Anthocyanins are coloured water soluble natural pigments widely used as photosensitizers in DSSC [53].Betalains are a class of red–violet (betacyanins) andyellow (betaxanthins) pigments that are present in plants of caryophyllales. The common major sources of betalains are plants of amaranthacea, redbeet, bougainvillea and cactacea[54].Cartenoids are another class of yellow and yellow orange pigments used as photosensitizers in DSSC [55].

There have been studies comparing efficiencies of anthocyanins, betalains and chlorophyll extracted from different plants [56-61]. This investigation reports extraction of betalain and chlorophyll from a single leaf which has been rarely reported. Water and ethanol used as solvents for a single dye in previous reports [57, 59] have extracted different dyes in this work. The previous report on red amaranth as natural sensitizer in DSSC by J. Uddin *et al* [61] have separated the various components using chromatography but the efficiencies reported are low and the individual coloured pigments were not classified. In this paper two natural dyes namely chlorophyll and betalain from leaves of red amaranth were used as photosensitizers for DSSC. The extracted dyes were characterized by UV-Vis absorption spectra and their structures confirmed through FTIR spectra.

3.3.2. Experimental

3.3.2 1 Materials

- ❖ Distilled water (Millipore System)
- ❖ Leaves of red amaranth (*Amaranthus tricolour* L),

3.3.2 2 Method

The leaves of red amaranth (Fig.3.16a) was washed and cleaned, cut into small pieces prior to extraction. The dye was extracted by adding the leaves to the respective solvent and heated with stirring at 60^{o}C for 15 minutes. The resulting solution was filtered using syringe filter (0.2µm) and stored at 4^{o}C for further experiments. The dye was extracted using two solvents namely DI water and ethanol (Fig.3.16b).The dyes extracted showed different colours namely red-violet with distilled water and green with ethanol showing the presence of two different pigments.

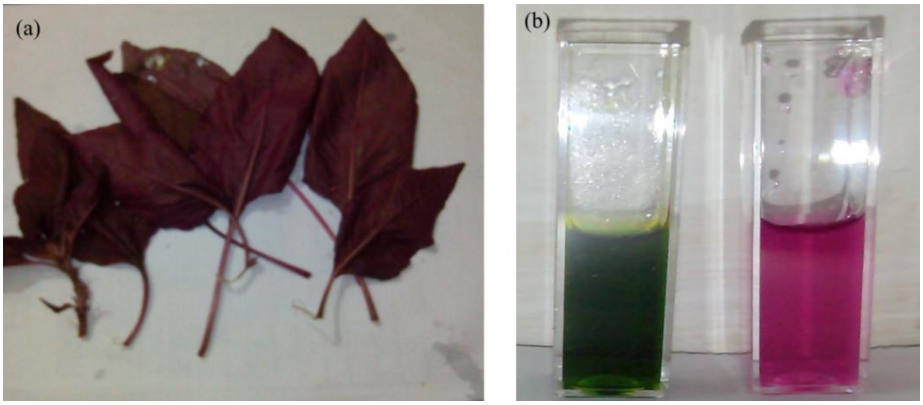

Fig. 3.16 (a) Red amaranth leaves (b) Extract of red amaranth in ethanol (green), water (pink)

3.3.3 Results and Discussion

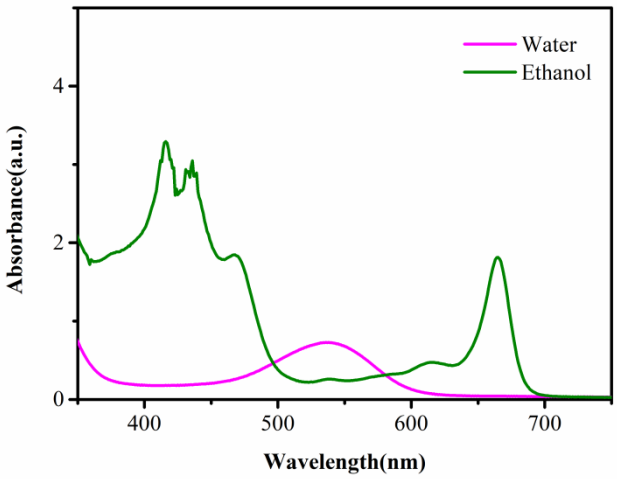

Fig.3.17 UV-Vis absorption spectra of dyes extracted from red amaranth leaves

Dyes extracted using different solvents show different absorption peaks in the UV-Vis absorption spectra. The difference in the absorption spectra is due to the presence of different photosynthetic pigments in the leaves of red amaranth in the visible spectrum (400-700 nm). From Fig.3.17 the absorption peaks of the dye in ethanol can be seen at a wavelength of 415,438 and 664 nm, for distilled water a single peak located at 536 nm was observed.

The absorption peak observed in the wavelength range of 400-440 and 660 nm indicate the presence of chlorophyll pigment whereas peak around 536nm attributes to betalain pigment [62-66]. The ethanol based extraction of chlorophyll showed better and broader absorption in the visible range of the electromagnetic spectrum. The molecular structure of chlorophyll and betalain are shown in Fig. 3.18.

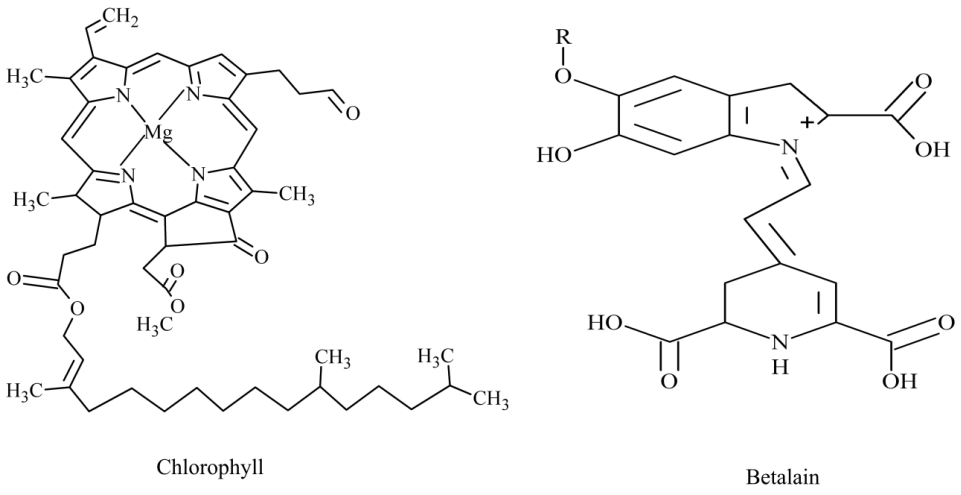

Fig.3.18 Molecular structure of chlorophyll and betalain dyes

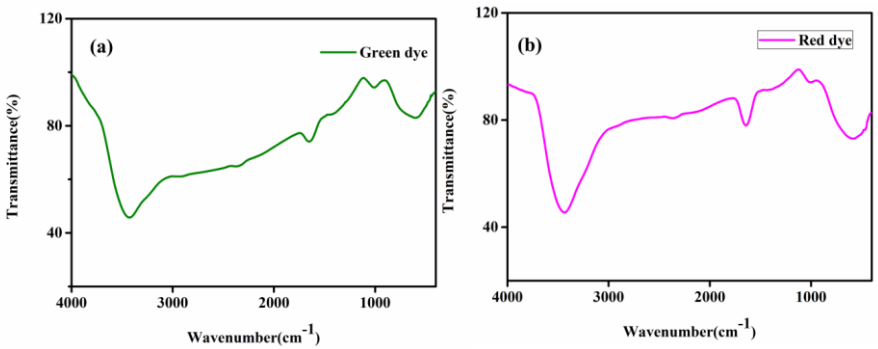

Fig.3.19 The FTIR spectra of (a) Chlorophyll dye (b) Betalain dye

The structure of the isolated dyes was confirmed by its FTIR spectra (Fig.3.19). The chlorophyll dye exhibits OH group stretching vibrations at 3438 cm^{-1} ,C-H vibrations of CH_3 and CH_2 groups at 2904 cm^{-1} and 2848 cm^{-1} ,C=O stretching vibrations at 1644 cm^{-1} and C-O vibrations at 1045 cm^{-1}[67].The betalain dye exhibits OH and NH stretching vibrations indicating H bonding at 3423 cm^{-1}, CH stretching vibrations at 2930 $cm^{-1}$and 2835 cm^{-1} due to CH groups, C=N stretching vibrations at 2362 cm^{-1},C=O stretching vibrations at 1638 cm^{-1},C-N-C bending vibrations at 1375 cm^{-1},C-O stretching vibrations 1057 cm^{-1} and C-H bending vibrations at 591 cm^{-1}[68].

3.4 Conclusion

Two different coloured dyes from the red amaranth leaf were extracted and used as photosensitizers for DSSC. These dyes were obtained by a simple cost effective lab method. The UV- Vis and FTIR measurements conducted indicate that the dyes extracted using water and ethanol are betalain and chlorophyll respectively. The chlorophyll dye showed good absorption in the visible region as compared to betalain dye. Overall the leaf of red amaranth shows great promise as a potential source of natural dyes in future.

References:

[1] K.L. Kelly, E. Coronado, L.L. Zhao ,G.C. Schatz, The optical properties of metal nanoparticles: The influence of size ,shape and dielectric environment, J. Phy. Chem 107 (2003) 668-677.

[2] Yu A Krutyakov, A A Kudrinskiy, A Yu Olenin, G V Lisichkin, Synthesis and properties of silver nanoparticles, advances and prospects, Russian Chemical Reviews 77 (2008) 233-257.

[3] S.Iravani, Green synthesis of metal nanoparticles using plants, Green Chem. 13 (2011) 2638-2650.

[4] V.K. Sharma, R.A. Yngard, Y. Lin, Silver nanoparticles: Green synthesis and their antimicrobial activities, Adv. Colloid Interface Sci. 145 (2009) 83-96.

[5] D. Raghunandan , B. D. Mahesh, S. Basavaraja , S. D. Balaji ,S. Y. Manjunath , A. Venkataraman,Microwave-assisted rapid extracellular synthesis of stable bio-functionalized silver nanoparticles from guava (Psidiumguajava) leaf extract,J Nanopart Res ,13 (2011) 2021–2028.

[6] U. K. Parashar, V. Kumar, T. Bera, P. S. Saxena, G. Nath, S. K. Srivastava, R. Giri, A. Srivastava, Study of mechanism of enhanced antibacterial activity by green synthesis of silver nanoparticles, Nanotechnology 2011 (22) 1-13.

[7] H. Arima, G. Danno, Isolation of antimicrobial compounds from guava (Psidiumguajava L.) and their structural elucidation, Biosci. Biotechnol. Biochem. 66(8) (2002), 1727-1730.

[8] W. Haiss, N. T. K. Thanh, J. Aveyard, D. G. Fernig, Determination of Size and Concentration of Gold Nanoparticles from UV-Vis Spectra, Anal. Chem 79 (2007) 4215-4221.

[9] S. Agnihotri, S. Mukherji, S. Mukherji, Size-controlled silver nanoparticles synthesized over the range 5–100 nm using the same protocol and their antibacterial efficacy, RSC Adv., 2014, 4, 3974-3983.

[10] G. V. White II, P.Kerscher, R. M. Brown, J. D. Morella, W. McAllister, D. Dean, C. L. Kitchens, Green synthesis of robust biocombatible silver nanoparticles using garlic extract, Journal of Nanomaterials, 2012 (2012) 1-12.

[11] M. R. Dasa, R. K. Sarmab, R. Saikiab, V. S. Kalec, M. V. Shelkec, Pinaki Sengupta,Synthesis of silver nanoparticles in an aqueous suspension of graphene oxidesheets and its antimicrobial activity,Colloids and Surfaces B: Biointerfaces 83 (2011) 16–22.

[12] M. R. Bindhu, M. Umadevi, Surface plasmon resonance optical sensor and antimicrobial activities of biosynthesized silver nanoparticles, SpectrochimicaActa Part A: Molecular and Biomolecular Spectroscopy 121 (2014) 596-604.

[13] L. Christensen, S. Vivekanandhan, M. Misra, A. K. Mohanty,Biosynthesis of silver nanoparticles using murrayakoenigii (curry leaf): An investigation on the effect of broth concentration in reduction mechanism and particle size, Adv. Mat. Lett. 2 (2011) 429-434.

[14] J. Turkevich, P.C. Stevenson, J. Hiller, A study of the nucleation and growth processes in the synthesis of colloidal gold, Discuss. Faraday. Soc. 11 (1951) 55-75.

[15] S.K. Ghosh, T. Pal, Interparticle coupling effect on the surface Plasmon resonance of gold nanoparticles: From theory to applications, Chem. Rev. 107 (2007) 4797-4862.

[16] P.K. Jain, K.S. Lee, I.H. El-Sayed, M.A. El-Sayed, Calculated absorption and scattering properties of gold nanoparticles of different size, shape and composition: Application in biological imaging and medicine, J. Phys. Chem. B 110 (2006) 7239-7248.

[17] F. Gambinossi, S.E. Mylon, J.K. Ferri, Aggregation kinetics and colloidal stability of functionalized nanoparticles, Adv. Colloid Interface Sci. 222 (2015) 332-349.

[18] J. Turkevich, Colloidal Gold. Part II, Gold Bull. 18 (1985) 125-131.

[19] S.L. Westcott, S.J. Oldenburg, T.R. Lee, N.J. Halas, Construction of simple gold aggregates with controlled plasmon – plasmon interactions, Chem. Phys.Lett. 300 (1999) 651-655.

[20] Y. Chegel, O. Rachkov, A. Lopatynsk, S. Ishihava, I. Yanchuk, Y. Nemoto, J.P. Hill, K. Ariga, Gold nanoparticles aggregation ;drastic

effect of cooperative functionalities in a single molecule conjugate, J. Phys. Chem. C 116 (2012) 2683-2690.

[21] C. Yang, H. Sui, X. Li, J. Han, X. Luo, X. Zhang, Haizhu. Sun, Hongchen. Sun, Y. Zhou, B. Yang, Gold nanoparticle superstructures with enhanced photothermal effect, Cryst. Eng. Comm. 15 (2013) 3490-3497.

[22] C.C. Chen, P.L. Kuo, Y.C. Cheng, Spherical aggregates composed of gold nanoparticles, Nanotechnology 20 (2009) 1-7.

[23] R. Raliya, P. Biswas, Environmentally benign bio-inspired synthesis of Au nanoparticles, their self assembly and agglomeration, RSC. Adv. 5 (2015) 42081-42087.

[24] J. Liao, Y. Zhang, W. Yu, L. Xu, C. Ge, J. Liu, N. Gu, Linear aggregation of gold nanoparticles in ethanol, Colloids Surf. A 223 (2003) 117-183.

[25] D. Liu, F. Zhou, C. Li, T. Zhang, H. Zhang, W. Cai, Y. Li, Black gold: Plasmoniccolloidosomes with broadband absorption self-assembled from monodispersed gold nanospheres by using a reverse emulsion system, Angew. Chem. Int. Ed. 54 (2015) 9596-9600.

[26] M.S. Akhtar, J. Panwar, Y.S. Yun, Biogenic synthesis of metallic nanoparticles by plant extracts, ACS Sustainable Chem. Eng. 1 (2013) 591-602.

[27] A.K. Mittal, Y. Chisti, U.C. Banerjee, Synthesis of metallic nanoparticles using plant extracts, Biotechnol. Adv. 31 (2013) 346-356.

[28] S.L.Smitha, D. Philip, K.G.Gopchandran, Green synthesis of gold nanoparticles using *Cinnamomumzeylanicum* leaf broth, Spectrochim.Acta Part A 74(2009) 735-739.

[29] B. Sadaghi, M. Mohammadzadeh, B. Babakhani, Green synthesis of gold nanoparticles using *Stevia rebaudiana* leaf extracts: Characterization and their stability, J. Photochem. Photobiol. B: Biology 148 (2015) 101-106.

[30] J. Kasthuri, S. Veerapandian, N. Rajendiran, Biological synthesis of silver and gold nanoparticles using apiin as reducing agent, Colloids and Surf. B: Biointerfaces 68 (2009) 55-60.

[31] C. Tamuly, M. Hazarika, S.Ch Borah, M.R. Das, M.P. Boruah, In situ biosynthesis of Ag, Au and bimetallic nanoparticles using Piper pedicellatum C.DC: Green chemistry approach, Colloids and Surf. B: Biointerfaces 102 (2013) 627-634.

[32] D.P. Stankus, S.E. Lohse, J.E. Hutchison. J.A. Nason, Interactions between natural organic matter and gold nanoparticles stabilized with different organic capping agents, Environ. Sci. Technol. 45 (2011) 3238-3244.

[33] X. Ji, X. Song, J. Li, Y. Bai, W. Yang, X. Peng, Size control of gold nanocrystals in citrate reduction: the third role of citrate, J. Am. Chem. Soc. 129 (2007) 13939-13948.

[34] D. Raghunandan, S. Basavaraja, B. Mahesh, S. Balaji, S.Y. Manjunath, A. Venkataraman, Biosynthesis of stable polyshaped gold nanoparticles from microwave-exposed aqueous extracellular anti-malignant guava(Psidiumguajava) leaf extract, Nano Biotechnol. 5 (2009) 34-41.

[35] R. Rajita, P. Nijisha, C.V. Nivedita, S. Sindhu, Natural dyes from red amaranth leaves as light harvesting pigments for dye sensitized solar cells, Mater Res. Bull 90 (2017) 156-161.

[36] X. Huang, H. Wu, X. Liao, B. Shi, One-step, size controlled synthesis of gold nanoparticles at room temperature using plant tannin, Green Chem. 12 (2010) 395-399.

[37] E. Diaz-de-Cero, V. Verardo, A.M.G. Caravaca, A.F. Gutierrez, A.G. Carretero, Determination of polar compounds in guava leaves infusions and ultrasound aqueous extract by HPLC-ESI-MS, J. Chem. 2015 (2015) 1-9.

[38] K. Yoosaf, B.I. Ipe, C.H. Suresh, K.G. Thomas, In situ synthesis of metal nanoparticles and selective naked eye detection of lead ions from aqueous media, J. Phys. Chem. C 111 (2007) 12839-12847.

[39] K.A. Rawat, S.K. Kailasa, Visual detection of arginine, histidine and lysine using quercetin functionalized gold nanoparticles, Microchim Acta 181(2014) 1917-1929.

[40] T. Sen, A. Patra, Formation of self assembled Au nanoparticles and the study of their optical properties by steady state and time resolved spectroscopies, J. Phys. Chem. C 113 (2009), 13125-13132.

[41] S. Shankar, L. Jaiswal, R. S. L. Aparna, R. G. S. V. Prasad, Synthesis, characterization,in vitro biocompatibility,and antimicrobial activity of gold, silver and gold silver alloy nanoparticles prepared from Lansium domesticum fruit peel extract, Material Letters 137 (2014) 75-78.

[42] P.Galleto, P.F. Brevet, H.H. Girault, R. Antoine, M. Broyer, Enhancement of the second harmonic response by adsorbates on gold

colloids: The effect of aggregation, J. Phys. Chem. B 103 (1999) 8706-8710.

[43] J. Zhang, C. Zhou, M. Yu, J. Liu, Different sized luminescent gold nanoparticles, Nanoscale 4 (2012) 4073-4083.

[44] C.C. Huang, Z. Yang, K.H. Lee, H.T. Chang, Synthesis of highly fluorescent gold nanoparticles for sensing mercury(II), Angew. Chem. Int. Ed 46 (2007), 6824-6828.

[45] H. He, C. Xie, J. Ren, Nonbleaching Fluorescence of gold nanoparticles and its applications in cancer cell imaging, Anal. Chem. 80 (2008) 5951-5957.

[46] M. K. Nazeeruddin, E. Baranoff, M. Grätzel, Dye-sensitized solar cells: A brief overview, Sol. Energy 85 (2011) 1172-1178.

[47] M. Grätzel, Conversion of sunlight to electric power by nanocrystalline dye sensitized solar cells, J. Photochem. Photobiol. A 164 (2004) 3-14.

[48] M. R. Narayan, Dye sensitized solar cells based on natural sensitizers, Renewable Sustainable Energy Rev. 16 (2012) 208-215.

[49] X-F.Wang, C-H Zhan, T. Maoka,Y. Wada, Y. Koyama, Fabrication of dye sensitized solarcells using chlorophylls c1 and c2 and their oxidized forms c1'and c2' from *Undaripinnatifida*(Wakame), Chem. Phys. Lett. 447 (2007) 79-85.

[50] M. Ikegami, M. Ozeki, Y. Kijitori, T. Miyasaka, Chlorin-sensitized high efficiencyphotovoltaic cells that mimic spectral response of photosynthesis, Electrochem. Commun.76 (2008) 140-143.

[51] R. Syafinar, N. Gomesh, M. Irwanto, M. Fareq, Y. M. Irwan, Chlorophyll pigments

as nature based dye for dye sensitized solar cells(DSSC), Energy Procedia 79 (2015) 896-902.

[52] H. Chang, Y. J. Lo, Pomegranate leaves and mulberry fruit as natural sensitizer for dye sensitized solar cells, Sol. Energy 84 (2010) 1833-1837.

[53] G. Calogero, J-Yum, A. Sinopoli, G. D. Marco, M. Grätzel, M. K. Nazeeruddin, Anthocyanins and betalains as light harvesting pigments for dye-sensitized solar cells, Sol. Energy 86 (2012) 1563-1575.

[54] Yamazaki, M. Murayama, N. Nishikawa, N. Hashimoto, M. Shoyama, O. Kurita, Utilization of natural carotenoids as photosensitizers for dye-sensitized solar cells, Sol. Energy, 81 (2007) 512-516.

[55] H. Zhou, L. Wu, Y. GaO, T. Ma, Dye sensitized solar cells using 20 natural dyes as sensitizers, J. Photochem. Photobiol. A 219 (2011) 188-194.

[56] S. Hao, J. Wu, Y. Huang, J. Lin, Natural dyes as photosensitizers for dye sensitized solar cells, Sol. Energy 80 (2006) 209-214.

[57] K. Woncharee, V. Meeyoo, S. Chavadej, Dye-sensitized solar cell using natural dyesextracted from rosella and blue pea flowers, Sol. Energ. Mat. Sol. Cells 91 (2005) 566-571.

[58] S.Ananth, P.Vivek, T. Arumanayagam, P. Murugakoothan, Natural dye extract oflawsoniainermis seed as photo sensitizer for titanium dioxide based dye sensitized solar cells, Spectrochim. Acta Mol. Biomol. Spectrosc. 128 (2014) 420-426.

[59] L. K. Singh, T. Karlo, A. Pandey, Performance of fruit extract of *Melastomamalabathricum L*. as sensitizer in DSSCs, Spectrochim. ActaMol. Biomol. Spectrosc. 118 (2014) 938-943.

[60] Lim, N. T. R. N. Kumara, A. L. Tan, A. M. Mirza, R. L. N. Chandrakanthi, M .I. Petra,L. C. Ming, G. K. R. Senadeera, P. Ekanayake, Potential natural sensitizers extracted from the skin of Canariumodontophyllum fruits for dye-sensitized solar cells, Spectrochim. Acta Mol. Biomol. Spectrosc. 138 (2015) 596-602.

[61] J. Uddin, J. M. M. Islam, E. Karim, S. M. M. Khan, S. Akhter, E. Hoque, M.A. Khan, Preparation and Characterization of Dye Sensitized Solar Cell using natural dye extract from Red Amaranth(Amaranthussp) as sensitizer, Int. J. Thin Fil. Sci. Tech. 4 (2015) 141-146.

[62] M. A. M. Al-Alwani, A. B. Mohamad , A. A. H. Kadhum, N. A Ludin, Effect of solvents on the extraction of natural pigments and adsorption onto TiO_2 for dye sensitized solar cell applications, Spectrochim. Acta Mol. Biomol. Spectrosc. 138 (2015) 130-137.

[63] Y. Cai, M. Sun, H. Corke, HPLC characterization of betalains from plants in *Amaranthacea*, J. Chromatogr. Sci. 43 (2005) 454-460.

[64] M .Biswas, S. Dey, R. Sen, Betalains from *Amaranthus TricolourL*, J. Pharmacogn.Phytochem. 5 (2013) 87-95.

[65] M. B. Ali, L. Khandaker, S. Oba, Changes in pigments,total polyphenol, antioxidant activity and color parameters of red and green edible amaranth leaves under different shade levels, J. Food Agric. Environ. (2010) 117 - 222.

[66] Y-Z. Cai, M. Sun, H. Corke, Characterization and application of betalain pigments fromplants of the Amaranthacea, Trends Food Sci. Technol. 16 (2005) 370-376.

[67] H. Chang, M-J Kao, T-L Chen, C-H Chen, K-C Cho, X-R Lai, Characterization of Natural Dye Extracted from Wormwood and Purple Cabbage for Dye-Sensitized Solar Cells, International Journal of Photoenergy ,2013 (2013) 1- 8 .

[68] D. Sengupta, B. Mondal, K. Mukherjee, Visible light absorption and photo-sensitizing properties of spinach leaves and beetroot extracted natural dyes, Spectrochim Acta A Mol Biomol Spectrosc. (2015) 1-31.

CHAPTER 4

SEMICONDUCTOR (TiO_2) - METAL NANOPARTICLE (Ag NP) HYBRID SYSTEM

SEMICONDUCTOR (TiO_2) - METAL NANOPARTICLE (Ag NP) HYBRID SYSTEM

4.1 Introduction

The ultimate goal of any solar cell technology is to achieve cost-effective power generation with optimum efficiency to meet the growing demands of the society. Nanostructure-semiconductor based solar cells are anticipated to play a major role in providing clean and green energy in future [1].DSSC (Dye Sensitized Solar Cell) assume a special place in this regard fulfilling the above requirements with a unique feature of charge generation, charge transport and charge collection by different components of the cell. Hence the focus shifts to optimised combination of materials and methods to improve individual device parameters associated with the solar cell like photoanode, dye, counter electrode, and electrolyte so as to enhance the device efficiency[2-7].Photoanode is one of the key components where research is being done to improve the photocurrent and hence efficiency of the solar cell. One of the prominent strategies is the integration of metal nanostructures to improve the overall output. Metal nanoparticles by virtue of their unique physico-chemical properties have opened doors of various possibilities for metal-semiconductor hybrid structures in photovoltaic cells, catalysis and sensing applications [8, 9].

Metal nanoparticles like silver have been extensively used in photovoltaics because of its relative stability and strong absorbance in visible region.The electromagnetic radiation causes collective oscillations of the conduction band electrons with a resonant frequency termed as Local Surface Plasmon Resonance(LSPR).The LSPR imparts significant influence on the photophysical properties on the semiconductors/dyes in the close vicinity of the

metal nanoparticles. A detailed study on the plausible interactions involving energy and electron transfer is required to evaluate the energy harvesting mechanisms occurring in the DSSC. The use of noble metal incorporated photoanodes has shown remarkable efficiencies mainly attributed to dye absorption enhancement due to LSPR [10-13].Sardar *et.al* reported silver modified photoanode and counter electrode with increased photovoltage leading to high efficiencies at about8.02% [14].Silver incorporated TiO_2 (Ag-TiO_2) photoanode in this work distinguishes itself in terms of novelty of design, ease of fabrication and competitive efficiencies. Further the role of resonant energy transfer (RET) in the vicinity of nanoparticle has been discussed along with its implications in solar cell performance, a less explored phenomenon in silver incorporated solar cells. Recently Nbelayim *et al* have reported that charge recombination is one of the major factors for not achieving very high efficiency in Ag-TiO_2 solar cells [15]. Here we are exploring the role of a non-radiative energy transfer, FRET (Förster Resonance Energy Transfer), playing a decisive role in retarding the efficiencies of hybrid solar cells.

In the present work silver nanoparticles synthesized through green method with leaf extract of guava (*Pisidium guajava*) are used to enhance photocurrent and hence efficiency of DSSC. Though silver synthesis using guava leaf extract has been previously reported [16], this study assumes significance because of its fast synthesis at room temperature with very high stability up to eight months. Further, it is carried out at room temperature and is completely green implying that no other reagent is added apart from precursor solution and aqueous guava leaf extract.

Ag-TiO_2 photoanode for this study was obtained by immersing bare TiO_2photoanode in silver nanoparticle (Ag NP) colloid. The optimized device performance was analysed using data obtained from current–voltage (I-V) measurements. Various characterization techniques were adopted to elucidate the enhancement and quenching mechanisms taking place at the semiconductor-Ag-dye interfaces and its role in determining the overall efficiency of the solar cell.

4.2 Materials and Methods

4.2.1 Materials

TiO_2 nanoparticles (P25), Fluorine doped tin oxide (FTO-7Ω/Sqcm), hexachloroplatinic acid (H_2PtCl_6), potassium iodide (KI) (99.5%) and N719 dye were obtained from Sigma-Aldrich and iodine (I_2) from MERCK. Distilled water (Millipore System), ethanol and methanol (≥ 99% Sigma Aldrich) were used as solvents.

4.2.2 Synthesis of silver nanoparticles

Plant extract was prepared from leaves of *Psidium guajava* (Guava) that was first rinsed with tap water and then distilled water to remove all the dust and dirt settled on them. Then the leaves were air dried for the removal of water from the surface of the leaves. Leaf extract was prepared by boiling and stirring the leaves in distilled water following the same procedure as reported in our previous work [17]. 20mL of 1 mM $AgNO_3$ was used as precursor solution for nanoparticle synthesis. For synthesis of silver nanoparticles, 1mL of the extract was added to 20 mL of 1mM of $AgNO_3$ solution and stirred using

pipette to ensure uniform mixing. The colour change of the silver salt solutionto pale yellow and then yellowish brown implies the formation of silver nanoparticles. The change in colour is completed within four minutes showcasing a very fast reduction mechanism as depicted in Fig.4.1.

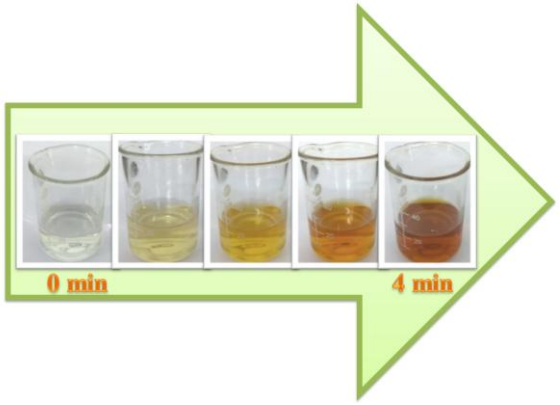

Fig.4.1 Colour change chart illustrating formation of Ag NPs

4.2.3 DSSC Assembly

FTO conductive glass plates (7 Ω/square cm) were first cleaned with soap solution and rinsed with de-ionised water and acetone for 10 minutes in an ultrasonic bath. The TiO_2 paste was prepared by blending commercial TiO_2 powder (anatase, 25 nm) with ethanol and one drop of TritonX -100.The resultant paste was deposited on the FTO glass plate using doctor blading technique. The air dried TiO_2 deposited FTO glass plates were calcined at 450^oC for 30 minutes in a muffle furnace. The thickness of the coated film was found to be 15 μm measured using a profilometer (Mitutoyo). On cooling, the area confinement of 0.25 cm^2 was done and dipped in silver nanoparticle colloid for 30 minutes. Finally dye was attached to TiO_2 surface by dipping the electrodes in dye solution for 24 hours. The photoelectrodes were taken from dye solution, rinsed with methanol to remove impurities and air dried for further use. The counter electrode was prepared by electrodepositing 4 mM

hexachloroplatinic acid (H_2PtCl_6) with a scan rate of 20mV/s for four cycles. The electrolyte was prepared by mixing 0.6M4-butyl methyl imidazolium iodide (BMII), 0.04 M Iodine (I_2), 0.1 M lithium iodide (LiI), 0.1 M guanidium thiocyanate (GuSCN) and 0.5 M tertiary butyl pyridine in acetonitrile. The TiO_2 electrode and electrodeposited Pt counter electrode were assembled to form a solar cell by sandwiching the redox electrolyte using binder clips.

4.2.4 Optical and Electrical measurements

The UV-vis spectrophotometer (T90, PGSTAT)was used to measure the nature of absorbance of the nanoparticles in the visible range of the solar spectrum. The size of the synthesized nanoparticles was determined by transmission electron microscopy (TEM) Jeol/ JEM 2100 using LaB6 source operated at 200 kV. The photoluminescence (PL) measurements were conducted using PerkinElmer (LS 55) in the visible range. For measuring the performance of DSSC, current-voltage (I-V) characteristics were done using solar simulator (Scientech) under 1 sun illumination (100mW/cm^2).The electrochemical impedance spectroscopic measurements were carried out using computer controlled electrochemical interface (SP150, Biologic) in the frequency range 1 mHz to 10MHz under illumination of 100mW/cm^2. Mott-Schottky measurements were conducted with 0.1 M Na_2SO_4 under the bias voltage of -0.9 V to -0.5 V in the frequency range of 1 kHz to 1Hz.The Flurocube-lifetime system (JOBIN-VYON) with pulsed diode excitation was used to measure lifetimes of the samples.

4.3 Results and Discussion

4.3.1 TEM and UV studies

TEM analysis of the Ag NPs indicates stable, well dispersed, near spherical nanoparticles as shown in Fig. 3(a).The TEM distribution graph Fig.3(b) shows maximum no of particles in the range 15-25 nm. The silver nanoparticles in this range are reported to show hot electron generation, a major mechanism involved in carrier generation enhancement in solar cells [18, 19].

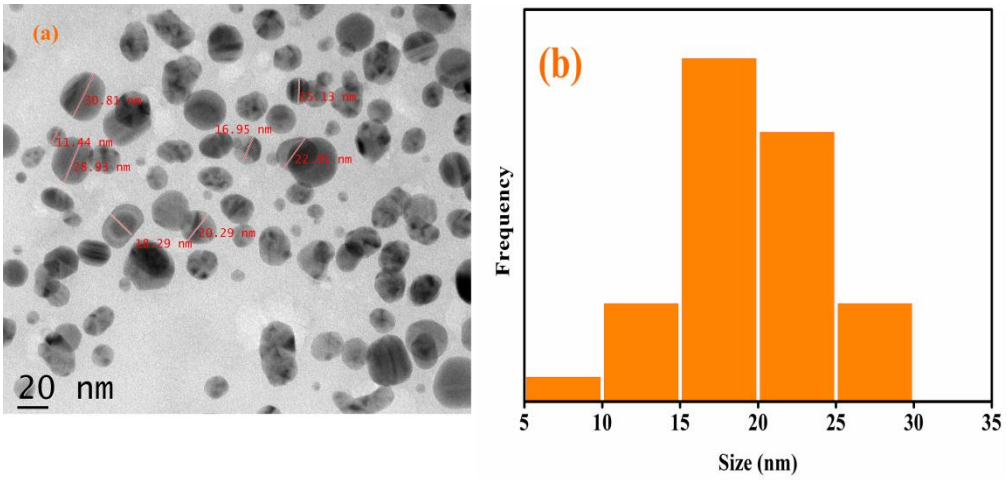

Fig.4.2 TEM (a) image (b) Size distribution graph of the synthesized Ag NPs

The UV- Vis measurement (Fig.4.3a) shows the absorbance peak at about 430 nm indicating the formation of silver nanoparticles. Guava leaf broth proves to be a good reducing agent in terms of synthesis rate with maximum conversion occurring in the first four minutes. Plasmonic nanostructures support the formation of resonant surface plasmons in response to a photon flux localising electromagnetic energy close to their surfaces. The electromagnetic field due to surface plasmon resonance enhances the optical absorption of the dye [20].

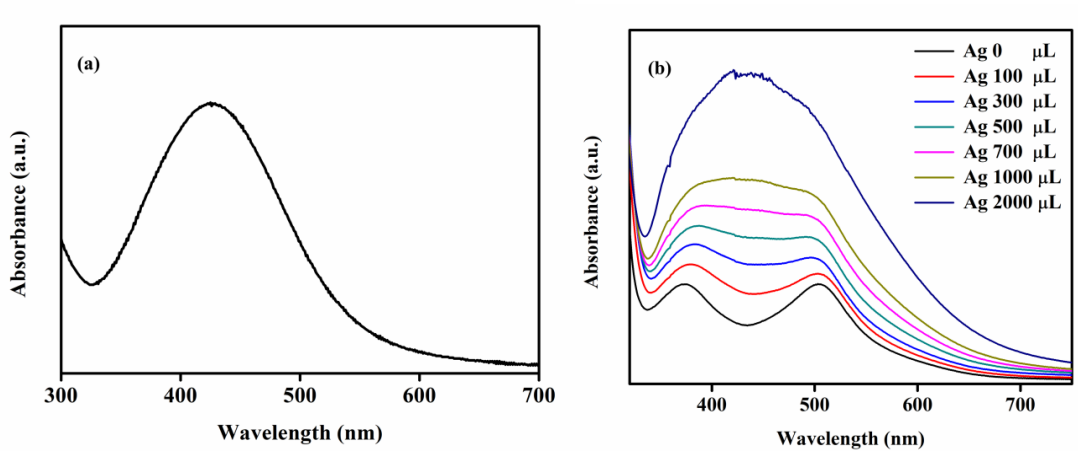

Fig.4.3 Absorbance spectrum of (a) Ag NP, (b) dye with increasing concentration of Ag NPs

The absorption enhancement of N719 dye on successive addition of silver nanoparticle solution in the range 300-600 nm has been depicted in Fig.4.3b. N719 has absorption peaks at 374nm and 504 nm which at first increase on addition of Ag NP and finally broadens leading to a panchromatic sensitization in the visible region. The increase in absorption coefficient of the dye due to LSPR of the Ag nanoparticles paves way for enhanced photogeneration of electrons leading to improved efficiency of solar cells.

4.3.2 SEM analysis and EDAX

The SEM image of Ag-TiO_2 thin film is shown in Fig.4.4a. The bright spots in the SEM image indicate the presence of silver nanoparticles distributed evenly on the TiO_2 surface [21]. The elemental analysis of silver modified TiO_2 photoanode was determined by conducting EDAX (Energy Dispersive X-Ray Analysis) analysis of the Ag-TiO_2 thin film. The analysis shows that 1.61 wt% Ag is present in the photoanode material as shown in the Fig.4.4b. The deposition of silver nanoparticles by dip coating method in this report matches

with the amount of direct deposition of silver on TiO_2 photoanode by other methods as reported previously [14].

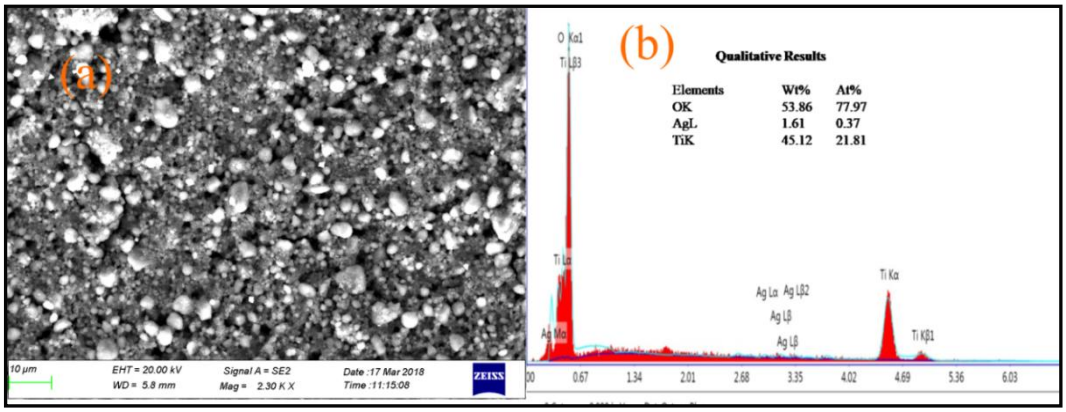

Fig.4.4 (a) SEM image of Ag-TiO_2 photoanode (b) EDAX of Ag-TiO_2-30 photoanode

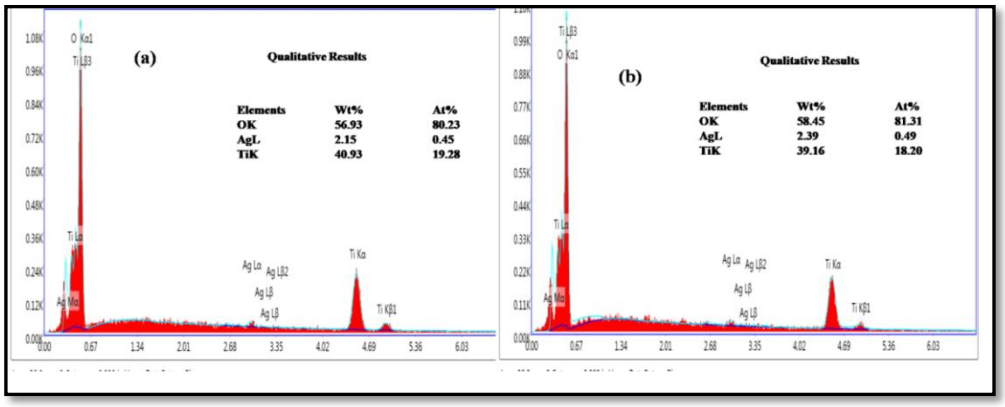

Fig.4.5 EDAX spectra (a) Ag-TiO_2-60 (b) Ag-TiO_2-120

From the increase in dipping time of photoanode in silver colloid the concentration of Ag in TiO_2 photoanode increases as shown in the EDAX spectra of Ag-TiO_2-60 and Ag-TiO_2-120 in the Fig. 4.5.

4.3.3 Bandgap and Mott-schottky analysis

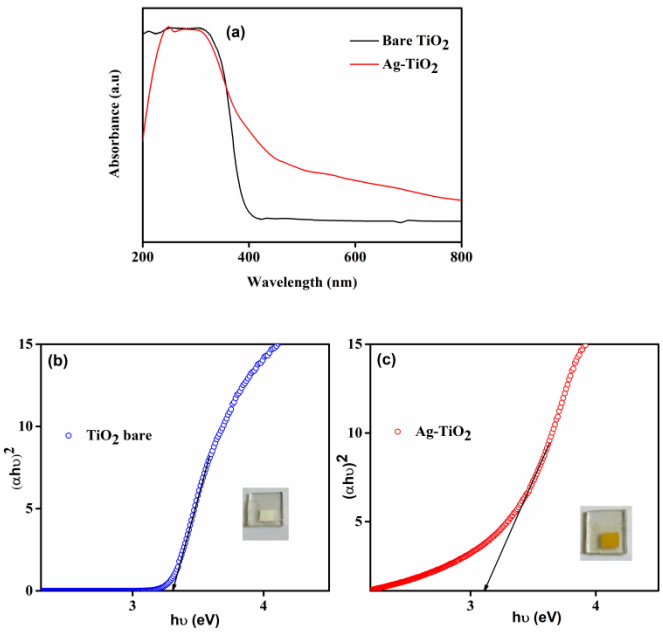

Fig. 4.6 (a) Absorbance of TiO_2 , Ag-TiO_2 .Tauc plot of (a) TiO_2 (b) Ag-TiO_2

The absorbance plot of the two photoanodes under study shows a considerable shift in the adsorption edge toward the visible region for the Ag-TiO_2 sample. The Tauc plots (Fig.4.6 b&c) drawn to calculate the bandgap energy of Ag-TiO_2 and bare TiO_2 shows E_g values as 3.3eV for bare TiO_2 and3.1 eV forAg-TiO_2 showing direct indication of decrease in bandgap energy due to the presence of metal nanoparticles in TiO_2.

The shifting of the absorbance towards the visible region acting favourably towards harnessing the solar spectrum leading to better light to energy conversion in solar cells [22, 23].

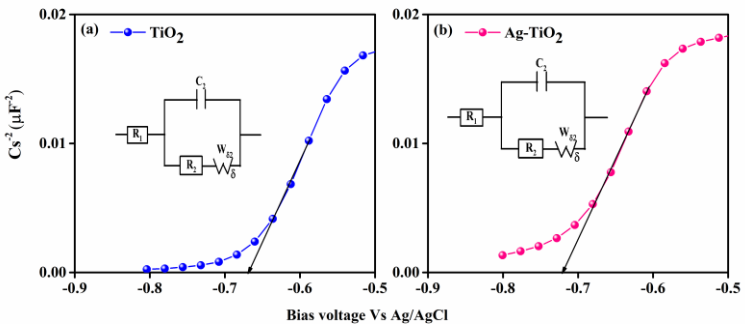

Fig.4.7 Mott-Schottky plot of (a) TiO_2 (b) Ag-TiO_2

The Mott-Schottky (MS) plot of the two photoanodes namely TiO_2 and Ag-TiO_2 has been displayed in Fig.4.7 (a) and (b).The positive slopes of both photoanodes establish the expected n-type semiconductor characteristics. The flatband potential (E_{fb}) is obtained by extrapolating capacitance ($1/Cs^2$) to zero.

$$\frac{1}{C^2} = \frac{2}{A^2 N_d e \in \in_0} (\mathrm{E} - E_{fb} - \frac{k_\beta}{e} T)$$

Where C is the capacitance, $\in$ is the dielectric constant of the material, $\in_0$ is the permittivity of free space, A is the area of the active surface, N_d is the donor or acceptor density, E is applied potential, E_{fb} is the flatband potential, k_β being the Boltzmann constant, T the temperature and e is the charge. The flatband potential of TiO_2 is -0.66V whereas it is -0.718V for Ag-TiO_2

The carrier concentration (N_d) was obtained by taking the slope of Mott-Schottky plot and dividing by area of the active surface of the electrode. The value for carrier concentration in bare TiO_2 is 2.128 x 10^{20} and that of Ag-TiO_2 is 3.2 x 10^{20} . The negative shift of flatband potential of Ag-TiO_2 with respect to TiO_2 along with increased carrier concentration leads to larger photocurrent generation in Ag-TiO_2 DSSC [24].

4.3.4 XPS studies

The surface composition of Ag-TiO_2 XPS spectra are depicted in the following graphs. The survey spectrum, O1s, Ti 2p and Ag 2p spectra are shown from Fig 4.8 (a) to 4.8 (d). The survey spectrum of 4.8 (a) shows peak at 284.2 eV corresponding to carbon from the instrument, Ag peaks at 366.38, 372.4 eV, Ti 2p peak at 457.4 eV and O 1s peak at 528.74 eV were seen in the figure. Fig 4.8 (b) shows O1s spectrum with two peaks due to TiO at 528.74 eV being the dominant peak and O-H peak at 530.227 eV being the minor peak. The Ti $2p_{3/2}$, Ti $2p_{1/2}$ peaks at 457.4 and 463.03 eV are evidence of Ti 4^+ formation in TiO_2 (Fig. 4.8c).

The Ag $3d_{5/2}$, $3d_{3/2}$ peaks appearing at binding energies 366.38eV and 372.4 eV (Fig. 4.8d) due to splitting of 3d doublet peak shows a difference of 6 eV which is indicative of the metallic nature of silver [25,26].

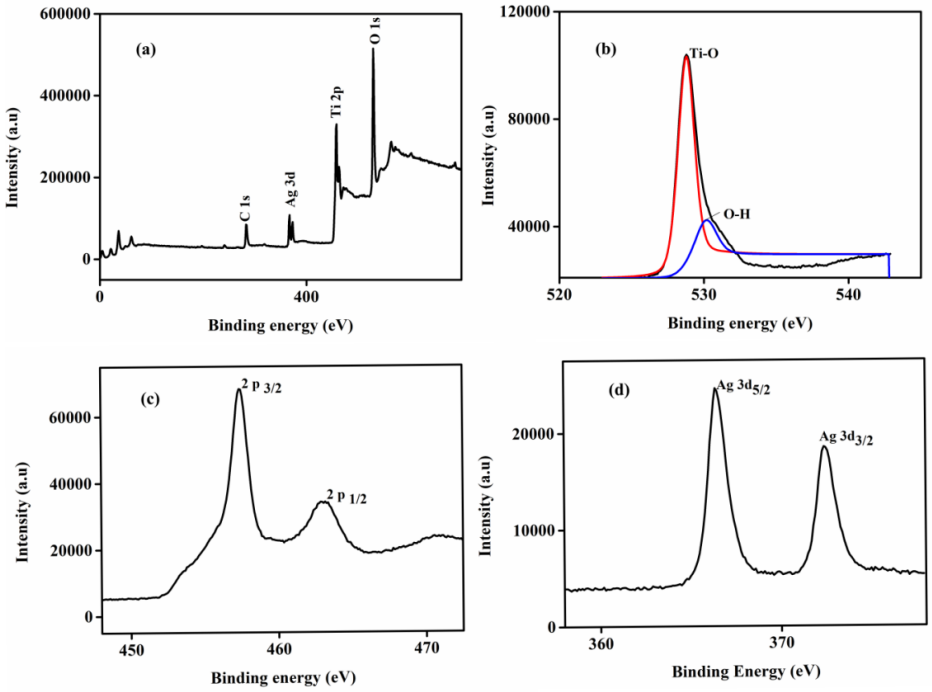

Fig 4.8 XPS (a) survey spectrum (b) O 1s (c) Ti 2p (d) Ag 3d

4.3.5 Solar Cell Characterisations of Ag-TiO_2

The current voltage characteristics of the cell with bare TiO_2 and Ag-TiO_2 with different dipping time, such as 30, 60 and 120 minutes, are given in Fig. 4.9a. Figure 4.9b depicts the Nyquist plot corresponding to the cell with bare TiO_2 and Ag-TiO_2 (30 minutes dipping time).

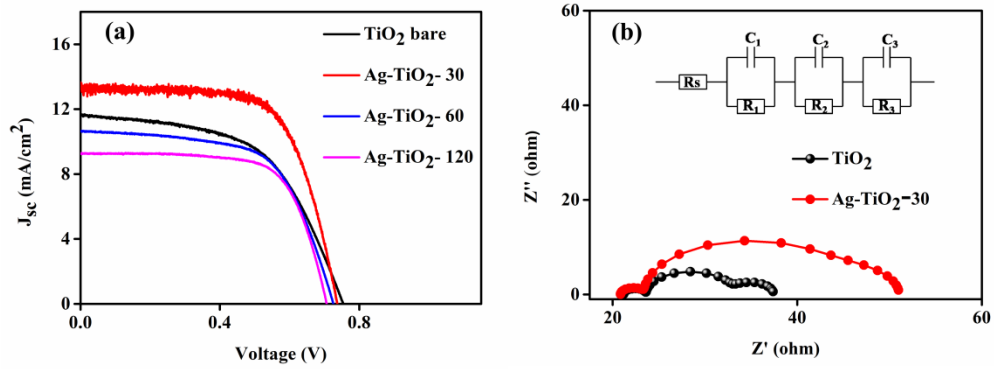

Fig.4.9 (a) Current voltage curves of bare TiO_2 and Ag-TiO_2 with different dip timings (b) Nyquist plot of bare and Ag-TiO_2-30 with inset showing the fitted equivalent circuit.

Sample	V_{oc} (V)	J_{sc} (mA/cm^2)	Fill Factor (FF) %	Efficiency η %
TiO_2	0.752	11.69	55.4	4.85
Ag-TiO_2-30	0.737	13.33	66.6	6.69
Ag-TiO_2-60	0.726	10.64	62.0	4.79
Ag-TiO_2-120	0.707	9.25	69.3	4.53

Table 4.1 Solar cell parameters from J-V curve of different Ag-TiO_2 photoanodes

The various device parameters like short circuit current density (J_{sc}),open circuit voltage (V_{oc}), fill factor (FF) and efficiency (η) of Ag-TiO_2 photoanode and bare TiO_2 studied for device performance are presented in Table.1. In the case of Ag-TiO_2 photoanode the open circuit voltage (V_{oc}) decreases slightly as compared to bare TiO_2. The V_{oc} is proportional to the difference between Fermi level of TiO_2 and Nernst potential of iodine/iodide electrolyte in a solar cell. The gap between the newly formed Fermi level of Ag-TiO_2 and redox potential of electrolyte is smaller by the shifting of the conduction band due to the adsorption of silver nanoaprticles. This finding is consistent with the previous reports of decrease in V_{oc} due to incorporation of noble metals in TiO_2 [27-29].The photocurrent density increases from 11.69 in bare TiO_2 to 13.33 mA/cm^2in Ag-TiO_2-30 photoanode. The increase in optical absorption by dye due to LSPR of silver nanoparticle, reduced electron hole recombination losses and narrowing of the bandgap seem to be the primary reasons for the boosted current density observed in Ag-TiO_2photoanode solar cell. Further the presence of large number of hydroxyl groups in the leaf extract of guava corresponding to gallic acid, querectin[30] present as capping agent for Ag NP contribute to its better attachment with the dye thus positively affecting the efficiency of the solar cell [31].The Nyquist plot (Fig. 4.9b) for Ag-TiO_2 -30 and bare TiO_2 photoanode fitted with the equivalent circuit exhibits semicircles corresponds to vital processes occurring at counter electrode, photoanode and electrolyte interfaces in DSSC. The first semicircle (R_1) in high frequency region symbolises charge transfer resistance at the counter electrode-electrolyte interface and the next semicircle (R_2) in the intermediate frequency region is associated with the dye sensitized photoanode/electrolyte interface resistance

and third semicircle (R_3) corresponds to Warburg resistance related to the diffusion of the electrolyte [32]. The values of EIS parameters R_1, R_2 and R_3 have been listed in Table 2. From the values we observe that there is no significant change in R_1 and R_3 values as Ag NPs have practically a lesser role in charge transfer kinetics at counter electrode and diffusion of the redox electrolyte [15]. However plasmonic effect is directly involved in the photoanode-dye/electrolyte interface, hence the value of R_2 is different for TiO_2 and Ag-TiO_2 -30. The increased electron transfer due to LSPR and reduced electron-hole recombination at the Ag-TiO_2-dye-electrolyte interface accounts for the high value of R_2 (23.88 Ω) as compared to R_2 (8.88 Ω) of bare TiO_2.

Sample	R_1 (ohm)	R_2 (ohm)	R_3 (ohm)
TiO_2	2.90	8.88	4.81
Ag-TiO_2-30	2.57	23.88	4.20

Table 4.2 Electrochemical impedance (EIS) parameters of bare TiO_2 and Ag-TiO_2 -30

The stability studies of Ag-TiO_2 -30 photoanode show decrease in efficiency over a period of 100 hours, but V_{oc} remains almost unchanged indicating the stability of the photoanode (Fig. 4.10).The decrease in efficiency of the device with time could be due to corrosive effect of the electrolyte on dye and counter electrode leading to lesser photocurrent [33].

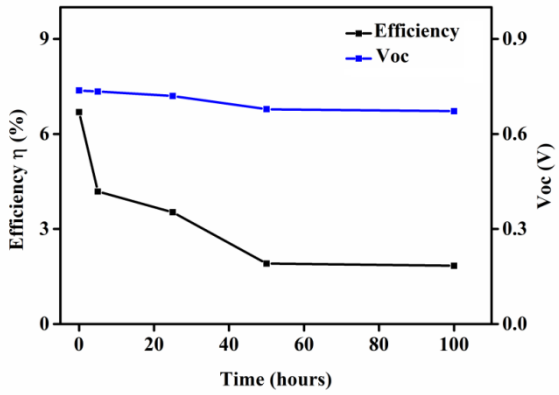

Fig.4.10. Stability studies of Ag-TiO_2 -30 photoanode cell

However, decrease in efficiency with increase in dipping time can be attributed to the presence of excess Ag on the TiO_2 surface which may be oxidised and corroded by the electrolyte (Figure 4.9a). The excess of Ag in the TiO_2 film is quantified using EDAX spectra obtained for Ag-TiO_2 -60 and Ag-TiO_2 -120 as shown in Fig. 4.5.

The excess of Ag NP on the surface reduces the sensitization of the TiO_2 by the N719 dye thus affecting the TiO_2-dye interface, a vital parameter in light harvesting and charge transfer in DSSC. An alternate possible mechanism responsible for the decrease in efficiency is associated with radiationless energy transfer between TiO_2 and Ag nanoparticles, which has been explained in this investigation. The Ag nanoparticles act as acceptor extracting energetic charge carriers from the semiconductor donor (TiO_2), thus reducing the number of carriers for charge transport in a solar device. Inspite of their various light enhancement properties, metal nanoparticles act as quenchers in certain hybrid systems which hamper the charge transport, thus adversely affecting the efficiency.

4.3.6 FRET Calculations and Lifetime measurements

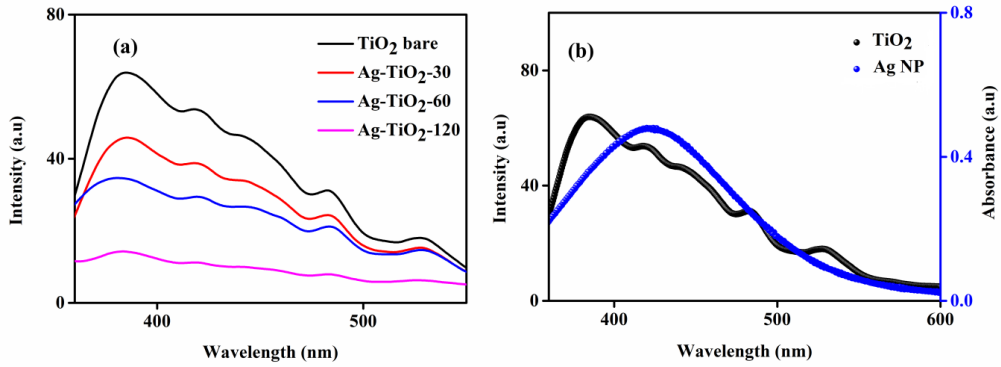

Fig.4.11 (a) PL quenching with various dipping times (b) TiO_2 and Ag NP overlap curve

PL studies are an indispensable tool in determining the charge transfer/recombination dynamics which are crucial in controlling the photoelectrical properties and hence performance of solar devices. The fate of the charge carriers (electron-hole pairs) can be studied to a large extent as PL emissions arise from recombination of free carriers. The PL emissions (Fig. 4.11a) show that the Ag-TiO_2 has diminished PL intensity compared to bare TiO_2. The PL emission of Ag-TiO_2 decreases with increase in dipping time from 30 to 120 minutes. The higher PL intensity of bare TiO_2 shows the rapid recombination of photogenerated charge carriers whereas a low PL emission indicates lesser electron-hole recombination favourable for improved charge transport [34].This lowering of PL intensity in Ag-TiO_2 can be attributed to the formation of Schottky barrier at Ag and TiO_2 interface retarding electron hole recombination processes and thereby promoting better transport of electrons. In this investigation we unravel another possibility of reduced

PL intensity due to the non-radiative energy transfer from TiO_2 to plasmonic metals (silver in this case) due to FRET (Förster Resonance Energy Transfer) mechanism. FRET involves depletion of the excited state of the semiconductor due to the presence of metal in the vicinity leading to PL quenching [35].The resonance energy transfer from TiO_2 to Ag NP is further justified by the overlap of emission spectrum of $TiO_2$with the Ag NP absorption spectrum(Fig. 4.11b). The Förster radius R_0, that is the distance at which probability of energy transfer is 50% is calculated using the standard equation [36].

$$R_0 = 0.211\ [k^2 n^{-4} Q_D J]^{1/6} \text{ ---------- (1)}$$

Where k^2 is the relative orientation of the dipoles of donor and acceptor in space and taken to be 2/3, n is the refractive index of the medium taken to be 1.4,Q_D the quantum yield of commercial TiO_2 anatase is 0.14 [37] , J is the overlap integral between TiO_2 emission and Ag NP absorption. From the calculation using equation (1), R_0 is found to be 3.88 nm which is in the acceptable range of FRET mechanism of 1-10 nm [38].Further evidence for FRET is provided by the lifetime measurements as shown in Fig. 4.12 to ratify the energy transfer from semiconducting nanoparticles (TiO_2) to Ag NP. Time correlated single photon counting (TCSPC) study was performed using a pulsed excitation of 370 nm. The time resolved fluorescence decay curves of bare TiO_2 and Ag-TiO_2 with various dipping times were measured. The red dots correspond to the decay and black dots

correspond to the instrument response curve. The decay profiles were fitted with a two- exponential function as reported elsewhere [39].

$$I(t) = \alpha_1 \exp(-t/\tau_1) + \alpha_2 \exp(-t/\tau_2) \text{---------- (2)}$$

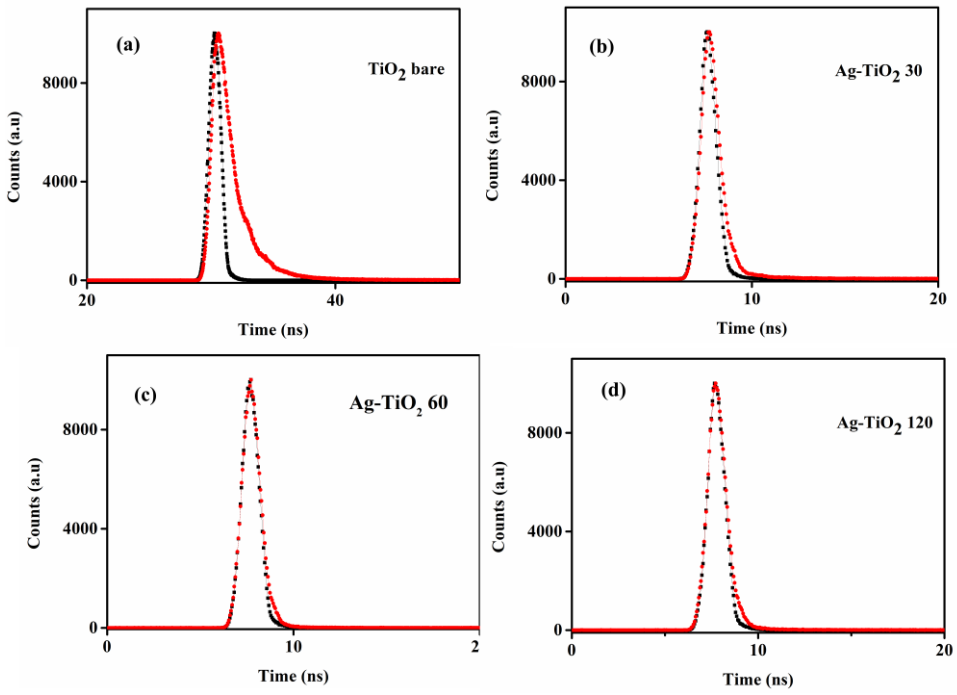

Fig.4.12 Lifetime decay curves of (a) TiO_2 bare (b) Ag-TiO_2-30 (c) Ag-TiO_2-60 (d)Ag-TiO_2-120

The obtained decay times have been presented in Table. 4.3. The shortening of lifetime of the TiO_2 (in the presence of Ag NP) is a clear indication of FRET occurring between the donor –acceptor pair. The obtained decay times have been presented in Table. 4.3. The shortening of lifetime of the TiO_2 (in the presence of Ag NP) is a clear indication of FRET occurring between the donor –acceptor pair.

Sample	τ_{avg} (ns)	FRET efficiency (%)
Bare TiO_2	0.227	-
Ag- TiO_2-30	0.119	47.6
Ag- TiO_2-60	0.071	68.8
Ag- TiO_2-120	0.065	71.2

Table 4.3 Lifetime and FRET efficiency calculated from TCSPC measurements

The FRET efficiency [38] is calculated from the relative fluorescence lifetime of the donor (TiO_2) in the absence (τ_D) and presence (τ_{DA}) of the acceptor (Ag NPs) using the formula

$$E = 1 - \frac{\tau_{DA}}{\tau_D}$$

where E is the efficiency of energy transfer.

The energy transfer efficiency increases with increase in dipping time of photoanode in Ag NP colloid which leads to increase in silver content in the photoanode as shown in EDAX of Ag-60 and Ag-120(Fig .4.5).This increase of acceptor concentration is responsible for the rise of transfer efficiency from 47.6 to 71.2% abiding by the basic characteristics of a FRET mechanism [40].The working of DSSC with a modified electrode along with charge and energy transfer mechanism has been presented in Fig4.13.

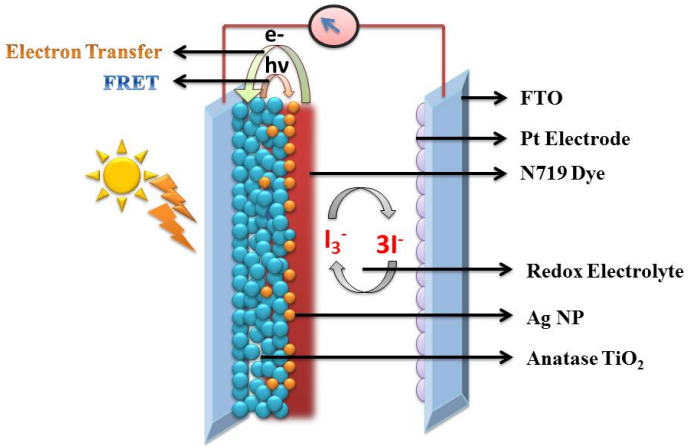

Fig 4.13 -Schematic illustration of working of Ag-TiO_2 photoanode DSSC

FRET is generally perceived as a loss mechanism in TiO_2-Ag hybrid structures [41-43]. Similarly quenching of fluorescent intensity of molecular probes in metal- fluroprobe hybrid systems via energy and electron transfer, being the major pathways, has been reported by Rahman *et al* [44]. In this work we have investigated the solar cell performance with respect to LSPR effect of Ag NPs in Ag-dye interface and energy transfer at TiO_2-Ag interface and observed their effect on solar cell performance. At an optimum dipping time LSPR effect dominates the scenario by generating enough electron hole pairs for strengthened solar to electricity conversion as seen in Ag-TiO_2-30.However, as dipping time increases the amount of silver nanoparticles in the photoanode increases leading to more TiO_2-Ag NP interaction with energy transfer becoming dominant process over LSPR thereby reducing the efficiency of the cell.

4.4 Conclusion

Silver nanoparticles were synthesized using leaf extract of guava through a simple, green protocol. The nanosilver was incorporated into the TiO_2 with dip coating method for 30, 60 and 120 minutes and was used as photoanode in dye sensitized solar cell and its performance studied and analysed. The optimised performance was attained by 30 minute dipping of the TiO_2 photoanode and the Ag-TiO_2-30 photoanode effectively improves the solar cell performance from 4.85 % to 6.69%. The improvement is due to the enhanced current density J_{sc}, from 11.69 to 13.33 mA/cm^2. The silver nanoparticles act as performance boosters by enhancing dye absorption in the visible region due to LSPR effect and suppress the back recombination at TiO_2-electrolyte interface. This remarkable light harvesting by Ag-TiO_2 photoanode is credited to reduction in band gap, surface plasmon effect of silver nanoparticles and reduction in losses due to electron hole recombination, thereby emphasising its prospective role in low cost solar devices.TiO_2-Ag interfaces increase with increasing the dipping time of the photoanode in silver nanoparticle colloid and that promote resonant energy transfer thereby suppressing the efficiency of the solar cell. The interplay of electron and energy transfer with increased dipping time of silver nanoparticles has been explained using FRET parameters and lifetime measurements. The charge and energy transfer phenomena at the semiconductor-AgNP-dye interfaces lead to different solar light harvesting in the various hybrid structures. This complementary role of charge and energy transfer can be suitably optimised to get plasmonic solar cells with superior efficiencies.

References

[1] P. V. Kamat, Meeting the clean energy demand: Nanostructure architectures for solar energy conversion, J. Phys. Chem. C 111 (2007)2834-2860.

[2] Michael Grätzel, Conversion of sunlight to electric power by nanocrystalline dye-sensitized solar cells, J. Photochem. Photobiol A 164 (2004) 3–14.

[3] B. E. Hardin , H. J. Snaith, M. D. McGehee, The renaissance of dye-sensitized solar cells, Nature Photonics 6 (2012) 162-169.

[4] S. Ito, T. N. Murakami, P. Comte, P.Liska, C. Grätzel, M. K. Nazeeruddin , M. Grätzel , Fabrication of thin film dye sensitized solar cells with solar to electric power conversion efficiency over 10%, Thin Solid Films 516 (2008) 4613–4619.

[5] S. Meng, E. Kaxiras, Electron and Hole Dynamics in Dye-Sensitized Solar Cells: Influencing Factors and Systematic Trends, Nano Lett. 10 (2010) 1238–1247.

[6] G. Calogero, P. Calandra, A. Irrera, A. Sinopoli, I. Citro , G. Di Marco, A new type of transparent and low cost counter-electrode based on platinum nanoparticles for dye-sensitized solar cells, Energy Environ. Sci 4 (2011) 1838-1844.

[7] X. Dang, J. Qi, M. T. Klug, Po-Y. Chen, D. S. Yun, N. X. Fang, P.T.Hammond, A. M. Belcher, Tunable localized surface Plasmon enabled broadband light harvesting enhancement for high-efficiency panchromatic dye-sensitized solar cells,Nano. Lett. 13 (2013) 637-642.

[8] J. R. Cole, N. J. Halas, Optimized plasmonic nanoparticle distributions for solar spectrum harvesting, Applied Physics Letters 89 (2006)153120-153123.

[9] H. A. Atwater, A. Polman, Plasmonics for improved photovoltaics devices, Nature Materials 9 (2010) 205-212.

[10] N. C. Jeong, C. Prasittichai, J. T. Hupp, Photocurrent enhancement by surface Plasmon resonance of silver nanoparticles in highly porous dye sensitized solar cells, Langmuir 27 (2011) 14609-14614.

[11] M. Ihara, K. Tanaka, K. Sakaki, I. Honma, K. Yamada, Enhancement of the absorption coefficient of ruthenium(II) dye in dye sensitized solar cells by a silver island film, J. Phys. Chem B 101 (1997) 5153-5157.

[12] S. Buda, S. Shafie, S. A. Rashid, H. Jaefer, N.F.M Sharif, Enhanced visible light absorption and reduced charge recombination in AgNPplasmonicphotoelectrochemical cell, Results in Physics 7(2017) 2311-2316.

[13] K.Guo, M. Li, X. Fang, X. Liu, B. Sebu, Y. Zhu, Z. Hu, X. Zhao, Preparation and enhanced properties of dye sensitized solar cells by surface plasmon resonance of Ag nanoparticles in nanocompositephotoanode, Journal of Power Sources 230 (2013) 155-160.

[14] S. Sardar, S. Ghosh, H. Remita, P. Kar, B. Liu, C. Bhattacharya, P. Lemmens, S. K. Pal, Enhanced photovoltage in DSSC; synergistic combination of a silver modified TiO_2photoanode and a low cost counter electrode, RSC Adv 6 (2016) 33433-33442.

[15] P. Nibelayim, G. Kawamura, W. K. Tan, H. Muto, A. Matsuda, Systematic characterisations of the effect of Ag@TiO_2 nanoparticles on the performance of plasmonic dye-sensitized solar cells,Sci. Rep 7 (2017) 1-12.

[16] U.K. Parashar, V. Kumar, T. Bera, P.S. Saxena, G. Nath, S.K. Srivastava, R. Giri, A. Srivastava, Study of mechanism of enhanced antibacterial activity by green synthesis of silver nanoparticles, Nanotechnology 22 (2011) 1-13.

[17] R. Rajita, P. Nijisha, C.V. Nivedita, S. Sindhu, Natural dyes from red amaranth leaves as light harvesting pigments for dye sensitized solar cells, Mater Res. Bull 90 (2017) 156-161.

[18] W. E. Erwin, H. F. Zarick, E. M. Talbert, R. Bardhan, Light trapping in mesoporous solar cells with plasmonic nanostructures, Energy Environ. Sci. 9 (2016) 1577-1601.

[19] W. Fan, M. K. H. Leung, Recent Development of plasmonic resonance-based photocatalysis and photovoltaics for solar utilization, Molecules 21 (2016) 1-26.

[20] J. Li, X. Chen, N. Ai, J. Hao, Q. Chen, S. Strawf, Y. Shi, Silver nanoparticle doped TiO_2nanofiber dye sensitized solar cells, Chemical Physics Letters 514(2011) 141-145.

[21] T. Solaiyammal, S. Muniyappan, B. G.T. Keerthana, S. S. Nemala, P. Bhargava,· P. Murugakoothan, Green synthesis of Ag and the effect of Ag on the efficiency of TiO_2 based dye sensitized solar cell, J Mater Sci: Mater Electron 28 (2017) 15423–15434.

[22] Y. H. Jang, Y. J. Jang, S. T. Kochuveedu, M. Byun, Z. Lin, D. H. Kim, Plasmonic dye-sensitized solar cells incorporated with Au-TiO_2 nanostructures with tailored configurations, Nanoscale 6 (2014) 1823-1832.

[23] S. P. Lim, A. Pandikumar, H. N. Lim, R. Ramraj, N. M. Huang, Boosting photovoltaic performance of dye sensitized solar cells using silver nanoparticle decorated N,S-Co-doped-TiO_2photoanode, Sci. Rep,11922 (2015) 1-14.

[24] N. Yao, J. Huang1, K. Fu, X. Deng, M. Ding, S. Zhang, X. Xu1 , L. Li, Reduced interfacial recombination in dye-sensitized solar cells assisted with NiO:Eu3+,Tb3+ coated TiO_2 film, Sci. Rep. 6 (2016) 1-9.

[25] J. Yu, J. Xiong, B. Cheng, S. Liu, Fabrication and characterization of Ag–TiO_2 multiphase nanocomposite thin films with enhanced photocatalytic activity,Applied Catalysis B: Environmental 60 (2005) 211–221.

[26] L. Ma, Y. Huang, M. Hou, Z. Xie , Z. Zhang, Ag nanorods coated with ultrathin TiO_2 shells as stable and recycleable SERS substrates, Sci. Rep. 5 **(**2015)1-8.

[27] K. G. Deepa, P. Lekha, S. Sindhu, Efficiency enhancement in DSSC using metal nanoparticles: A size dependent study, Solar Energy 86 (2012) 326-330.

[28] J. Du, J. Qi, D. Wang, Z. Tang, Facile synthesis of Au@TiO_2 core-shell hollow spheres for dye-sensitized solar cells with remarkably improved efficiency, Energy. Environ. Sci. 2012 5 (2012) 6914-6918.

[29] M. A. K. L Dissannayake, J. M. K. W Kumari, G. K. R Senadera, C. A. Thotowatthage, Efficiency enhancement in plasmonic dye-sensitized solar cells with TiO_2photoanodes incorporating gold and silver nanoparticles, J. Appl. Electrochem 46 (2016) 47-58.

[30] E. Diaz-de-Cero, V. Verardo, A.M.G. Caravaca, A.F. Gutierrez, A.G. Carretero, Determination of polar compounds in guava leaves infusions and ultrasound aqueous extract by HPLC-ESI-MS, J. Chem. 2015 (2015) 1-9.

[31] Z.Tian, L. Wang, L.Jia, Q. Li, Q. Song, S. Su and H. Yang, A novel biomass coated Ag–TiO_2 composite as a photoanode for enhanced photocurrent in dyesensitized solar cells, RSC Advances 3 (2013) 6369-6376.

[32] Q. Wang, J –E. Moser, , M.Grätzel, Electrochemical Impedance Spectroscopic Analysis of Dye-Sensitized Solar Cells, J. Phys. Chem. B 109 (2005) 14945-14953.

[33] G. Boschloo, A. Hagfeldt, Characteristics of the iodine/triodide redox mediator in dye-sensitized solar cells, Accounts of chemical research 42 (2009) 1819-1826.

[34] S. P. Lim, A. Pandikumar, N. M. Huang, H. N Lim, G. Gu, T. L. Ma, Promotional effect of silver nanoparticles on the performance of N-doped TiO_2photoanode based dye sensitized solar cells, RSC. Adv. 4 (2014) 48236-48244.

[35] J.Chen, S. Shen,P.Guo, M. Wang, J. Su, D. Zhao, L.Guob, Plasmonic Ag@SiO2 core/shell structure modified g-C3N4 with enhanced visible light photocatalytic activity, J. Mater. Res. 29 (2014) 64-70.

[36] S. Sardar, P. Kar, H. Remita, B. Liu, P. Lemmens, S. K. Pal, S. Ghosh, Enhanced charge separation and FRET at heterojunctions between semiconducting nanoparticles and conducting polymer nanofibers for efficient solar light harvesting, Sci. Rep 5 (2015) 1-14.

[37] M. Lunz and A. L. Bradley, Concentration dependence of Förster resonant energy transfer between donor and acceptor nanocrystal quantum dot layers: Effect of donor-donor interactions, Phy. Rev. B 83 (2011) 1-10.

[38] Suparna Sadhu, Krishna KantaHaldar, and AmitavaPatra, Size Dependent Resonance Energy Transfer between Semiconductor Quantum Dots and Dye Using FRET and Kinetic Model, J. Phys. Chem. C 114 (2010) 3891–3897.

[39] N. Serpone, A. Salinaro, Terminology, relative photonic efficiencies and quantum yields in heterogeneous photocatalysis. Part I: Suggested protocol, Pure & Appl. Chem. 71 (1999) 303-320.

[40] L. Dworak, V. V. Matylitsky, T. Ren, T. Bashe, T. Wachtveit, Acceptor concentration dependence of förster resonance energy transfer dynamics in dye-quantum dot complexes, J. Phys. Chem. C 118 (2014) 4396-4402.

[41] J. Zhou, F. Ren, S. Zhang, W. Wu, X. Xa, Y. Liu, C. Jiang, SiO_2 –Ag-SiO_2-TiO_2 multi-shell structures: Plasmon enhanced photocatalysis with wide spectral response, J. Mater. Chem. A 1 (2013) 13128-13138.

[42] D. B. Ingram, S. Linic, Water splitting on composite plasmon –metal/semiconductor photoelectrodes: Evidence for selective Plasmon

induced formation of charge carriers near the semiconductor surface, J.Am.Chem.Soc.133 (2011) 5202-5205.

[43] E. Liu, L. Kang, Y. Yang, T. Sun, X. Hu, C. Zhu, H. Liu, Q. Wang, X. Li, J. Fan, Plasmonic Ag deposited TiO_2nano-sheet film for enhanced photo-catalytic hydrogen production by water splitting, Nanotechnology 25 (2014) 1-10.

[44] Dewan S. Rahman, Sanhita Deb, Sujit Kumar Ghosh, Relativity of electron and energy transfer contributions in nanoparticle-induced fluorescence quenching,J. Phys. Chem. C119 (2015) 27145−27155.

CHAPTER 5

DYE-Au HYBRID FRET STRUCTURES IN PHOTOCATALYSIS

DYE-Au HYBRID FRET STRUCTURES IN PHOTOCATALYSIS

5.1. Introduction:

The effective utilisation of natural resources particularly sunlight for energy harvesting applications is an active area of research for the past few decades. Photovoltaics and photocatalysis are two important renewable energy technologies utilize sunlight for energy harvesting applications. Though both depend on the electron –hole generation, the electron –hole pairs are driven in a circuit to get current in photovotaics whereas they participate in a redox reaction in photocatalysis[1]. The nanostructured materials due to their size dependent properties are the backbone of new generation light harvesting systems. These nanomaterials both inorganic and organic have been utilised for the design of energy conversion systems. Though semiconductor nanomaterials are being extensively used for photocatalysis, noble metals have shown great development in the last decade [2] .

Noble metal nanostructures characterised by the generation of surface plasmon in resonance with incoming light show very strong absorption in the visible region. Hence the key factor governing any light harvesting technology is to incorporate metal nanostructures to enhance optical absorption, carrier generation and electromagnetic field enhancement to obtain the maximum flux of incident photons. By tuning the geometry, dimension, and composition, the metal nanostructures can suitably be manipulated to capture varying wavelengths of solar light to complement the absorption by the sensitizer in the case of solar cell and semiconductor in the case of photcatalysis [3].

The metallic nanostructures due to these properties significantly affect the photophysical properties of molecular chromophores leading to interesting biological and sensor applications[4]. These interactions are responsible for the de-excitation of the dye involving electron and energy transfer to the bound metal nanoparticle[5]. One of the pathways is non-radiative energy transfer (FRET) from the dye to the acceptor nanoparticle.Methylene Blue- Au nanoparticles (MB-Au NP), Methylene Blue- Quantum dots (MB-QD)systems have been previously reported for photodynamic therapy and bio-imaging purposes respectively[6,7]. In this work FRET between Methylene Blue (MB) and gold nanoparticles has been explored to study the photodegradation of Methylene blue (MB) dye.

5.2. Experimental Section

5.2.1 Synthesis

The fresh mature leaves of guava were collected, washed and dried in air for some time. The leaves were then cut into small pieces and boiled and stirred with distilled water (Millipore system) for 15 minutes in a magnetic stirrer at 100°C and 500 rpm. The extract was cooled and filtered using Whatman filter paper and stored at 4^{o}C for analysis.1mM of $HAuCl_4$ (Sigma-Aldrich) was used as gold precursor solution for synthesis of nanoparticles.

For synthesis of gold nanoparticles 1 mL (Au1), 2mL (Au2) and 3 mL (Au3) of extract were added to 3 ml of 1mM of $HAuCl_4$ solution and stirred for two minutes at room temperature to ensure uniform mixing. The instant colour change of the pale yellow gold salt solution implies the formation of gold

nanoparticles. The sample Au1 shows reddish pink colour whereas samples Au2 and Au3 show black colour indicating variation from Au1 (Fig. 5.1).

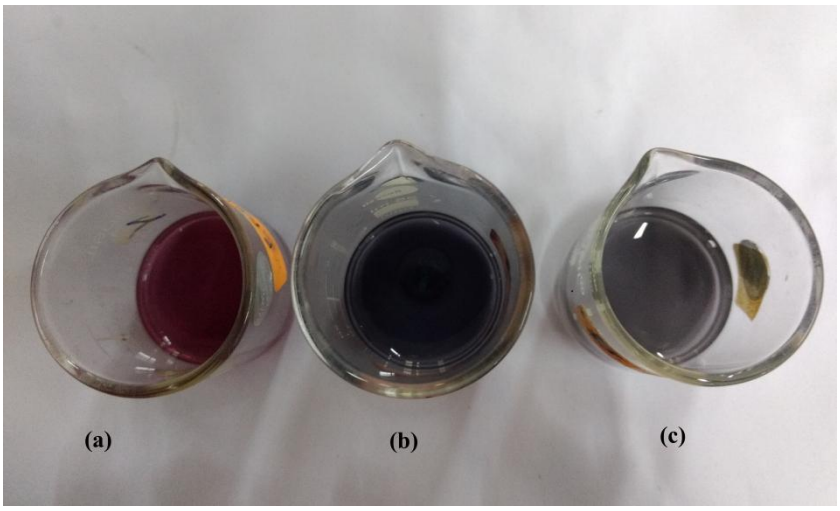

Fig. 5.1 Gold nanoparticle solutions of different colours (a) Au1 (b) Au2 (c) Au3

5.2.2 Dye Degradation

Photocatalytic activity measurements were conducted by adding 1 mL of gold nanoparticle solution to 20 mL of MB dye (0.002 wt %) in distilled water. The resulting mixture was subjected to stirring for 10 minutes under dark condition to attain absorption-desorption equibilirium. Initially 4 mL of the dye solution was taken and the MB concentration monitored using a UV-Vis Spectrophotometer. Further the dye solution absorbance was observed after 30 and 60 minutes intervals under illumination by 300 W Xenon lamp in presence of metal nanoparticles.

5.2.3 Characterisation Techniques

The UV-Vis spectrophotometer was used to measure the nature of absorbance of the nanoparticles due to surface plasmon resonance (SPR) in the visible range of the solar spectrum. The size of the synthesized nanoparticles was determined by transmission electron microscopy (TEM) Jeol/ JEM 2100 using LaB6 source operated at 200 kV. The fluorescent measurements were conducted using PerkinElmer (LS55) in the visible range. The photocatalytic measurements were conducted using photocatalytic reactor (LZCX-XE) using 300W Xenon Lamp. Lifetime measurements were conducted with Flurocube-lifetime system (JOBIN-VYON) with pulsed diode excitation

5.3. Results and Discussion

5.3.1 Optical Measurements

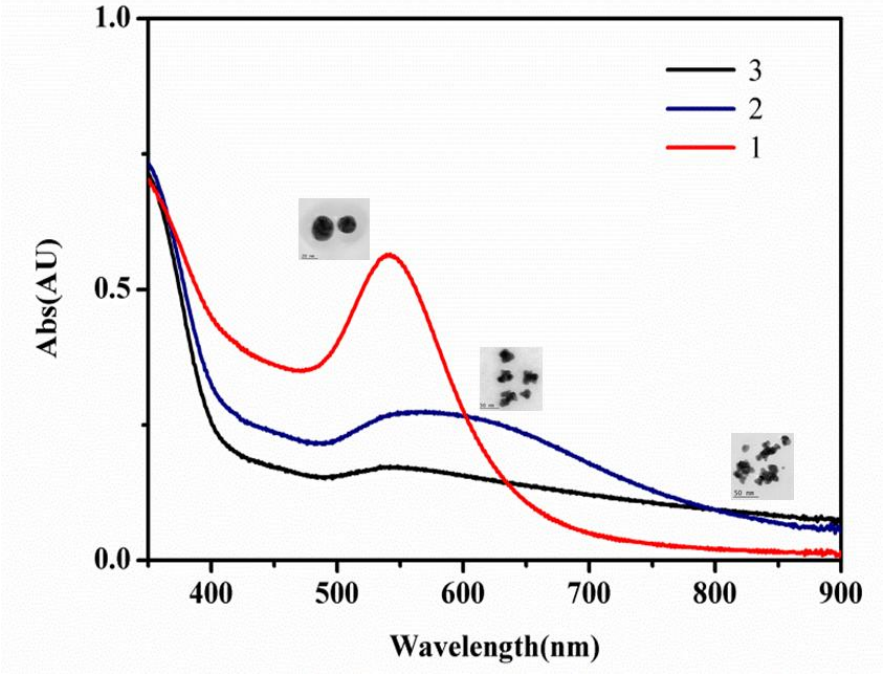

Fig.5.2 TEM images of Au1, Au2 and Au3 with their normalised absorption spectra

UV absorption spectra of the nanoparticles, Au1 Au2 and Au3,along with corresponding TEM images are presented in Fig.5.2.It is seen that the aggregate structures Au2 and Au3 show broadband spectra compared to the sharp peak shown by monodisperseAu1 nanoparticles.

The concentration of nanoparticles in solution is obtained using a method reported by Liu et al[8]. The average number of gold atoms per nanoparticle is calculated using the equation

$$N = 0.523\frac{\rho D^3}{M.} \quad \text{..... (1)}$$

Where ρ and M correspond to the density of fcc gold and atomic mass respectively. D is the average size of the nanoparticle obtained from TEM measurements and the details are presented in Table 1. The molar concentration of the nanoparticle solution is given by

$$C = \frac{N_{tot}}{N\,V\,N_a} \quad \text{..... (2)}$$

WhereN_{tot},N_a correspond to the total number of gold salt present in the solution and Avogadro number respectively. V is the volume of the reaction solution. The concentration of the samples Au1, Au2 and Au3 have been shown in Table 5.1.

Name	Concentration in mol/L	Average Size from TEM Images (nm)
Au 1	4.47×10^{-7}	26.2
Au 2	1.12×10^{-7}	38.6
Au 3	3.80×10^{-8}	52.7

Table 5.1 Sizes and concentrations of Au nanoparticles

The gold nanoparticles Au1, Au2 and Au3 are used for the fluorescent quenching studies of methylene blue dye with an excitation wavelength of 580 nm as shown in Fig 5.3a to c. From the graphs it is seen that Au3 quenches the MB dye fluorescence better than Au1 and Au2. The relative intensity I_0/I as a function of Au concentration has been plotted in Fig. 5.3d. Here I_0 and I are the intensity of the dye in the absence and presence of quencher respectively. It is seen that relative intensity increase with concentration of the quencher (gold nanoparticles) and is a measure of the quenching efficiency of the individual nanoparticles Au1, Au2 and Au3. The graph shows that the extent of quenching is highest for Au3 followed by Au2 and Au1. As the metal nanoparticles in this study are above 5 nm in size the energy transfer mechanism is likely to dominate over charge transfer mechanism in the quenching of MB dye[9] .

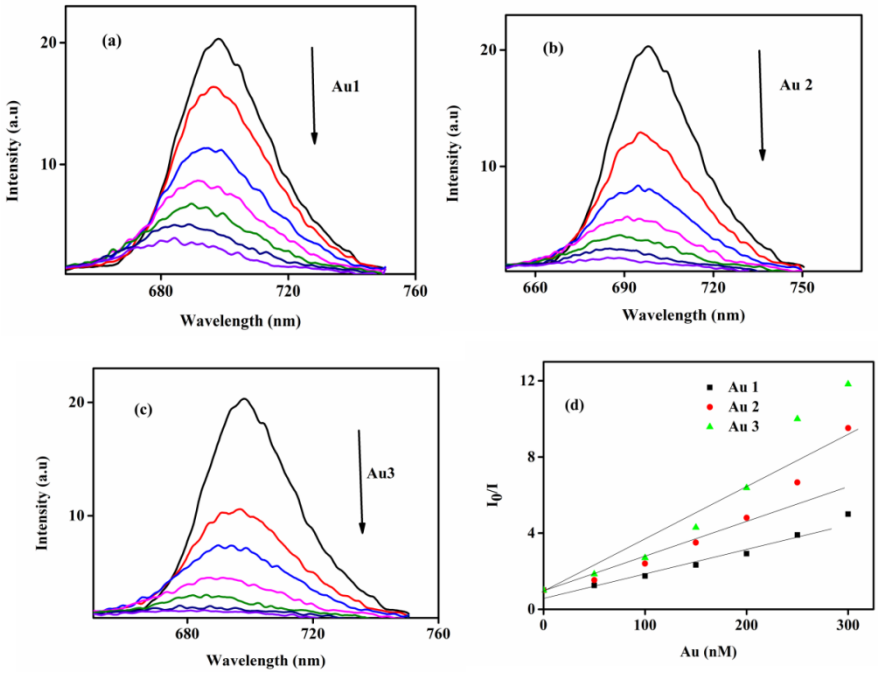

Fig.5.3 Quenching of MB dye with (a) Au1 (b) Au2 (c) Au3 (d) Relative quenching plot

5.3.2 FRET Analysis

In this work we elucidate the quenching of fluorescence of a common dye Methlene Blue through energy transfer mechanism from the excited fluroprobe to the metal nanoparticle in the vicinity assuming that non-radiative energy transfer mechanism (FRET) is the major pathway in the quenching of Methylene blue dye. The FRET occurs when the following conditions are satisfied (a) donor shows fluorescent behaviour (b) proximity and relative orientation of transition dipoles of donor and acceptor (c) overlap of the fluorescence spectrum of the donor with the acceptor absorption (Figure 5.4a and b) (d) distance between the donor and acceptor [10]. The efficiency of the energy transfer is calculated using the following equation

$$E = 1 - \frac{I}{I_0} = \frac{{R_0}^6}{{R_0}^6 + {r_0}^6} \quad \text{..... (3)}$$

Where r_0 is the distance between the donor and acceptor and R_0 is the förster radius in angstrom, corresponding to the distance where the efficiency of energy transfer is 50% and can be calculated using the following equation

$$R_0 = 0.211\ [k^2 n^{-4} Q_D\, J]^{1/6} \quad \text{..... (4)}$$

Where k^2 is the relative orientation of the dipoles of donor and acceptor in space and taken to be 2/3, n is the refractive index of the medium taken to be 1.4, Q_D is the quantum yield of MB dye, J is the overlap integral between MB dye emission and Au NP absorption.

The spectral overlap integral is given by

$$J = \int_0^\infty I_D(\lambda) \in_A (\lambda) \lambda^4 d\lambda \quad \text{..... (5)}$$

Where ϵ is the molar absorption coefficient in M^{-1} cm^{-1}, λ is the wavelength of the light in nm and I_D is the intensity of the fluorescence

spectrum of the donor normalized on the wavelength scale. Q_D was calculated using Rhodamine B as reference using the following equation

$$Q_S = {F_S \times A_R \times {n_s}^2 \times Q_R}/{F_R \times A_S \times {n_r}^2} \quad \text{..... (6)}$$

Where F_S, F_R is integrated fluorescence emission of the sample and reference respectively. A_R, A_S are the absorbances with n_r and n_s being the refractive indexes of the reference and sample respectively. The absorbance of MB dye and overlap of Au1, Au2, Au3 absorption spectra with the MB emission spectrum has been plotted in Fig.5.4.

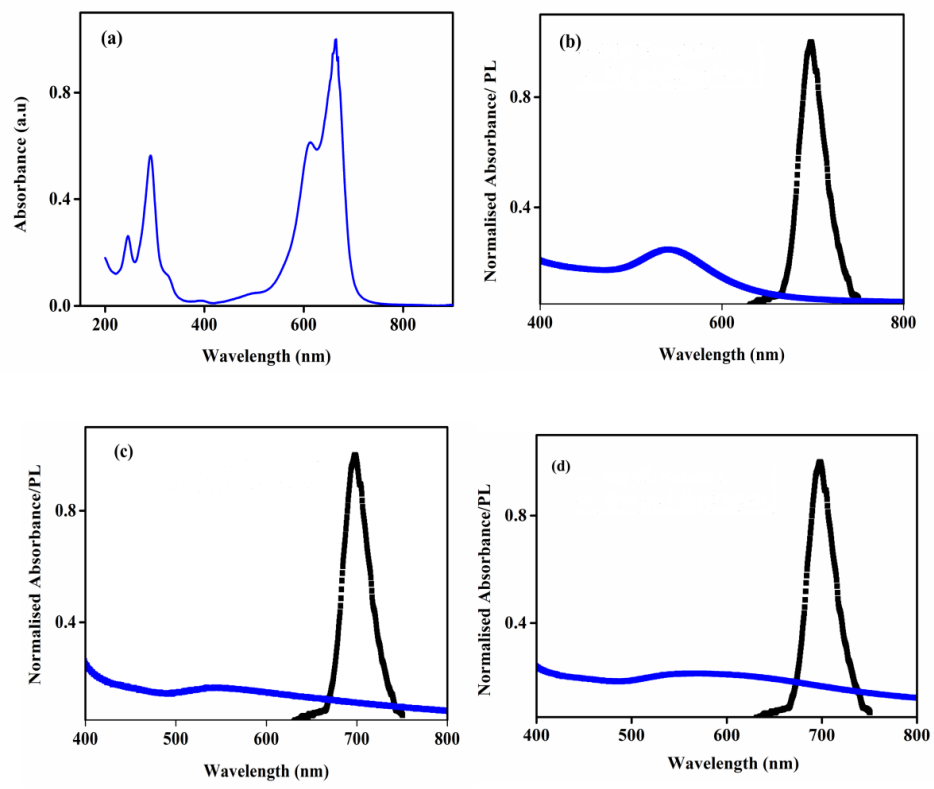

Fig. 5.4 (a) Absorbance of MB dye and Overlap curve of Emission spectrum of MB dye with absorption spectrum of (b) Au1 (c) Au2 (d) Au3

Dye	Emission max (nm)	Absorption (nm)	Quantum yield
MB	**698**	**611, 665**	**0.076 in water**

Table 5.2 Spectral characteristics of MB dye

The overlap integral J for MB-Au 1, Au2 and Au3 combinations was found out using Flurotool software and other relevant parameters were calculated using equations 3 to 6. The values of critical parameters obtained have been presented in Table 5.3.

Hybrid System	Overlap integral J	R_0(nm)	r_0(nm)	E (%)
MB-Au1	2.96×10^{15}	4.1	5.1	20.0
MB-Au2	3.75×10^{16}	6.2	6.9	34.5
MB-Au3	7.5×10^{16}	7.0	7.1	46.7

Table 5.3 FRET parameters of MB-Au system

From the values it is seen that with the increase in extent of overlap the energy transfer efficiency increases. The R_0 values for all the three pairs are below 8 nm which is in agreement with upper limit of FRET, above which the mechanism becomes weaker [11]. The r values lie in the range $0.5R_0$ to $1.5R_0$ showing an efficient energy transfer between MB dye and gold nanoparticles [12].It is seen that the gold nanoaggregates (Au3) show better quenching and highest energy transfer compared to Au2 and Au1.

5.3.3 Photocatalytic studies and energy transfer

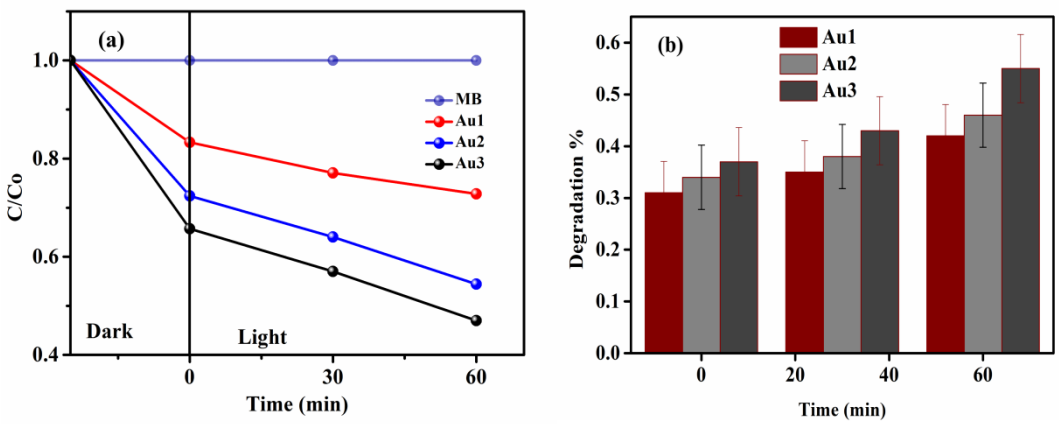

Fig.5.5 (a) Photocatalytic activity of Au1, Au2 and Au3 colloids (b) Degradation plot of the three Au samples

To understand the photocatalytic activity of the gold colloids by the degradation of MB dye, a plot C/C_0 versus time is drawn as shown in Fig.5.5 (a) Where C_0 is the initial concentration and C is the concentration of MB dye at regular intervals. Here pure MB dye was used as a control system. Further the degradation plot (5.5 (b)) it is seen that Au3 nanoparticles degrade MBdye to about 55% after 60 min as compared to 47% for Au2 and 41% for Au1 nanoparticles. From the plot sit is understood that gold colloids synthesized in this work exhibit photocatalytic behaviour and black gold aggregates show better photocatalytic behaviour compared to monodisperse red colloids. In monodisperse noble metal nanoparticles, electron-hole pairs are generated due to Surface Plasmon Resonance (SPR), but are insufficient enough to promote photocatalysis properly due to their high recombination rates compared to semiconductors. But this scenario can be improved by designing plasmonic

superstructures/aggregates with good light harvesting properties due to their special properties like near field enhancement and broadband spectra compared to isolated particles[13]. The close proximity of gold nanoparticles in an aggregate is responsible for strong broadband absorption due to Plasmon Resonance coupling thereby improving the light harvesting of Au2 and Au3 aggregates. LSPR concentrates the light flux (the energy of incoming photons) into a small volume surrounding the gold nanostructure with enhancements in the intensity of electric fields about 10^3 times higher than that of an isolated particle. This creates excited electrons in nanoparticles gaining sufficient energy under visible light irradiation, to activate reactant molecules adsorbed on the Au-NPs and induce chemical reactions[14].

In this work we propose that the FRET between dye molecules and Au nanoparticles plays a constructive role in the photodegradation of the dye by non-radiative energy transfer increasing the number of energetic electrons to carry out photocatalytic reactions on the MB dye molecules. It is seen that Au3 showing maximum energy transfer also shows the maximum catalytic activity as shown in Fig.5.5. On comparison with Table 5.3 it is seen that the photocatalytic activity increases with increase in FRET from Au1 to Au3.The transfer of excitation energy from Donor dye (MB) to acceptor (Au nanoparticles) results in the further accumulation of photoexcited charge carriers on the surface of Au nanoparticles. Thus the synergy of radiative effects due to plasmonic enhancement and non-radiative effects like FRET help in achieving direct photocatalysis of dyes using nanomolar concentrations of Au nanoparticles as shown in Fig. 5.6

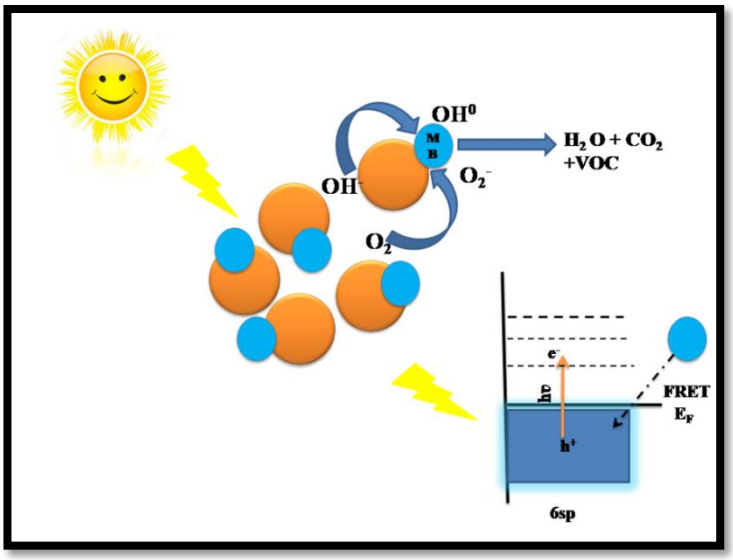

Fig. 5.6 Scheme depicting photocatalysis and FRET involvement between MB dye and Au NPs

4. Conclusion

The gold nanoparticles of different sizes synthesized via green protocol were studied for their interaction with MB dye in this work. It was observed that the gold nanoparticles quenched MB dye fluorescence as indicated by PL measurements. The quenching was more prominent for aggregate structures Au2 and Au3 showing broadband spectra compared to monodisperse Au1. It was proposed that non-radiative energy transfer mechanism FRET is occurring between Dye and Au nanoparticles. The FRET parameters were calculated and all the three FRET pairs showed R_0 distance below 8 nm indicating FRET to be the dominating mechanism in the limit. The FRET efficiency increased with increase in size/shape of the nanoparticles and this was exploited to conduct photocatalytic dye degradation. It was observed that Au3 with highest FRET exhibits the highest photocatalytic degradation indicating that FRET helps in increasing photoexcited charge carriers for reacting with dye molecules for

their degradation. Thus FRET between MB dyes –Au nanoparticle helps in direct photocatalysis of the dye which can be used for water purification purposes.

References:

[1] P. V Kamat, Meeting the Clean Energy Demand : Nanostructure Architectures for Solar Energy, J.Phys.Chem.C. 111 (2007) 2834–2860.

[2] M. Rochkind, S. Pasternak, Y. Paz, Using Dyes for Evaluating Photocatalytic Properties :, Molecules. 20 (2015) 88–110.

[3] M.-H.W. Peng Wang, Baibiao Huang, Ying Dai, Plasmonic photocatalysts: harvesting visible light with noble metal nanoparticles, Phys. Chem. Chem. Phys. 14 (2012) 9813–9825.

[4] S.Y. Park, S.M. Lee, G.B. Kim, Y. Kim, Gold nanoparticle-based fluorescence quenching via metal coordination for assaying protease activity, Gold Bull. 45 (2012) 213–219.

[5] R. Shrivastava, B. Jain, K. Das, Spectroscopic investigations on the binding of Methylene Blue and Nile Blue to negatively charged gold nanorods, J. Mol. Struct. 1020 (2012) 56–62.

[6] J. Yu, C. Hsu, C. Huang, P. Chang, Development of Therapeutic Au–Methylene Blue Nanoparticles for Targeted Photodynamic Therapy of Cervical Cancer Cells, ACS Appl. Mater. Interfaces. 7 (2015) 432–441.

[7] L. Li, J. Liu, X. Yang, Z. Peng, W. Liu, J. Xu, J. Tang, X. He, K. Wang, Quantum dot / methylene blue FRET mediated NIR fluorescent nanomicelles with large Stokes shift for bioimaging, Chem Comm. 51 (2015) 14357–14360.

[8] X. Liu, M. Atwater, J. Wang, Q. Huo, Extinction coefficient of gold

nanoparticles with different sizes and different capping ligands, Colloids Surfaces B Biointerfaces. 58 (2007) 3–7.

[9] S.R. Kavitha, M. Umadevi, S.R. Janani, T. Balakrishnan, R. Ramanibai, Spectrochimica Acta Part A : Molecular and Biomolecular Spectroscopy Fluorescence quenching and photocatalytic degradation of textile dyeing waste water by silver nanoparticles, Spectrochim. ACTA PART A Mol. Biomol. Spectrosc. 127 (2014) 115–121.

[10] S.A. Selvaraj Naveenraj, Ramalinga Viswanathan Mangalaraja, Jerry J. Wu, Abdullah M. Asiri, Gold Triangular Nanoprisms and Nanodecahedra : Synthesis and Interaction Studies with Luminol toward Biosensor Applications, Langmuir. 2 (2016) 11854–11860.

[11] T. Sen, S. Sadhu, A. Patra, Surface energy transfer from rhodamine 6G to gold nanoparticles: A spectroscopic ruler, Appl. Phys. Lett. (2012) 1–4.

[12] S. Naveenraj, R.V. Mangalaraja, J.J. Wu, M. Asiri, S. Anandan, Gold triangular nanoprisms and nanodecahedra – synthesis and interaction studies with Luminol towards biosensor applications, Langmuir. 32 (2016) 11854–11860.

[13] S. Linic, P. Christopher, D.B. Ingram, Plasmonic-metal nanostructures for efficient conversion of solar to chemical energy, Nat. Mater. 10 (2011) 911–921.

[14] J. Yang, Y. Li, L. Zu, L. Tong, G. Liu, Y. Qin, D. Shi, Light-concentrating plasmonic au superstructures with significantly visible-light-enhanced catalytic performance, ACS Appl. Mater. Interfaces. 7 (2015) 8200–8208.

FRET BETWEEN QUANTUM DOTS AS DONOR AND ACCEPTORS IN A HYBRID SYSTEM

6.1. Introduction:

Solar energy conversion and photovoltaics have assumed unprecedented importance in the recent times due to the emerging power crisis and environmental concerns. The third generation photovoltaics like DSSC have been extensively studied due to their low fabrication cost and good photoresponse in visible region [1]. Quantum dot sensitized solar cells (QDSSC) developed along with DSSC have also shown great promise in the recent years. Quantum dots (QDs) are tiny semiconductor nanomaterials with exciting physical and chemical properties due to quantum confinement effects [2].

The QDSSC follows the same operational principle like DSSC though the anchoring of QD to TiO_2 is not as effective as dye. Hence inspite of major breakthroughs in efficiencies QDSSC is yet to achieve the level of performance of DSSC. Inspite of these shortcomings QDSSC research holds promise are its interesting optical properties, stability and low cost compared to costly molecular dyes.

One of the successful methods in improving the photoresponse of the solar cell is to design hybrid structures showing Forster Resonance Energy Transfer (FRET) mechanism. QDs with excellent photophysical properties like bright stable emission, large stokes shift, long fluorescent lifetimes satisfy the primary requisite for a FRET donor [3]. The advantages of QD as donor in QD-Dye

nanohybrids leading to high efficiencies has been well documented in various reports [4]. But in contrast QD-QD hybrid systems suffer from shortcomings inspite of their photostability compared to organic dyes. Though QD-QD systems are feasible and have been successfully used in various biological applications the proper utilization of a QD-QD system with attractive efficiencies is yet to be realised in the QDSSC scenario [5]. The effective absorption of the sensitizer in the visible region is the key factor to any light harvesting assembly. Semiconductor quantum dots like CdSe absorb in the visible region have been used as sensitizers and energy donors in hybrid solar cells leading to considerable improvement in efficiencies [6–8]

Here, we have used CdSe as acceptors and Graphene quantum dots (GQD) as donors in the QD-QD FRET system. GQDs are known to absorb at shorter wavelength region due to the pi-pi* transition of the aromatic network in the basal structure of GQD. GQDs by virtue of their unique configuration exhibit stable fluorescence which puts them in a better position over the conventionally used semiconductor QDs [9]. Apart from good optical behaviour GQDs possess chemical stability which makes them one of the most sought out new generation materials for a wide variety of applications [10].

Further GQDs have been explored as energy donors for N719 dyes with considerable efficiencies as reported in the recent times [11]. A hybrid solar cell with GQD as energy donor to CdSe sensitized TiO_2 solar cell has been designed in this experiment. The improved efficiency of the CdSe sensitized cell with the introduction of GQD has been justified by non radiative energy transfer mechanism using spectral matching, photoluminescence and lifetime measurements.

6.2. Experimental Section

6.2.1Materials

Cadmium chloride, Selenium, 3-mercaptopropionic acid (MPA) were purchased from Sigma Aldrich and used directly without further purification. TiO_2 nanoparticles (P 25), Fluorine doped tin oxide (FTO-7Ω/Sqcm), hexachloroplatinic acid (H_2PtCl_6) , potassium iodide (KI) (99.5%), N719 dye were obtained from Sigma-Aldrich and iodine (I_2) from MERCK. Distilled water (Millipore System), Acetone, Ethanol and Methanol (≥ 99% Sigma Aldrich) were used as solvents.

6.2.2 Synthesis of CdSe QD and GQDs

CdSe quantum dots were prepared by previously reported method using a solution route at ambient temperature [12]. Briefly, aqueous solution of cadmium chloride was prepared with addition of a required amount of MPA (0.24 M) under constant stirring to get a clear solution at pH maintained between 9 and 10. Further selenium powder dissolved in hydrazine hydrate was slowly added to the solution to get a pale yellow colloid.

GQDs were prepared through a two-step process that is formation of graphene oxide (GO) from graphite flakes and further reduction to graphene QDs as reported in literature with minor modifications. Firstly GO was obtained by oxidation of graphite treated with a mixture of H_2SO_4 and H_2PO_4 along with $KMnO_4$ using Tour's method [13] in an ice bath. Afterwards continuous stirring followed by addition of hydrogen peroxide resulted in oxidised form of graphite. This solution on being subjected to ultrasonication

leads to graphene oxide. The obtained graphene oxide (0.5mg/ml) is mixed with required amount of water and ascorbic acid and put in an autoclave at 200 ^{o}C for six hours. After cooling the supernatant liquid was taken out through a syringe filter to be used for further characterisations.

6.2.3Fabrication of QDSSC device

The FTO glass plates were first cleaned using detergent solution followed by successive washing with distilled water, isopropanol and acetone using an ultrasonicator. These plates after drying were doctor bladed with TiO_2 paste prepared using TiO_2 powder, ethanol and TritonX-100. These electrodes after air drying overnight were sintered at 450 ^{o} C for 30 minutes. On cooling, the area confinement of 0.25 cm^2 was done and the TiO_2 electrode was dipped in CdSe colloid for 0.5,2, 5 and 12 hours. Further the GQDs were dropcasted onto the optimised photoanode kept at 40 °C in a hot air oven. The electrolyte was prepared by mixing 0.6 M 4-butyl methyl imidazolium iodide (BMII), 0.04 M Iodine (I_2), 0.1 M lithium iodide (LiI), 0.1 M guanidiumthiocyanate (GuSCN) and 0.5 M tertiary butyl pyridine in acetonitrile. The hybrid photoanode and electrodeposited Pt counter electrode were assembled to form a solar cell by sandwitching the redox electrolyte using binder clips.

6.2.4 Characterisation Techniques

The UV-Vis spectrophotometer (T90, PG Instruments) was used to measure the nature of absorbance of the nanoparticles in the visible range of the solar spectrum. The size of the synthesized nanoparticles was determined by transmission electron microscopy (TEM) Jeol/ JEM 2100 using LaB6 source operated at 200 kV. Fourier transform infrared spectra (FTIR) of GQDs and

CdSe were measured using PerkinElmer Spectrum Two FTIR spectrometer in the wavenumber range of 4000-450 cm^{-1}. The photoluminescent (PL) measurements were conducted using PerkinElmer (LS 55) in the visible range.For measuring the performance of DSSC, current-voltage (I-V) characteristics were done using solar simulator (Scientech) under 1 sun illumination (100 mW/cm^2). The pulsed diode excitation of 370 nm from Flurocube-lifetime system (JOBIN-VYON) was used to measure lifetimes of the samples.

6.3. Results and Discussion

6.3.1 TEM and SEM analysis

TEM studies were conducted to understand the size/morphology of the GQD and CdSe colloids. Fig.6.1a and c represents the TEM images of GQD and CdSe showing homogenous distribution of particles. The sizes are observed to be below 10nm. The synthesized samples CdSe and GQD are well dispersed and uniformly distributed making them suitable for solar cell fabrication. The presence of fringes along with the bright spots in SAED pattern shows the crystallite nature of the samples (Fig. 6.1b and d).

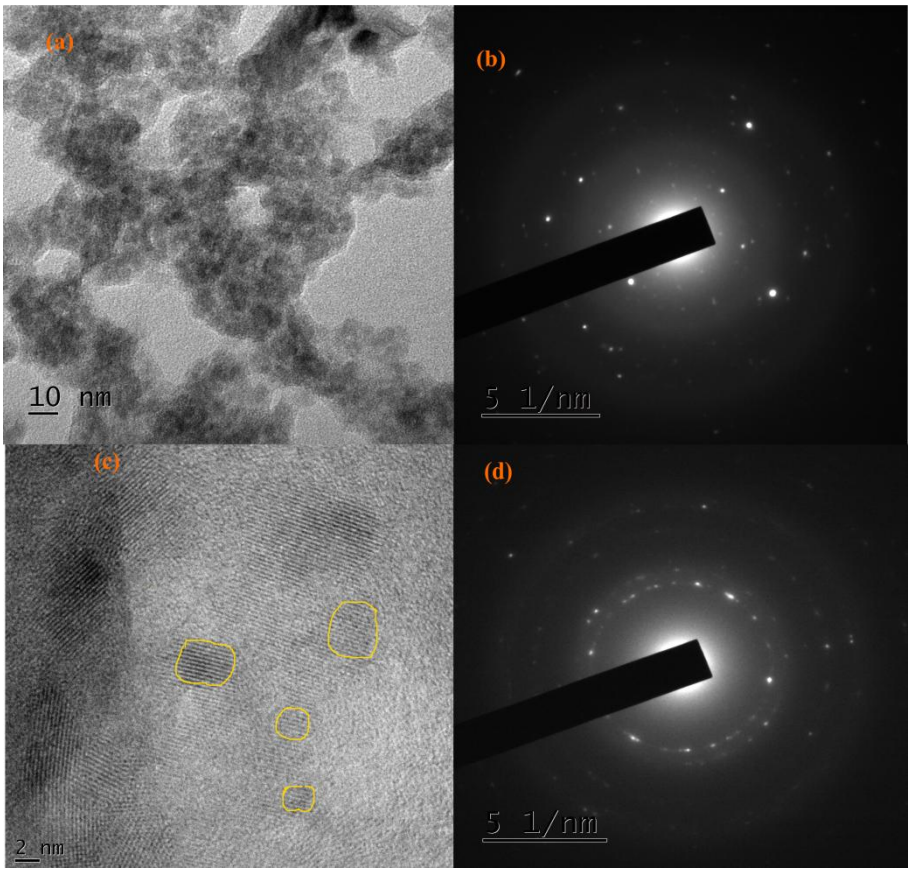

Fig. 6.1 (a) GQD TEM (b) GQD SAED (c) CdSe TEM (d) CdSe SAED

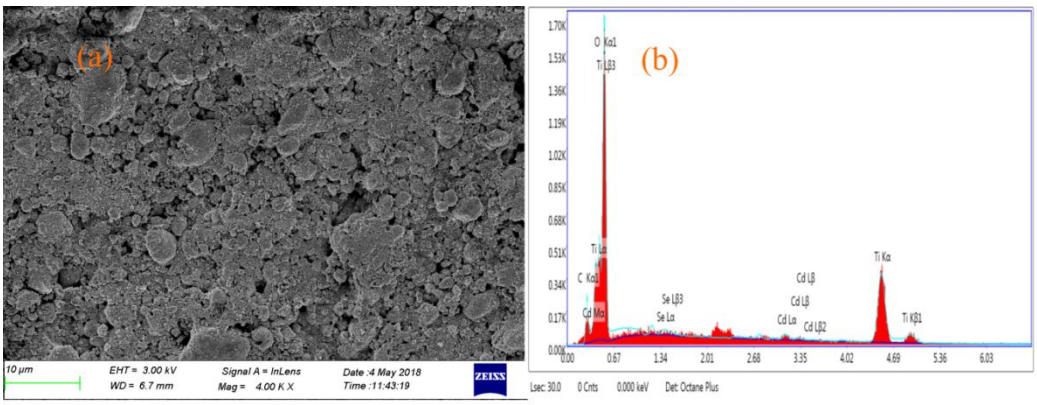

Fig.6.2 GQD-CdSe Hybrid photoanode (a) SEM image and (b) EDAX spectrum

The SEM and EDAX spectra of the hybrid photoanode are presented in Fig.6.2a and b. The peaks corresponding to C, Cd, Se indicate the presence of these elements in TiO_2 photoanode.

6.3.2 Optical Properties

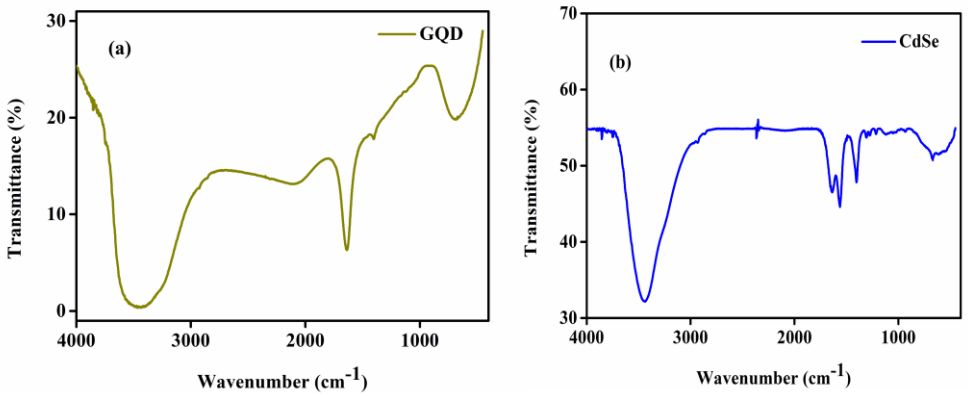

Fig.6.3 FTIR spectrum of (a) GQD (b) CdSe QD solution

Fourier Transform Infrared (FTIR) analysis of the GQD and CdSe solutions are shown in Fig. 6.3a and 6.3b. The GQD solution shows a broadband centred at 3487 cm^{-1} representing free O–H bonding. The bands at 1399 cm^{-1} and 1647 cm^{-1} reveal the presence of C–H bonding and aromatic ring respectively [14].

The 3455 cm^{-1} peak in the CdSe solution correspond to the O-H vibration and the small peaks at 2923 cm^{-1}, 2855 cm^{-1} correspond to the CH stretching vibrations due to MPA molecules respectively. The peaks at 1644 cm^{-1} , 1399 cm^{-1} correspond to the vibration of free carboxylic acid and symmetric stretching vibration of C-O groups as reported elsewhere [15] .

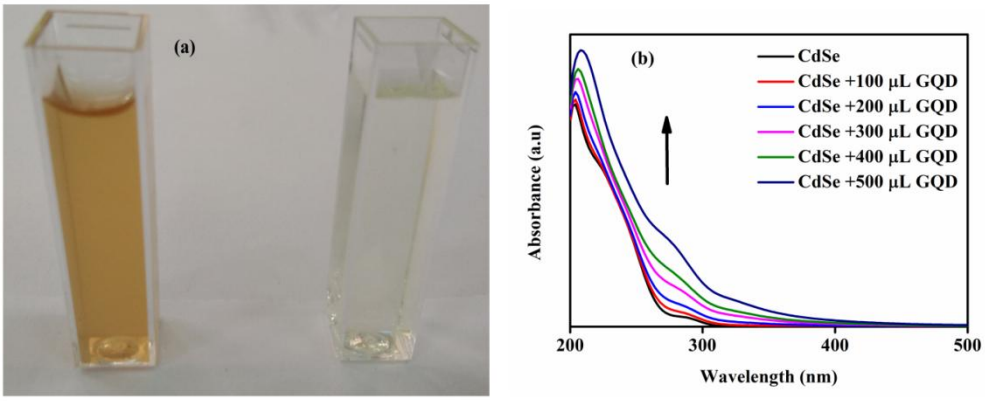

Fig. 6.4 (a) GQD (yellow) and CdSe (colourless) solution (b) absorption of fixed amount of CdSe with increasing GQD

Figure 6.4(a) shows the prepared GQD and CdSe solutions for solar cell applications. Figure 6.4 (b) shows the increase in absorption of the CdSe solution with increasing amount of GQD in 200-400 nm regions. The increase in absorbance in CdSe upon addition of GQD may be responsible for the increase in light absorption by the CdSe photo-anode, however it is seen that major absorption in the region of 300-400 nm corresponding to the absorption of the two quantum dots. This narrow spectral window may be the reason for the lower efficiencies of the solar cells used in this study.

6.3.3 Pl quenching and FRET parameters

The Fig.6.5 (a) shows a reasonable overlap between the CdSe QD acceptor absorption spectrum and GQD donor emission spectrum indicating possibility of energy transfer (FRET) from GQD to CdSe.

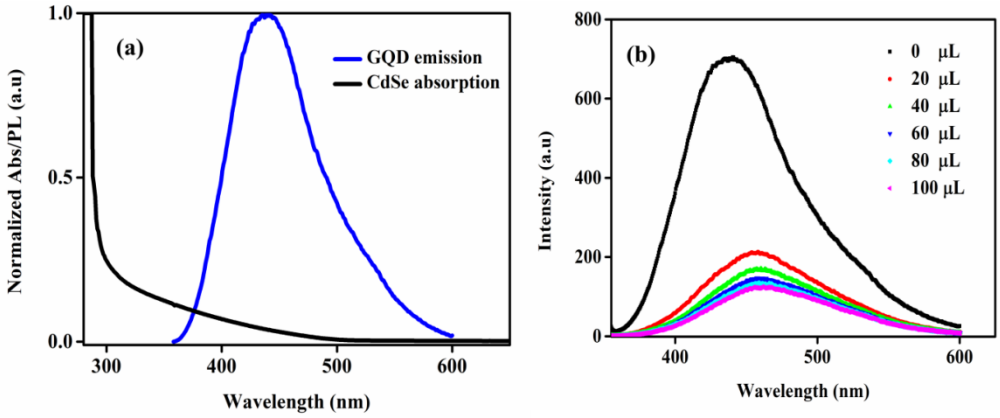

Fig.6.5 (a) Spectral overlap of GQD emission and CdSe absorption (b) PL quenching of GQD in presence of different volumes of CdSe QDs

The absorption spectra of CdSe shows absorption in 200-300 range with a tail extending to the visible region, whereas a broad emission peak starting from 357 nm upto 600 nm is seen in the case of GQDs. Figure 6.5b shows the quenching of GQD emission in the presence of different concentrations of CdSe quantum dots indicating energy transfer from the donor (GQD) to the acceptor (CdSe).

The FRET radius R_o corresponding to the distance between the donor and acceptor at which probability of energy transfer is 50% is given by

$$R_0 = 0.0211(k^2 \times n^{-4} \times Q_D \times J_\lambda)^{1/6} \quad \text{in nm}$$

Where k^2 is taken to be 2/3, n is the refractive index of water taken to be 1.33, Q_D is the quantum yield and J_λ is the spectral overlap integral between the donor emission and acceptor absorption.

The spectral overlap integral is expressed as

$$J = \int_0^\infty I_D(\lambda) \in_A (\lambda)\lambda^4 d\lambda$$

Where ϵ is the molar absorption coefficient in M^{-1} cm^{-1}, λ is the wavelength of the light in nm and I_D is the emission spectrum of the donor normalized on the wavelength scale [16]. The quantum yield of GQD Q_S was calculated using quinine sulphate in 0.1 M H_2SO_4 as reference Q_R (0.54) using the following equation

$$Q_S = {F_S \times A_R \times {n_s}^2 \times Q_R}\Big/{F_R \times A_S \times {n_r}^2}$$

Where F_S,F_R is integrated fluorescence emission of the sample and reference respectively. A_R and A_S are the absorbance at the exciting wavelength of the reference and sample and n is the refractive index which is same for both sample and reference (water in this case).

From the calculation R_0 was found to be 2.8 nm pointing towards FRET mechanism which occurs in the range of 1-10 nm [17]. The energy transfer E_T in terms of R_0 is given by the following equation

$$E_T = \frac{R_0^6}{r^6 + R_0^6}$$

Where r is the distance between the donor-acceptor pair of GQD-CdSe FRET system. Further to test the energy transfer between GQDs and CdSe QDs fluroscence spectra of GQD with successive addition of CdSe is studied as shown in Fig. 6.5b. The decrease in PL intensity of GQD with the increase in concentration of CdSe provides evidence of resonance energy transfer from donor to acceptor.

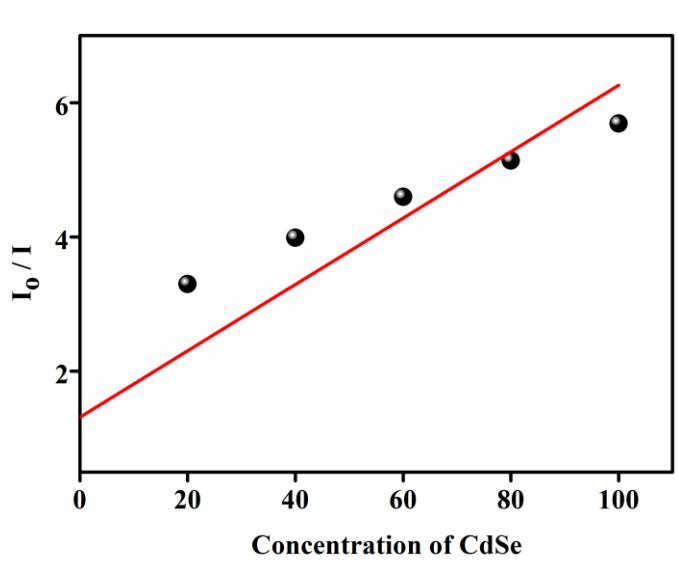

Fig.6.6 Stern –Volmer Plot

The fluorescence efficiency is quantified using Stern-Volmer equation and (S-V) plot [18] is drawn (Fig. 6.6) to show quenching of the Donor (GQD) with respect to the acceptor (CdSe) .

$$\frac{I_0}{I} = 1 + K_{SV}[Q]$$

Here I_0 and I represent the GQD emission intensity in the absence and presence of the acceptor CdSe QD. It is seen that $\frac{I_0}{I}$ (quenching efficiency) increases with increase in concentration of CdSe. From the slope the K_{SV} (Stern-Volmer) constant is calculated to be $0.0494 \times 10^6 \pm 0.01\ M^{-1}$ similar to values reported elsewhere strongly suggesting non-radiative transfer via FRET mechanism [8].

6.3.4 Solar Cell Characterisations and Lifetime measurements

To utilise FRET to improve energy harvesting in real energy conversion application, QD-QD hybrid architecture in DSSC was constructed and tested

for cell performance as shown in Fig.6.7. The device fabrication was done through different methods (a) Cdse dip coated into TiO_2 and GQD dropcasted on it (b) GQD alone (GQ1) , GQD dipcoated first and then CdSe dropcasted (GQ2), and both CdSe and GQD dipcoated (GQ3).

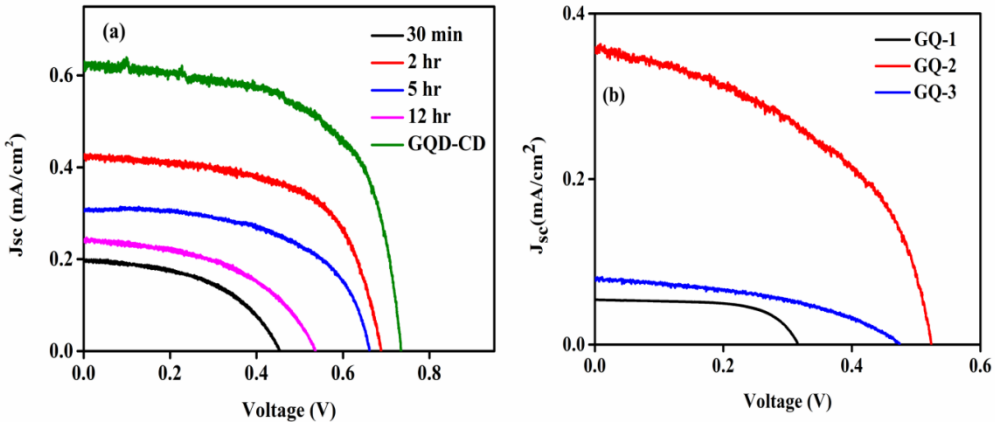

Fig.6.7 J-V curves of different cell configurations (a) CdSe dipping times of 30 min to 12 hours and dropcasted by GQD (GQD-CD) (b) GQ1, GQ2, GQ3

The TiO_2 photoanodes were dip coated in CdSe solution for various dipping times 0.5, 2, 5, 12 hours for QDSSC configuration and two hours dipping was seen to give the best efficiency. The CdSe cell with 2 hour dipping was chosen to be used as the hybrid cell because of its optimum performance. It is observed that the efficiency of the CdSe cells does not improve with increasing the dipping time. The poor performance of CdSe cells with higher dipping time could be due to the aggregation of QDs on the surface leading to higher resistance to electron transfer [19]. The results for CdSe cells with various dipping times and different combinations of hybrid cells of GQD and CdSe have been tabulated in Table 6.1.

Sample	Jsc (mA)	Voc (V)	FF (%)	Efficiency ŋ (%)
CdSe- TiO_2 - 0.5 hr	0.196	0.454	50.4	0.045
CdSe- TiO_2 - 2 hr	0.424	0.688	62.0	0.180
CdSe- TiO_2 - 5 hr	0.308	0.661	57.7	0.117
CdSe- TiO_2 - 12 hr	0.240	0.537	50.4	0.065
GQD-CD-TiO_2-2 hr	0.620	0.735	61.4	0.280
GQ 1 (GQD – TiO_2)	0.054	0.316	63.7	0.010
GQ2(CD-GQD- TiO_2)	0.365	0.523	47.7	0.088
GQ3 (GQD-CD – TiO_2)	0.080	0.474	43.8	0.016

Table 6.1 Photo-electrochemical parameters of CdSe –GQD solar cells

From the values presented in Table 6.1, it is observed that photoanode with dip coating of CdSe and drop casting of GQD dropcasted (GQD-CD- TiO_2-2 hr) shows the maximum efficiency compared to hybrid cells GQ2 and GQ3.

The dip coating of both quantum dots in GQ3 gives lesser efficiency of 0.016% which may be due to the incomplete attachment of the sensitizers to the photo-electrode surface due the leakage of water based sensitizers. The GQ2 system first sensitizes with GQD and then sensitizes with CdSe shows an efficiency of 0.088%. Highest efficiency of 0.28 % is observed for the cell with CdSe dip coating (2Hrs.) followed by GQD dropcasting over TiO_2 photo-electrode.

The reason for the lowered efficiency in GQ2 is that GQD having lesser sensitizing ability compared to CdSe is not suitable for being the first sensitizing layer to TiO_2 photo-anode (GQ1) as shown in Table 1. This also confirms that the FRET donor (GQD) helps the acceptor in facilitating electron

transfer to photo-anode and does not act as a co-sensitizer. The most favoured device design is the acceptor being the first sensitizing layer followed by donor as represented in GQD-CD system. The GQD-CD hybrid cell shows an efficiency enhancement of 55% from 0.18% to 0.28%. The GQD-CD photo-anode had an improved J_{sc} of 0.62 mA/cm^2 compared to 0.424 mA/cm^2 of bare CdSe photo-anode showing 46% enhancement.

Similarly V_{oc} also showed improvement from 0.688V to 0.735 V in a hybrid QD cell showing an increase of 6.7%. It is seen that the increase in J_{sc} contributes majorly to the efficiency enhancement compared to the slight increase of V_{oc} of the hybrid cell. This also supports energy transfer between GQD and CdSe leading to more excited states in CdSe driving more electrons to the conduction band of TiO_2 resulting in increased photocurrent generation [20].

To confirm the energy transfer from GQD to CdSe QD decay measurements were taken using Time Correlated Single Photon Counting (TCSPC) studies using a laser excitation of 370 nm and fitted the curves using a three exponential function. The average decay times are 0.41 and 0.21 nanoseconds for GQD and GQD-CD respectively. The shortening of lifetime confirms the presence of FRET from GQD to CdSe as shown in the Fig. 6.8

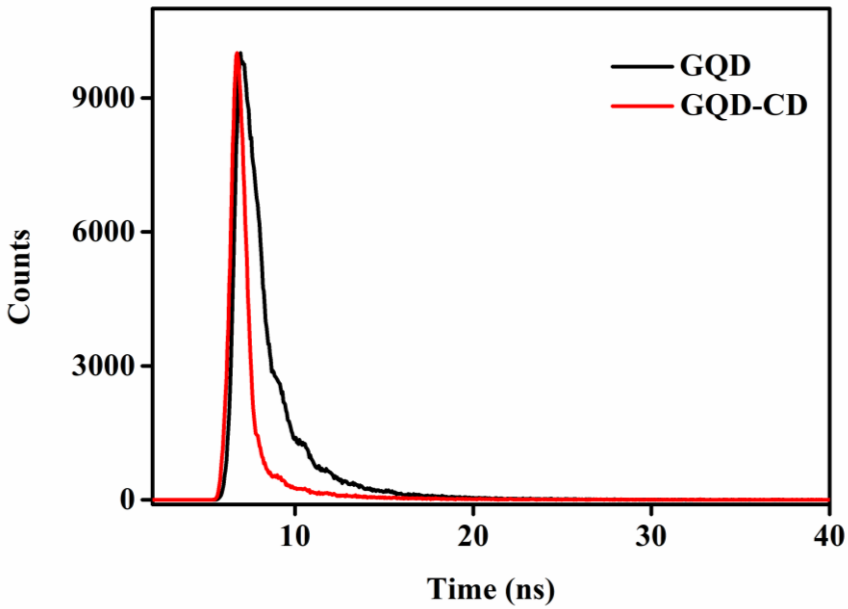

Fig. 6.8 Lifetime measurement curves of GQD in the presence and absence of CdSe

The energy transfer efficiency (E_T) and rate of energy transfer k_T is expressed through the following formula in terms of lifetime

$$E_T = 1 - \frac{\tau_{DA}}{\tau_D}; k_T = \frac{1}{\tau_D} \times \left(\frac{R_0}{r}\right)^6$$

Where τ_{DA} and τ_D are the lifetimes of donor in presence and absence of acceptor respectively [21]. From the average lifetime values the energy transfer is calculated to be 48.7% as shown in Table 2.

GQD (τ_D)	CdSe (τ_A)	GQD-CD (τ_{DA})	k_T (transfer rate)	E_T
0.41 ns	0.14 ns	0.21 ns	2.29×10^8 s^{-1}	48.7 %

Table 2 FRET parameters of the GQD-CdSe Hybrid Cell

From the lifetime measurements it is clearly evident that FRET occurs between the GQD-CdSe pair and that is responsible for the improvement in efficiency of the solar cell.

4. Conclusion

The rarely reported FRET between GQD as donor and CdSe as acceptor has been explored in a QDSSC. The QDs synthesized through a known protocol were investigated for energy transfer efficiencies in a QD-QD hybrid system. The PL quenching experiments and lifetime measurements confirmed the energy transfer from GQD to CdSe QD. The solar cell studies were conducted to exploit this energy transfer to improve the efficiency of the solar cells. The cell fabrication first involved the CdSe dipcoating optimisation with dipping times varying from 0.5 to 12 hours. The optimised performance was obtained for 2 hour dipcoating on which GQD was dropcasted to make a hybrid cell with the best performance. The energy efficiency improved from 0.18 % to 0.28% for hybrid cell showing 55.5 % enhancement in the efficiency. The major contribution to efficiency comes from Jsc which increases to 0.62 mA/cm^2 compared to 0.424 mA/cm^2 of bare CdSe photoanode showing 46% enhancement. The Voc increases slightly from 0.688V to 0.735 V in a hybrid solar cell showing an enhancement of 6.8%. The FRET mechanism is elucidated through PL quenching and lifetime measurements with an energy transfer of about 48.7%. Though the efficiency presented in this FRET system is low this combination is likely to be helpful in harnessing selective regions particularly near UV regions of the electromagnetic spectrum for major breakthroughs in future applications

References:

[1] O.E. Semonin, J.M. Luther, M.C. Beard, Quantum dots for next-generation photovoltaics, Mater. Today. 15 (2012) 508–515.

[2] W. Wang, G. Jiang, J. Yu, W. Wang, Z. Pan, N. Nakazawa, Q. Shen, X. Zhong, High Efficiency Quantum Dot Sensitized Solar Cells Based on Direct Adsorption of Quantum Dots on Photoanodes, ACS Appl. Mater. Interfaces. 9 (2017) 22549–22559.

[3] S. Kundu, A. Patra, Nanoscale Strategies for Light Harvesting, Chem. Rev. 117 (2017) 712−757.

[4] S. Buhbut, S. Itzhakov, E. Tauber, M. Shalom, I. Hod, T. Geiger, Y. Garini, D. Oron, A. Zaban, Built-in quantum dot antennas in dye-sensitized solar cells, ACS Nano. 4 (2010) 1293–1298.

[5] K. Chou, A. Dennis, Förster Resonance Energy Transfer between Quantum Dot Donors and Quantum Dot Acceptors, Sensors. 15 (2015) 13288–13325.

[6] M.A. Shivkumar, L.S. Inamdar (Doddamani), M.H.K. Rabinal, B.G. Mulimani, G.M. Advi Rao, S.R. Inamdar, FRET from CdSe / ZnS Core-Shell Quantum Dots to Fluorescein 27 Dye, Open J. Phys. Chem. 3 (2013) 40–48.

[7] L. Etgar, J. Park, C. Barolo, V. Lesnyak, S.K. Panda, P. Quagliotto, S.G. Hickey, M.K. Nazeeruddin, A. Eychmüller, G. Viscardi, M. Grätzel, Enhancing the efficiency of a dye sensitized solar cell due to the energy transfer between CdSe quantum dots and a designed squaraine dye, RSC

Adv. 2 (2012) 1–5.

[8] S. Sadhu, K.K. Haldar, A. Patra, Size Dependent Resonance Energy Transfer between Semiconductor Quantum Dots and Dye Using FRET and Kinetic Model, J. Phys. Chem. C. 114 (2010) 3891–3897.

[9] Q. Xu, Q. Zhou, Z. Hua, Q. Xue, C. Zhang, X. Wang, D. Pan, M. Xiao, Single-particle spectroscopic measurements of fluorescent graphene quantum dots, ACS Nano. 7 (2013) 10654–10661.

[10] S. Zhu, J. Zhang, S. Tang, C. Qiao, L. Wang, H. Wang, X. Liu, B. Li, Y. Li, W. Yu, X. Wang, H. Sun, B. Yang, Surface chemistry routes to modulate the photoluminescence of graphene quantum dots: From fluorescence mechanism to up-conversion bioimaging applications, Adv. Funct. Mater. 22 (2012) 4732–4740.

[11] A. Subramanian, Z. Pan, G. Rong, H. Li, L. Zhou, Graphene quantum dot antennas for high efficiency Förster resonance energy transfer based dye-sensitized solar cells, J. Power Sources. 343 (2017) 39–46.

[12] M.N. Kalasad, M.K. Rabinal, B.G. Mulimani, Ambient synthesis and characterization of high-quality CdSe quantum dots by an aqueous route, Langmuir. 25 (2009) 12729–12735.

[13] D.C. Marcano, D.V. Kosynkin, J.M. Berlin, A. Sinitskii, Z. Sun, A. Slesarev, L.B. Alemany, W. Lu, J.M. Tour, Improved Synthesis of Graphene Oxide, ACS Nano. 4 (2010) 183–191.

[14] C.M. Luk, L.B. Tang, W.F. Zhang, S.F. Yu, K.S. Teng, S.P. Lau, An efficient and stable fluorescent graphene quantum dot–agar composite as

a converting material in white light emitting diodes, J. Mater. Chem. 22 (2012) 22378–22381.

[15] N.T. Vo, H.D. Ngo, D.L. Vu, A.P. Duong, Q. V. Lam, Conjugation of E. coli O157:H7 Antibody to CdSe/ZnS Quantum Dots, J. Nanomater. 2015 (2015) 1–7.

[16] S. Sarkar, A. Makhal, T. Bora, S. Baruah, J. Dutta, S.K. Pal, Photoselective excited state dynamics in ZnO–Au nanocomposites and their implications in photocatalysis and dye-sensitized solar cells, Phys. Chem. Chem. Phys. 13 (2011) 12488.

[17] M. Lunz, A.L. Bradley, V.A. Gerard, S.J. Byrne, Y.K. Gun, V. Lesnyak, N. Gaponik, Concentration dependence of Förster resonant energy transfer between donor and acceptor nanocrystal quantum dot layers : Effect of donor-donor interactions, Phys. Rev. B. 83 (2011) 1–10.

[18] D.S. Rahman, S. Deb, S.K. Ghosh, Relativity of Electron and Energy Transfer Contributions in Nanoparticle-Induced Fluorescence Quenching, J. Phys. Chem. C. 119 (2015) 27145–27155.

[19] M.-S. Jeong, M.-K. Son, S.-K. Kim, S. Park, K. Prabakar, H.-J. Kim, Study on characteristics of CdS quantum dot-sensitized solar cells prepared by successive ionic layer adsorption and reaction with different adsorption times, Electron. Mater. Lett. 10 (2014) 621–626.

[20] A. Gopi, S. Lingamoorthy, S. Soman, K. Yoosaf, R. Haridas, S. Das, Modulating FRET in Organic-Inorganic Nanohybrids for Light Harvesting Applications, J. Phys. Chem. C. 120 (2016) 26569–26578.

[21] A. Makhal, S. Sarkar, T. Bora, S. Baruah, J. Dutta, A.K. Raychaudhuri, S.K. Pal, Role of Resonance Energy Transfer in Light Harvesting of Zinc Oxide-Based Dye-Sensitized Solar Cells, J. Am. Chem. Soc. 114 (2010) 10390–10395.

CHAPTER 7

DYE-DYE HYBRID SOLAR CELL

DYE-DYE HYBRID SOLAR CELL

7.1 Introduction:

The dye sensitized solar cells have emerged as one of the promising technologiesfor affordable solar cells applications in future [1]. However the effective utilisation of DSSC for enhanced power conversion still faces many hurdles. One of the major challenges is to obtain a cheap, environment friendly sensitizer which can replace the costly ruthenium dyes and still obtain reasonable efficiencies[2]. Though natural dyes have made progress in this regard, still most of the dyes alone are insufficient to get competing efficiencies[3]. To overcome this problem, two or more dyes have been used in solar cells to increase the spectral window of the individual sensitizer[4].

Two natural dyes obtained from leaves of red amaranth were used as photosensitizers for DSSC in this work. The investigations conducted indicate that the dyes extracted using water and ethanol arebetalain (red dye) and chlorophyll (green dye) respectively.The extracted dyes were characterized by UV-Vis absorption spectra and their structures confirmed through FTIR spectra. The photoelectrochemical properties of the DSSC using these extract as sensitizers was investigated and it was found that the green dye performs better with an efficiency of 0.53%.

To improve the efficiency of the prepared solar cell and toimprove light absorbance, a hybrid cell is constructed using two dyes as sensitizers.One of the efficient ways to enhance energy harvesting in solar cells is through FRET mechanism. In FRET one dye acts as an acceptor and one acts as a donor whose emission overlaps with the absorbance spectrum of the acceptor. The

donor non-radiatively transfers its energy to the acceptor which acts as the sensitizer in the solar cell. The donors therefore perform as antennaeor energyrelaywhose primary function is the transfer of the energy to the acceptor. In device assembly one protocol is that the sensitizing dye is absorbed into photoanode and donor dye is dissolved in the electrolyte as an energy relay [5]. Alternate method is that both dyes are co-adsorbed into the photoanode one by one or as a cocktail for in-situ FRET assembly.

For FRET to occur, donor molecule should be fluorescent and have more excitation energy than the acceptor molecule[6]. In this work an attempt has been made to enhance the efficiency of the DSSC using natural dye obtained from the leaves of red amaranth using Rhodamine B as the energy relay dye. Rhodamine B is a commercial dye which has been recently utilised in solar cell research though it has been widely used in photocatalytic studies. RhodamineB is cheap, stable and has an absorbance around 500nm which makes it a good candidate for solar cell applications. Here Rhodamine dye has been utilised as an energy donor to the natural dye in dye-dye FRET system in a liquid electrolyte DSSC. The hybrid system performs better than the individual dyes used as sensitizers supporting energy transfer, though the improvement is less significant in this configuration.

7.2 Materials and Methods

7.2.1 Materials

Natural dyes were prepared using red amaranth leaves following the procedure mentioned in our previous work[7]. Rhodamine B was purchased from Sigma-Aldrich and used without further purification. Ethanol, Distilled water (Millipore systems) were used as solvents.

7.2.2 DSSC Assembly

FTO conductive glass plates (7 Ω/square cm) were cleansed using soap solution, de-ionised water, acetone in an ultrasonic bath consecutively and dried in a hot air oven at 60°C. The TiO_2 thin film was obtained by coating the paste of TiO_2 powder (anatase, 25 nm) ethanol and TritonX -100 on the FTO glass plate. The TiO_2 deposited FTO glass plates were dried in oven overnight and calcined at 450^oC for 30 minutes in a furnace.The photoanodeswere taken out from the oven and area confinement of 0.25 cm^2 was done.The photoanodes were dipped in natural dye solution for 24 hours. The photoelectrodes were taken from dye solution, rinsed with methanol to remove impurities;air dried and dipped in Rhodamine b dye solution for another 24 hours. The counter electrode was prepared by electrodeposition of 4mM hexachloroplatinic acid (H_2PtCl_6) using cyclic voltammetry method. The electrolyte was prepared by mixing 0.04 M Iodine (I_2),0.1 M lithium iodide (LiI) in acetonitrile with 0.6M4-butyl methyl imidazolium iodide (BMII), 0.1 Mguanidiumthiocyanate (GuSCN) and 0.5 M tertiary butyl pyridine as additives. The prepared photoelectrode and platinum counter electrode were assembled to form a solar cell by sandwiching the redox electrolyte using binder clips.

7.2.3 Characterisation Techniques

The UV-vis spectrophotometer (T90, PGSTAT) was used to measure the nature of absorbance of the nanoparticles in the visible range of the solar spectrum. The photoluminescence (PL) measurements were conducted using PerkinElmer (LS 55) in the visible range.For measuring the performance of DSSC, current-voltage (I-V) characteristics were done using solar simulator

(Scientech) under 1 sun illumination (100mW/cm^2).The electrochemical impedance spectroscopic measurements were carried out using computer controlled potentiostat-galvanostat (SP150, Biologic) in the frequency range 1 mHz to 10MHz under illumination of 100mW/cm^2. The Flurocube-lifetime system (JOBIN-VYON) with pulsed diode excitation was used to measure lifetimes of the samples.

7.3. Result and Discussion

7.3.1 Cell characterisations of natural dyes

The J-V (current density-voltage) curves were obtained from natural dye sensitized DSSC and are shown in Fig. 7.1. The cell parameters obtained are tabulated and shown in Table 1. Chlorophyll dye (ethanol extracted) sensitized cell had an open circuit voltage of 0.582 V and short circuit current density of 1.31 mA/cm^2 compared to 0.486 V and 0.87 mA/cm^2 of betalain dye (water extracted).Chlorophyll based natural dye showed better efficiency of 0.53 % and fillfactor of 69.7 % compared to 0.23 % and 53.4 % of betalain based dye. This could be due to the stronger and broader absorbance of the chlorophyll dye in the visible region and its better attachment on to TiO_2 surface.

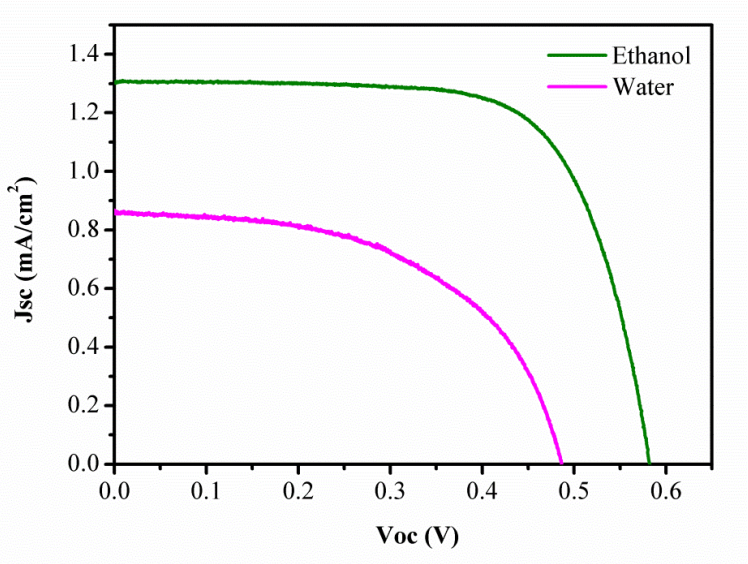

Fig. 7.1 Current-voltage characteristics of natural dye sensitized DSSC

Solvent	Jsc (mA/cm^2)	Voc (V)	FF(%)	η (%)
Water	0.87	0.486	53.4	0.23
Ethanol	1.31	0.582	69.7	0.53

Table 7. 1**.** Cell parameters of natural dye sensitized DSSC

The steady state I-V characteristics of DSSC provide the information about the performance parameters of the cell namely Jsc (short circuit current), Voc (open circuit voltage), FF (fill factor) and η (efficiency) but are unable to explain the individual processes behind it.EIS (electrochemical impedance spectroscopy) is a dynamic technique which has the ability to separate various complex processes occurring at the various interfaces of the DSSC. This method is employed to study the kinetics of electrochemical and photoelectrochemical processes in DSSC by measuring the current response to ac voltage as a function of frequency[8].

The Nyquist plot shown in Fig. 7.2a features three semicircles that are in order of decreasing frequency corresponding to counter electrode-electrolyte interface resistance (R_1), the electron transfer at the oxide/electrolyte interface (R_2) and Warburg resistance related to diffusion of redox couple (R_3). R_s is the sheet resistance of the FTO substrate. The first two semicircles correspond to high frequency and middle frequency regions and last semicircle corresponds to low frequency region[9]. The impedance of each interface is plotted after fitting the EIS data with software in terms of an equivalent circuit. EIS parameters are listed in Table 7.2.

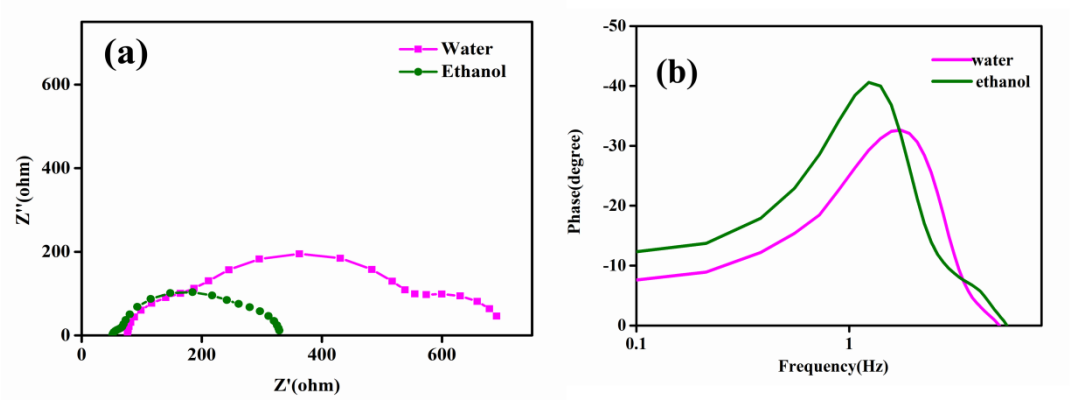

Fig.7.2 (a) Nyquist plot of betalain/chlorophyll sensitized DSSC and (b) bode phase plot

Solvent	$R_1(\Omega)$	$R_2(\Omega)$	$R_3(\Omega)$
Water (Red)	83	391	136
Ethanol (Green)	26	228	33

Table 7.2 EIS parameters of natural dye sensitized DSSC

The R_1, R_2 and R_3 values are different for the dyes which could be due to the difference in binding between the dye molecules and TiO_2.A higher value

of R_2 in both dyes indicates lower probability of back recombination of electrons which is a decisive factor in determining cell efficiency. The high value of R_1 and R_3 can cause a decrease in J_{sc} leading to lesser efficiency. Here, betalain extracted from water shows high R_1 and R_3 values. .

The Impedance curves (Fig.7.2a) are in agreement with the efficiencies obtained from the I-V curves (Fig.7.1).Fig.7.2bshows the bode phase plot of the cell sensitized with dye extracted with water and ethanol in the low frequency range (0.1-10 Hz) corresponding to effective lifetimes of electrons on the surface of TiO_2photoanode. The peak frequencies obtained from the graph are inversely proportional to lifetimes of electrons[10] . The peak frequency of greendye extracted from ethanol is 1.26 Hz and that of water extracted red dye is 1.70 Hz. This leads to better electron lifetime of ethanol extracted chlorophyll dye compared to water extracted betalain dye leading to better efficiency of DSSC. The bode plot results are in agreement with the J-V experimental data.

7.3.2 FRET parameters of Hybrid Dye system

To improve the efficiency of the natural dye sensitized solar cell, a commercial dye with good stability and quantum yield was used as a second sensitizer in this work with structure shown in Fig. 7.3.

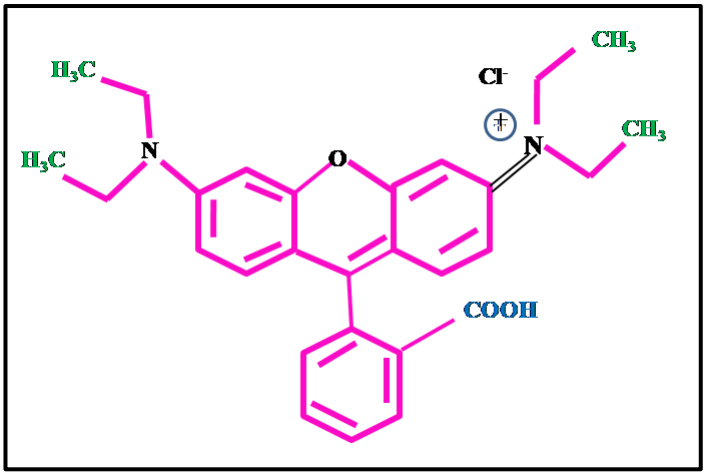

Fig.7.3 Molecular structure of Rhodamine B

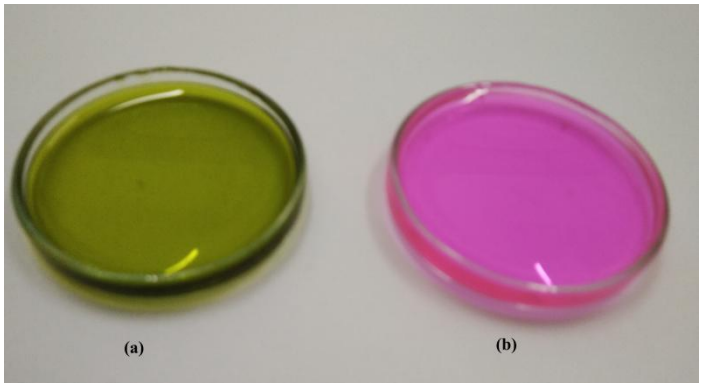

Fig. 7.4 (a) Green dye (b) Rhodamine B dye in ethanol

The two dyes used in hybrid cell namely green dye chlorophyll and Rhodamine has been presented in Fig 7.4. The spectral overlap between the emission of Rhodamine B and absorption of green dye is given by Fig.7.5.

Co-sensitization of TiO_2 photoanode by two dyes enhances the absorption bandwidth by broadening the spectral window. Rhodamine B was used to absorb wavelengths in 550-620 nm regions which were not covered by the green dye.

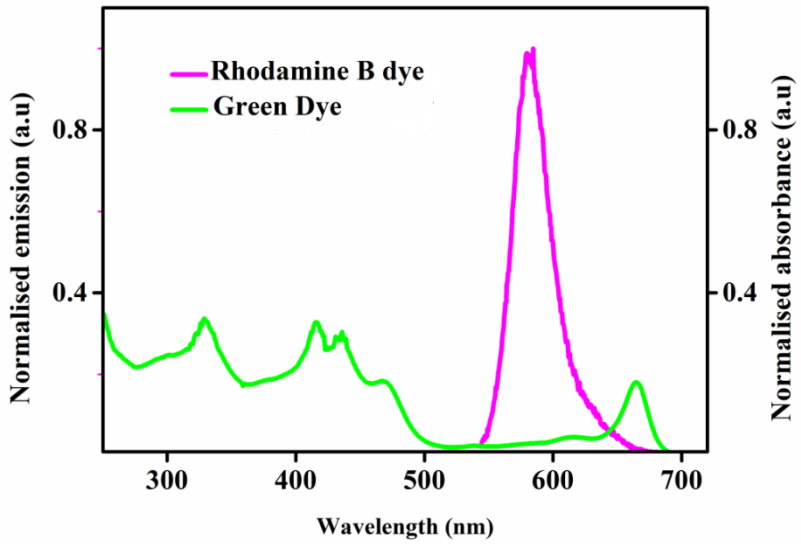

Fig.7.5 The spectral overlap between emission of Rhodamine (Rd) and absorption of Green (G) dye

From the graph, overlap integral was calculated using Flurotool free software and the Förster radius R_0 is calculated to be 3.38 nm using calculations based on previous reports [11] and presented in Table 7.3.It is seen that R_0 lies between 1-10 nm which is the range of FRET mechanism[12].

Dye Solution	Overlap Integral J (nm^4/mol.cm)	R_0 (A^0)	Concentration (Mol/L)
Donor-Acceptor	1.464×10^{14}	33.88	3×10^{-4}

Table 7.3 FRET parameters of Rhodamine-Green dye combination

The quenching studies conducted on Rhodamine by adding small amounts of green dye are shown in Fig.7.6 It is seen that Rhodamine dye quenches as

the concentration of the green dye goes on increasing suggesting energy transfer between the dyes.

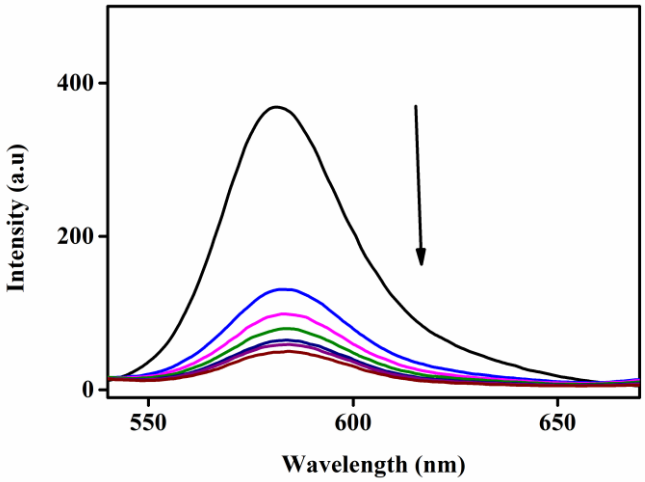

Fig.7.6 PL quenching of Rhodamine B with increasing amounts of green dye

To confirm the energy transfer occurring between Rhodamine B and green dye lifetime decay measurements using time-corelated single photon counting (TCSPC) method was conducted. The experiment was performed at a pulsed excitation of 460 nm and the decay curves were fitted with a three exponential function $I(t) = \sum_{i=1}^{3} \alpha_i \, e^{\frac{-t}{\alpha_i}}$ as shown in Fig.7.7.

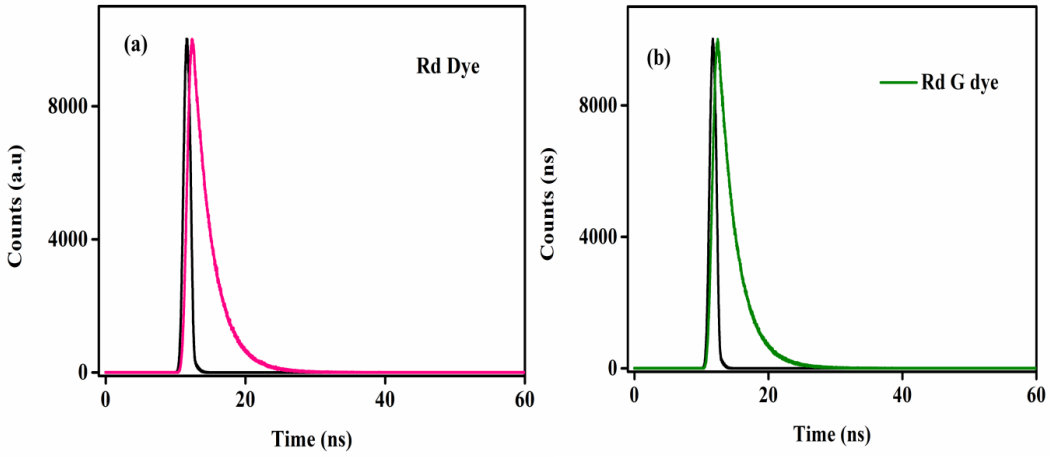

Fig. 7.7 Lifetime measurements (a) Rd Dye (b) Rd G dye

The lifetime of the hybrid system of Rhodamine-Green dye is 2.3 ns, whereas the Rhodamine dye alone is 2.8 ns as shown in Table 3.The shortening of lifetime is an indicative of FRET occurring between the donor-acceptor pair in this case. The energy transfer efficiency is calculated using the following equation

$$E_T = \frac{\tau_{DA}}{\tau_D} \qquad (1)$$

Donor-Acceptor Concentration	Donor Lifetime τ_D(ns)	FRET pair Lifetime τ_{DA}	Energy Transfer efficiency,E_T(%)
3×10^{-4}: 3×10^{-4}	2.8	2.3	17.85

Table7.4 Lifetime data of the donor and FRET pair

7.3.2 Cell characterisations of Hybrid system

In order to test the improvement in solar cell efficiency using FRET system the J-V curves were drawn from the data obtained from solar cell measurements and are presented in Fig. 7.8 a and b.

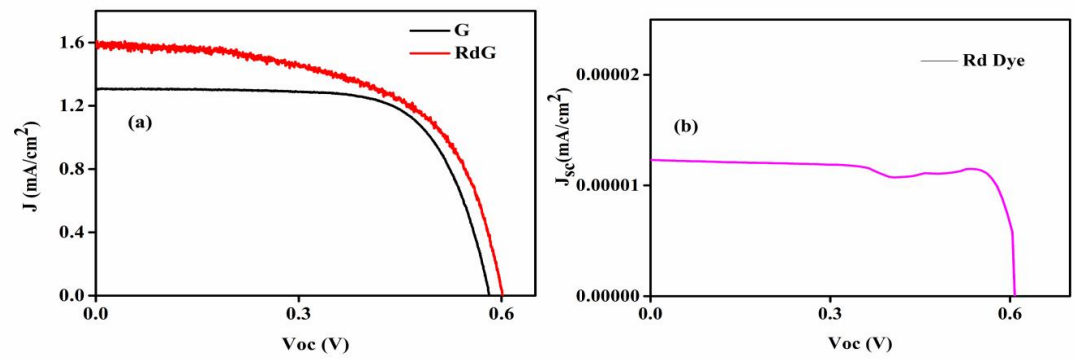

Fig.7.8 J-V curves of (a) FRET pair (RdG) and GreenDye(G)

(b) RhodamineB (Rd)

From the J-V curves shown in Fig.7.8 it is seen that there is a marginal increase in current and open circuit voltage of the hybrid cell. The parameters obtained from I-V measurements of the three cells have been presented in Table 7.5 for comparison.

Name of sensitizer	J_{sc} (mA/cm^2)	Voc (V)	Fill Factor (FF)	Efficiency (%)
Green Dye	1.31	0.582	69.7	0.53
Rhodamine b Dye	1.232×10^{-5}	0.579	53.6	5.6×10^{-3}
Rd-G Hybrid	1.58	0.601	60.1	0.571

Table 7.5 Comparison of solar cell parameters of various configurations

From the Table 7.5 it is seen that Rhodamine B has a low efficiency of 0.0056% which matches with the previous reports[13]. As Rhodamine dye is not a good sensitizer, we can claim that the improvement in the hybrid cell is not due to the combined sensitization of the individual dyes, but due to energy transfer via FRET mechanism. Here the green dye was attached directly to the photoanode surface and then Rhodamine dye was used as second layer to achieve better output in FRET system.The Rhodamine dye acted as an energy donor to the green chlorophyll dye in the hybrid system. The current density increases from 1.31 mA/cm^2 to 1.58 mA/cm^2 showing an enhancement of 20.6%. Similarly open circuit voltage increases from 0.582 V to 0.601 V showing an enhancement of 3.2 %. More enhancements in J_{sc} compared to Voc may be due to increased number of excited states in green dye due to energy transfer from Rhodamine dye leading to better sensitization of the TiO_2 photoanode. In order to understand the charge transfer dynamics the EIS and Bode plot curves are presented in Fig. 7.9.

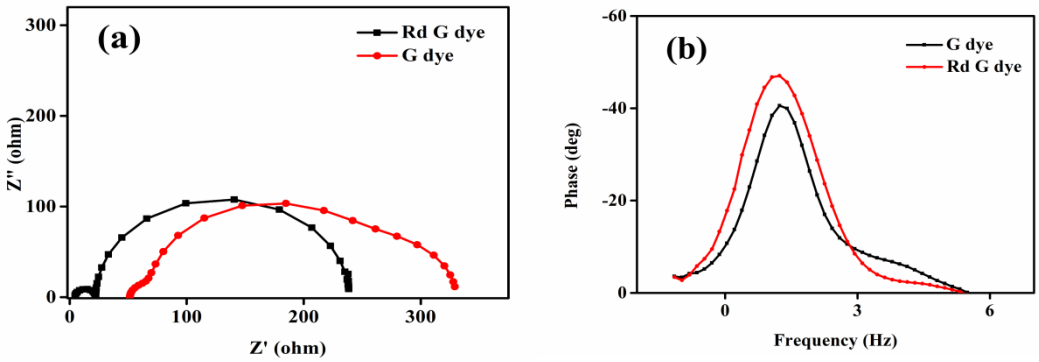

Fig 7.9 Hybrid cell (a) Nyquist plot (b) Bode plot

Name of Dye	$R_1(\Omega)$	$R_2(\Omega)$	$R_3(\Omega)$
Green (G)	26.0	228	33.0
FRET pair (Rd-G)	22.2	211	4.8

Table 7.6 EIS parameters of Hybrid Cell

From the Nyquist plot it is seen that the first and second curves show similar values showing small changes but there is difference in low frequency end representing Warburg diffusion corresponding to charge kinetics at the electrolyte. The decrease in value of R_3 in Hybrid cell could be due to the decrease in viscosity of the electrolyte due to the presence of two dyes. A less viscous electrolyte causes increase in diffusion coefficient leading to increase in electron diffusion length indicating an increase in J_{sc} [14]. The bode plots which are indicative of the electron lifetime shows frequency values of 1.18 Hz and 1.26 Hz of the FRET cell and green dye respectively. As electron lifetime is inverse of frequency, these values suggest a better electron lifetime for the Hybrid cell. The sequential adsorption of the green dye and then Rhodamine dye creates a layer on the TiO_2 photoanode protecting it from the liquid electrolyte, thus reducing electron hole back recombination leading to increase in electron lifetime of the Hybrid cell [15]. Though the bode plots are in agreement with J-V curves showing better electron lifetime for Hybrid cell , the difference is very small justifying less increment in cell efficiency.

Conclusion:

Two natural dyes from the red amaranth leaf, betalain (red) and chlorophyll (green) were used as photosensitizers for DSSC. The chlorophyll dye showed a better efficiency of 0.53 % with a fill factor of 69.7 % compared to betalain dye with an efficiency of 0.23 % and a fill factor of 53.4 %. The V_{oc} of 0.582 V of chlorophyll dye is comparable to the V_{oc} of high efficiency chlorophyll dyes reported in literature. The sensitization of TiO_2surface can be improved by replacing alkyl groups by carboxylic groups in chlorophyll dye. Similarly the V_{oc} of betalain dye of 0.486 V is also comparable to betalain sensitized DSSC reported in literature. To further improve the efficiency of the solar cell, chlorophyll or green dye was co-sensitized with a commercial dye named Rhodamine B. It is seen that the Rhodamine B inspite of being a poor sensitizer improves the efficiency of the cell by energy transfer mechanism known as FRET. The Rhodamine B acts as donor and green dye acts as acceptor in the FRET systems. The FRET distance is calculated to be 3.38 nm and energy transfer efficiency is about 17.85 %. Though the hybrid system utilised here is novel, it is seen that the enhancement in solar cell efficiency is about 7% which needs to be improved by changes in device architecture and trying various combinations of cocktail dyes with Rhodamine B and other commercial dyes.

References

[1] M.G. Brian O' Regan, A low -cost ,high-efficiency solar cell based on dye-sensitized colloidal TiO2 films, Nature. 353 (1991) 737–740.

[2] M.K. Nazeeruddin, E. Baranoff, M. Grätzel, Dye-sensitized solar cells: A brief overview, Sol. Energy. 85 (2011) 1172–1178.

[3] M.R. Narayan, Review : Dye sensitized solar cells based on natural photosensitizers, Renew. Sustain. Energy Rev. 16 (2012) 208–215.

[4] B.E. Hardin, E.T. Hoke, P.B. Armstrong, J. Yum, P. Comte, M.D. Mcgehee, K. Nazeeruddin, M. Gra, J.M.J. Fre, Increased light harvesting in dye-sensitized solar cells with energy relay dyes, 3 (2009).

[5] N.D. Eisenmenger, K.T. Delaney, V. Ganesan, G.H. Fredrickson, M.L. Chabinyc, Improving energy relay dyes for dye sensitized solar cells by increasing donor homotransfer, J. Phys. Chem. C. 118 (2014) 14098–14106.

[6] D.S. Cells, J.I. Basham, G.K. Mor, C.A. Grimes, Förster Resonance Energy Transfer in Dye-Sensitized Solar Cells, ACS Nano. 4 (2010) 1253–1258.

[7] R. Ramanarayanan, P. Nijisha, C. V Niveditha, S. Sindhu, Natural dyes from red amaranth leaves as light-harvesting pigments for dye-sensitized solar cells, Mater. Res. Bull. 90 (2017) 156–161.

[8] M.G. Wang, Qing, Jacques-E. Moser, Electrochemical Impedance Spectroscopic Analysis of Dye-Sensitized Solar Cells, 109 (2005) 14945–14953.

[9] B. Liu, W. Li, B. Wang, X. Li, Q. Liu, Y. Naruta, W. Zhu, Influence of different anchoring groups in indoline dyes for dye-sensitized solar cells: Electron injection, impedance and charge recombination, J. Power Sources. 234 (2013) 139–146.

[10] J. Bisquert, A. Fabregat-santiago, Francisco, Ivan Mora-Sero , Germa

Garcia-Belmonte, S. Gimenez, Electron Lifetime in Dye-Sensitized Solar Cells: Theory and Interpretation of Measurements, J. Phys. Chem. C. 113 (2009) 17278–17290.

[11] S. Kundu, A. Patra, Nanoscale Strategies for Light Harvesting, Chem. Rev. 117 (2017) 712−757.

[12] M. Lunz, A.L. Bradley, V.A. Gerard, S.J. Byrne, Y.K. Gun, V. Lesnyak, N. Gaponik, Concentration dependence of Förster resonant energy transfer between donor and acceptor nanocrystal quantum dot layers : Effect of donor-donor interactions, Phys. Rev. B. 83 (2011) 1–10.

[13] H. Setyawati, A. Purwaningsih, H. Darmokoesoemo, F. Rochman, H. Setyawati, A. Purwaningsih, F. Rochman, A.J. Permana, Potential Complex of Rhodamine B and Copper (II) for Dye Sensitizer on Solar Cell, 070004 (2016) 1–7.

[14] Y. Bai, Y. Cao, J. Zhang, M. Wang, R. Li, P. Wang, S.M. Zakeeruddin, M. Grätzel, High-performance dye-sensitized solar cells based on solvent-free electrolytes produced from eutectic melts, Nat. Mater. 7 (2008) 626–630.

[15] V.A. Online, Y. Lin, J. Chen, P. Hsiao, Y. Tung, C. Chang, C. Chen, E fficiency improvement of dye-sensitized solar cells by in situ fluorescence resonance energy, J. Mater. Chem. A. (2017) 9081–9089.

CHAPTER 8

Summary and Scope of Future Work

Summary and Scope of Future Work

The first chapter of the thesis highlights the importance of solar energy for the benefit of human race. It provides the historical overview of the generations of solar cells and working principle of DSSC. Further it elucidates various enhancement mechanisms in DSSC and discusses the principle and application of FRET in detail. Finally the scope of the thesis and outline of the work is described. The chapter two discusses the principles and methodologies involved in this doctoral work for characterising the materials and devices used in this thesis.

The third chapter describes in detail the materials synthesized via novel green protocol for this doctoral work. The supporting characterisations to properly describe the property and nature of the materials synthesized were conducted in detail. The leaf extract of guava in water medium was used as reducing agent to synthesize silver and gold nanoparticles. The silver nanoparticles were in the size range of 10-30 nm and spherical in shape. The gold nanoparticles of red and black colour obtained were of three different sizes upon varying the concentration of the extract. The formation of aggregate structures of black gold were explained by a model proposed based on the hydrogen bonding due to the excess hydroxyl groups present in the extract. The natural dyes extracted from leaves of red amaranth were betalain (in water) which is red in colour and chlorophyll (in ethanol) which is green in colour were confirmed from absorbance and FTIR measurements.

The fourth chapter deals with Ag incorporated TiO_2photoanodes used to improve efficiency in DSSC. The incorporation of silver nanoparticles

improves performance by SPR effect, lowering of bandgap and reduced recombination of electron –hole pairs. In this work we have shown that the both electron transfer and energy transfer mechanisms act complementary to each other. Here FRET and SPR act complementary to each other in determining the efficiency of solar cell. When FRET increases efficiency decreases and vice versa. The optimisation was conducted through controlling the dip coating time of bare TiO_2photoanodes in Ag colloid, carried out at 30,60 and 120 minutes. It was found out that 30 minutes dipping with Ag content of 1.6 % gives the best performance with 6.69% efficiency. With increasing dipping time Ag content increases and performance diminishes as FRET dominates over plasmonic enhancement leading to decrease in efficiency.

In the fifth chapter the spectroscopic studies of gold nanoparticles and MB dye was studied and energy transfer mechanism between Dye and Au nanoparticles observed.The role of shape/size of gold nanoparticles in influencing the energy transfer was investigated. It was observed that gold nanoaggregates show better energy transfer and hence better photodegradation of the dye. In this dye-metal nanoparticle hybrid system FRET acts as a facilitator in direct photocatalysis of dye by metal nanoparticles.

The sixth chapter deals with the efficiency improvement in CdSe sensitized solar cell due to the introduction of GQD as Donor in the Hybrid cell structure. Various combinations of CdSe-GQD were studied and it was found that CdSe as the first sensitizing layer with GQD drop casted on it gives the best result with an efficiency of 0.28%. The enhancement due to FRET was confirmed through PL quenching and lifetime measurements.

The seventh chapter deals with the photoelectrochemical studies of a hybrid cell having Rhodamine B-and natural green dye combination. The hybrid cell shows enhancement of solar cell efficiency of pure natural dye supported by FRET mechanism. Here the enhancement is about 7% as the energy transfer is also less of about 17 %. However this combination of dye-dye cell is novel and can be further improved by introducing different cell architecture and various combinations of dyes.

SCOPE OF FUTURE WORK

- Exploiting metal nanoparticle Ag and Ag-TiO_2 composite for various applications like photocatalytic degradation of dyes and water purification.
- Exploring Au/Ag counters for DSSC applications
- Using green synthesized Ag-Au alloys/bimetallic nanoparticles for various light harvesting applications.
- Improving the efficiency of QD solar cell by different combinations of QD-Dye systems
- Using different combinations of natural and low cost commercial dyes for enhanced solar to light conversion efficiency in DSSC.

Materials Research Bulletin 114 (2019) 28–36

Contents lists available at ScienceDirect

Materials Research Bulletin

journal homepage: www.elsevier.com/locate/matresbu

The deterministic role of resonance energy transfer in the performance of bio-inspired colloidal silver nanoparticles incorporated dye sensitized solar cells

Rajita Ramanarayanan, Niveditha Chokiveetil, Nijisha Pullanjiyot, Bhabhina Ninnora Meethal, Sindhu Swaminathan*

Department of Nanoscience & Technology, University of Calicut, Kerala, 673635, India

ARTICLE INFO

Keywords:
FRET
LSPR
DSSC
Ag nanoparticles
Green synthesis
Photoanode

ABSTRACT

The crucial role of non-radiative energy transfer mechanism, Förster Resonance Energy Transfer (FRET), competing with Localized Surface Plasmon Resonance (LSPR) mediated charge transfer in influencing the performance efficiency of dye sensitized solar cell has been discussed in this investigation. LSPR enhances the light harvesting efficiency of the dye but FRET (TiO_2 - Ag) acts as a loss mechanism in the cell performance. Bio-inspired silver colloids were incorporated into the TiO_2 photoanode with dip coating for 30, 60 and 120 min. The 30 min dipped Ag-TiO_2 photoanode solar cell showed an improved efficiency of 6.69% as compared to 4.85% of bare TiO_2 photoanode. Higher dipping time reduces efficiency of the cell by dominating FRET over LSPR effects. The magnitude TiO_2-Ag, Ag-dye and dye-TiO_2 interfaces can be controlled by changing the dipping time to get the benefits of LSPR and to revoke FRET in a DSSC structure for high performance efficiency.

1. Introduction

The ultimate goal of any solar cell technology is to achieve cost-effective power generation with optimum efficiency to meet the growing demands of the society. Nanostructure-semiconductor based solar cells are anticipated to play a major role in providing clean and green energy in future [1]. DSSC (Dye Sensitized Solar Cells) assume a special place in this regard fulfilling the above requirements with a unique feature of charge generation, charge transport and charge collection by different components of the cell. Hence the focus shifts to optimised combination of materials and methods to improve individual device parameters associated with the solar cell like photoanode, dye, counter electrode, electrolyte so as to enhance the device efficiency [2–7]. Photoanode is one of the key components where research is being done to improve the photocurrent and hence efficiency of the solar cell. One of the prominent strategies is the integration of metal nanostructures to improve the overall output. Metal nanoparticles by virtue of their unique physico-chemical properties have opened doors of various possibilities for metal-semiconductor hybrid structures in photovoltaic cells, catalysis and sensing applications [8,9].

Metal nanoparticles like silver have been extensively used in photovoltaic because of its relative stability and strong absorbance in visible region. The electromagnetic radiation causes collective oscillations of the conduction band electrons with a resonant frequency termed as Local Surface Plasmon Resonance (LSPR). The LSPR imparts significant influence on the photophysical properties on the semiconductors/dyes in the close vicinity of the metal nanoparticles. The use of noble metal incorporated photoanodes has shown remarkable efficiencies mainly attributed to dye absorption enhancement due to SPR (surface plasmon resonance) [10,11]. Sardar *et al* reported silver modified photoanode and counter electrode with increased photovoltage leading to high efficiencies at about 8.02% [12]. Most of the previously reported methods [12] synthesize Ag-TiO_2 by addition of silver precursor to TiO_2 along with reducing agent followed by a lab method to form Ag-TiO_2 nanocomposite powder which is then coated on FTO/ITO to form photoanode or mix Ag NPs to TiO_2 followed by stirring/ball milling for long hours to form Ag-TiO_2 nanocomposite [13,14]. This investigation uses direct dipping of TiO_2 photoanode in Ag colloid to form Ag-TiO_2 photoanode via dip coating method without involving any tedious physical/chemical processes. Silver incorporated TiO_2 (Ag-TiO_2) photoanode in this work distinguishes itself in terms of novelty of design, ease of fabrication and competitive efficiencies. However inspite of promising results noble metal incorporation in photoanodes has failed to reach the desired heights in terms of solar cell

* Corresponding author.
E-mail address: sindhus@uoc.ac.in (S. Swaminathan).

https://doi.org/10.1016/j.materresbull.2019.02.017
Received 3 November 2018; Received in revised form 30 January 2019; Accepted 11 February 2019
Available online 11 February 2019
0025-5408/

efficiency to achieve commercial success. A detailed study on the plausible interactions involving energy and electron transfer is required to evaluate the energy harvesting mechanisms occurring in the DSSC. Recently Nbelayim et al have reported that charge recombination is one of the major factors for not achieving very high efficiency in Ag-TiO_2 solar cells [15]. Here we are exploring the role of a non-radiative energy transfer FRET (Förster Resonance Energy Transfer) a relatively less explored phenomenon, playing a decisive role in determining the efficiencies of hybrid solar cells.

In the present work silver nanoparticles synthesized through green method with leaf extract of guava (*Pisidiumguajava*) used to enhance photocurrent and hence efficiency of DSSC. Though silver synthesis using guava leaf extract has been previously reported [16], this study assumes significance because of its fast synthesis and very high stability up to eight months. Further it is carried out at room temperature and is completely green implying that no other reagent is added apart from precursor solution and aqueous guava leaf extract.

Ag-TiO_2 photoanode for this study was obtained by immersing bare TiO_2 photoanode in silver nanoparticle (Ag NP) colloid. The optimized device performance was analysed using data obtained from current-voltage (I-V) measurements. Various characterization techniques were adopted to elucidate the enhancement and quenching mechanisms taking place at the semiconductor-Ag-dye interface and its role in determining the overall efficiency of the solar cell.

2. Materials and methods

2.1. Materials

TiO_2 nanoparticles (P25), Fluorine doped tin oxide (FTO-7Ω/Sqcm), hexachloroplatinic acid (H_2PtCl_6) and potassium iodide (KI) (99.5%), N719 dye were obtained from Sigma-Aldrich and iodine (I_2) from MERCK. Distilled water (Millipore System), Ethanol and Methanol (≥ 99% Sigma Aldrich) were used as solvents.

2.2. Synthesis of silver nanoparticles

The fresh mature leaves of guava were washed, cut into small pieces and air-dried for some time to remove excess of water. Leaf extract was prepared by boiling and stirring the leaves in distilled water following the same procedure as reported in our previous work [17]. 20 mL of 1 mM $AgNO_3$ (Merck) was used as precursor solution for nanoparticle synthesis. For synthesis of silver nanoparticles 1 mL of the extract was added to 20 mL of 1 mM of $AgNO_3$ solution and stirred using pipette to ensure uniform mixing. The colour change of the silver salt solution to pale yellow and then yellowish brown implies the formation of silver nanoparticles. The change in colour is completed within 4 min showcasing a very fast reduction mechanism as depicted in Fig. 1.

2.3. DSSC assembly

FTO conductive glass plates (resistance 7 Ω/cm^2) were first cleaned with soap solution and rinsed with de-ionised water and acetone for 10 min in an ultrasonic bath. The TiO_2 paste was prepared by blending commercial TiO_2 powder (anatase, 25 nm) with ethanol and one drop of Triton X -100. The resultant paste was deposited on the FTO glass plate using doctor blading technique. The air dried TiO_2 deposited FTO glass plates were calcined at 450 °C for 30 min in a muffle furnace. On cooling, the area confinement of 0.25 cm^2 was done and dipped in silver nanoparticle colloid for 30 min (three dipping time chosen are 30, 60 and 120 min). Finally dye was attached to TiO_2 surface by dipping the electrodes in dye solution for 24 h. The photoelectrodes were taken from dye solution, rinsed with methanol to remove impurities and air dried for further use. The counter electrode was prepared by electrodepositing 4 mM hexachloroplatinic acid (H_2PtCl_6) with a scan rate of 20 mV/sec for four cycles. The electrolyte was prepared by mixing

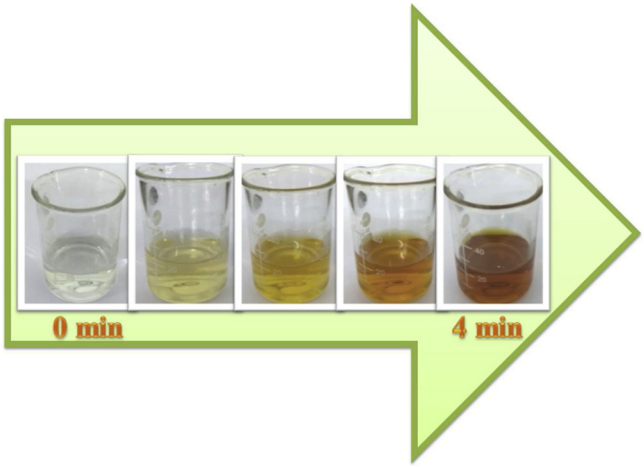

Fig. 1. Colour change chart illustrating formation of Ag NPs.

0.6 M 4-butyl methyl imidazolium iodide (BMII), 0.04 M Iodine (I_2), 0.1 M lithium iodide (LiI), 0.1 M guanidiumthiocyanate (GuSCN) and 0.5 M tertiary butyl pyridine in acetonitrile. The TiO_2 electrode and electrodeposited Pt counter electrode were assembled to form a solar cell by sandwiching the redox electrolyte using binder clips.

2.4. Optical and electric measurements

The UV–vis spectrophotometer (T90) was used to measure the nature of absorbance of the nanoparticles in the visible range of the solar spectrum. X –ray diffraction (XRD) measurements were performed using Rigaku Miniplex–X Ray Diffractometer with monochromatic Cu-Kα radiation (λ = 1.54 Å), scanned in the 2θ range of 30° to 80°. The size of the synthesized nanoparticles was determined by transmission electron microscopy (TEM) Jeol/ JEM 2100 using LaB6 source operated at 200 kV. The photoluminescence (PL) measurements were conducted using PerkinElmer (LS 55) in the visible range. For measuring the performance of DSSC, current-voltage (I–V) characteristics were done using solar simulator (Scientech) under 1 sun illumination (100 mW/cm^2). The electrochemical impedance spectroscopic measurements were carried out using computer controlled electrochemical interface (SP150, Biologic) in the frequency range 1 mHz to 10 MHz under illumination of 100 mW/cm^2. Mott-Schottky measurements were conducted with 0.1 M Na_2SO_4 under the bias voltage of $^{-}$0.9 V to $^{-}$0.5 V in the frequency range of 1 KHz to 1 Hz. The Flurocube-lifetime system (JOBIN-VYON) with pulsed diode excitation was used to measure lifetimes of the samples.

3. Results and discussion

The XRD pattern of the synthesized silver nanoparticles using guava leaf extract is recorded and the spectrum is shown in Fig. 2.

The peaks are broadened indicating smaller crystallite size of the nanoparticles. The peaks are indexed as (111), (200), (220), (311) planes of FCC silver by comparing with the JCPDS data. Apart from these peaks, an additional unassigned peak around 2θ value of 46° (peak with asterisk) is also seen. This peak may be due to the formation of bio-organic components/metallo-proteins that are present in the leaf extract. Similar findings are reported previously [18]. The crystallite size obtained from Scherer formula is 12.6 nm.

TEM analysis of the Ag NPs indicates stable, well dispersed, near spherical nanoparticles as shown in Fig. 3(a). The size distribution graph obtained from TEM (Fig. 3(b)) shows that maximum no of particles are in the range 15–25 nm. The silver nanoparticles in this range are reported to show hot electron generation, a major mechanism involved in carrier generation enhancement in solar cells [19,20].

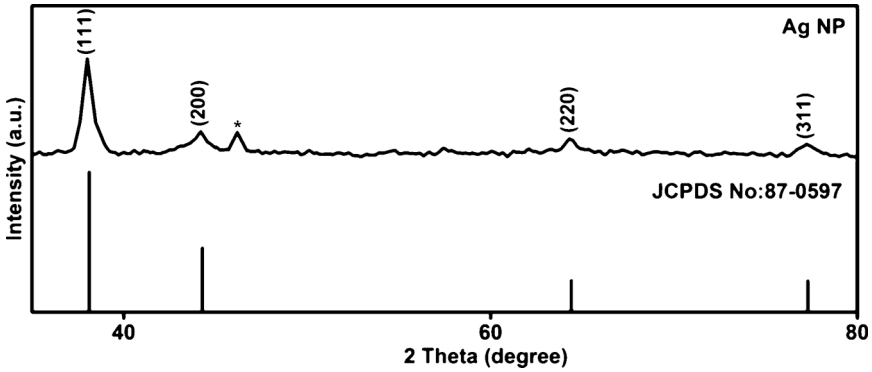

Fig. 2. XRD spectrum of Ag NPs with JCPDS data.

The HRTEM image showing lattice spacing is presented in Fig. 4(a). The obtained fringe width 0.23 nm corresponds to (111) planes of silver (JCPDS-87-0597) indicating the crystalline nature of nanoparticles. The selected-area electron diffraction (SAED) pattern of the synthesized sample is shown in Fig. 4(b). The concentric diffraction rings containing bright spots correspond to the presence of (111), (200), (220), (311), and (222) planes of the face-centered cubic (FCC) silver nanoparticles.

The UV–vis measurements (Fig. 5a) show the absorbance peak at about 425 nm indicating the formation of silver nanoparticles. Guava leaf broth proves to be a good reducing agent in terms of synthesis rate with maximum conversion occurring in the first 4 min. Plasmonic nanostructures support the formation of resonant surface plasmons (SPs) in response to a photon flux localising electromagnetic (EM) energy close to their surfaces. The EM field due to surface plasmon resonance enhances the optical absorption of the dye [21]. The absorption enhancement of N719 dye on successive addition of silver nanoparticle solution in the range 300–600 nm has been depicted in Fig. 5(b). N719 has absorption peaks at 374 nm and 504 nm which at first increase on addition of Ag NP and finally broadens leading to a panchromatic sensitization in the visible region. The increase in absorption coefficient of the dye due to LSPR of the Ag nanoparticles paves way for enhanced photogeneration of electrons leading to improved efficiency of solar cells.

The SEM image of Ag-TiO_2 thin film is shown in Fig. 6a. The bright spots in the SEM image indicate the presence of silver nanoparticles distributed evenly on the TiO_2 surface [22]. The elemental analysis of silver modified TiO_2photoanode was determined by conducting EDAX (Energy Dispersive X-Ray Analysis) analysis of the Ag-TiO_2 thin film. The analysis shows that 1.61 wt% Ag is present in the photoanode material as shown in the Fig. 6(b). The deposition of silver nanoparticles by dip coating method in this report matches with the amount of direct deposition of silver on TiO_2 photoanode by other methods as reported previously [14].

The Tauc plot (Fig. 7(a) and (b)) was drawn to calculate the bandgap energy of sintered Ag-TiO_2 and bare TiO_2 powders using UV–vis Spectrophotometer. The E_g values are 3.3 eV for bare TiO_2 and 3.1 eV for Ag-TiO_2 showing direct indication of bandgap narrowing due to the presence of metal nanoparticles in TiO_2. This bandgap narrowing is due to the downward shift of conduction band and upward shift of valence band due to the presence of large number of free electrons by virtue of Ag NPs. Thus bandgap reduction shifts the optical absorbance towards the visible region acting favourably towards harnessing the solar spectrum leading to better light to energy conversion in solar cells [23,24].

The Mott-Schottky (MS) plot of the two photoanodes namely TiO_2 and Ag-TiO_2 has been displayed in Fig. 8 (a) and (b). The positive slopes of both photoanodes establish the expected n-type semiconductor characteristics. The flatband potential (E_{fb}) is obtained by extrapolating capacitance ($1/Cs^2$) to zero. The negative shift of flatband potential of Ag-TiO_2 with respect to TiO_2 is clearly observed from the graph suggesting increased carrier concentration leading to larger photocurrent generation [25].

The XPS studies are conducted on Ag-TiO_2 30 and Ag-TiO_2 120 to analyse the chemical composition and chemical states of Ag and Ti elements and the spectra are shown in Fig. 9a and b.

Fig. 9(a) shows the Ag $3d_{5/2}$ and $3d_{3/2}$ peaks appearing at binding energies 367.6 eV and 373.6 eV of Ag-TiO_2-30 indicating that the silver nanoparticles are not oxidised. However the Ag-TiO_2-120 sample shows Ag 3d peaks shifting to lower binding energies at 366.1 eV and 372.1 eV indicative of silver oxidation. The Ti $2p_{3/2}$ and $2p_{1/2}$ peaks of Ag-TiO_2-30 and Ag-TiO_2-120 do not show variation in binding energy and are observed respectively at 458.6 eV and 464.1 eV indicating the presence of Ti atoms in oxidation state IV [10].

Table 1 shows the surface atomic concentration of Ti, O and Ag elements in Ag-TiO_2 -30 and Ag-TiO_2-120 samples. The increase in Ag concentration for Ag-TiO_2-120 is due to increased dipping time of the respective photoanode in Ag colloid.

The various device parameters like short circuit current density

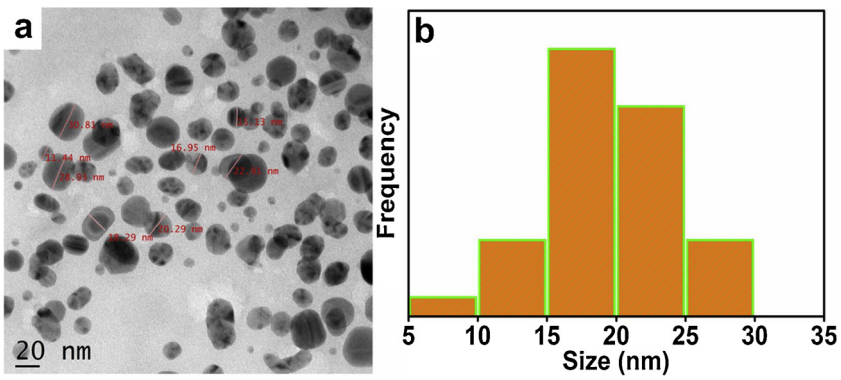

Fig. 3. TEM (a) image (b) size distribution graph of the synthesized Ag NPs.

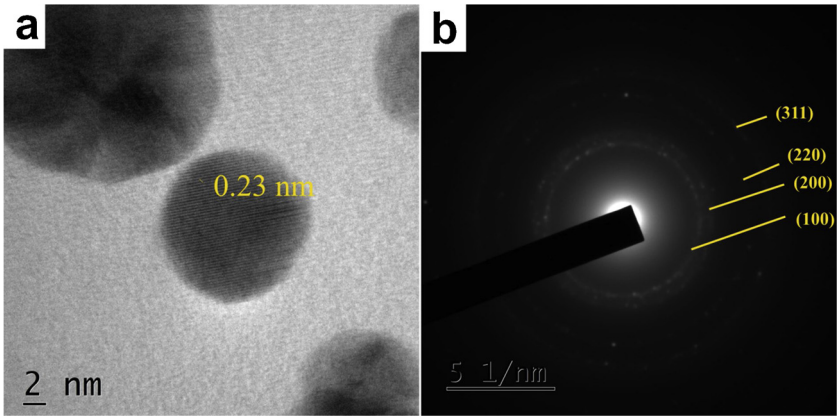

Fig. 4. a) HRTEM image showing lattice fringes (b) SAED pattern.

(J_{sc}), open circuit voltage (Voc), fill factor (FF) and efficiency (ŋ) of Ag-TiO_2 photoanodeand bare TiO_2 was studied for device performance in comparison to bare TiO_2 as presented in Table 1. The current voltage characteristics of the cell with bare TiO_2 and Ag-TiO_2 with different dipping time, such as 30, 60 and 120 min, are given in Fig. 10a. Fig. 10b depicts the Nyquist plot corresponding to the cell with bare TiO_2 and Ag-TiO_2 with various dipping times. The solar cell parameters are given in Table 2.

In the case of Ag-TiO_2 photoanode the open circuit voltage (V_{oc}) decreases slightly as compared to bare TiO_2. The V_{oc} is proportional to the difference between Fermi level of TiO_2 and Nernst potential of iodine/iodide electrolyte in a solar cell. The gap between the newly formed Fermi level of Ag-TiO_2 and redox potential of electrolyte is smaller by the shifting of the conduction band due to the adsorption of silver nanoaprticles. The V_{oc} is seen to decrease for silver incorporated photoanodes Ag-TiO_2-30, Ag-TiO_2-60 and Ag-TiO_2-120 from 0.737 V to 0.707 V. This finding is consistent with the previous reports of decrease in V_{oc} due to incorporation of noble metals in TiO_2 [26–28]. The photocurrent density increases from 11.69 in bare TiO_2 to 13.33 mA/cm^2 in Ag-TiO_2-30 photoanode. The increase in optical absorption by dye due to SPR of silver nanoparticle, reduced electron hole recombination losses and narrowing of the band gap are seem to be the primary reasons for the boosted current density observed in Ag-TiO_2-30 photoanode solar cell. Further the presence of large number of hydroxyl groups in the leaf extract of guava corresponding to gallic acid, quercetin [29] etc. (Fig. S1 in Supporting information (SI)) presents as capping agent for Ag NP contribute to its better attachment with the dye thus positively affecting the efficiency of the solar cell [30]. However the increasing trend in current density is not followed in Ag-TiO_2-60 and Ag-TiO_2-120 photoanodes. This trend of decrease in current density after an optimum concentration of Ag NPs has been observed in previous studies [15] indicating the role of other effects which compete with LSPR. The current density of a solar cell depends on good light absorbance for generation of charge carriers as well as their efficient injection and transport in the photoanode. Though Ag-TiO_2-60, Ag-TiO_2-120 photoanodes might have increased light absorbance with increase in Ag concentration but the key role of charge injection and transport leads to improved performance of Ag-TiO_2-30. The decrease in dye/TiO_2 interface and other loss mechanisms due to energy transfer are seem to be the reasons behind the decrease in net electron injection/transfer leading to reduced J_{sc} in Ag-TiO_2-60 and Ag-TiO_2-120 photoanodes.

The Nyquist plot (Fig. 10b) for Ag-TiO_2 photoanodes and bare TiO_2 photoanode fitted with the equivalent circuit exhibits semicircles corresponds to vital processes occurring at counter electrode, photoanode and electrolyte in DSSC. The first semicircle (R_1) in high frequency region symbolises charge transfer resistance at the counter electrode and the next semicircle (R_2) in the intermediate frequency region is associated with the dye sensitized photoanode/electrolyte interface resistance and third semicircle (R_3) corresponds to Warburg resistance related to the diffusion of the electrolyte [31].

The values of EIS parameters R_1, R_2 and R_3 have been listed in Table 3. From the values we observe that there is no significant change in R_1 and R_3 values as Ag NPs have practically a lesser role in charge transfer kinetics at counter electrode and diffusion of the redox electrolyte. However plasmonic effect is directly involved in the photoanode-dye/electrolyte interface, hence the value of R_2 is different for TiO_2 and Ag-TiO_2 photoanodes. The R_2 values increase for all the three Ag-TiO_2-30, 60 and 120 photoanodes indicating a reduction in back recombination due to less TiO_2–electrolyte interface. Among the Ag-TiO_2 photoanodes, the one with 30 min dipping time shows highest value and an increase in dipping time lowers R_2. Here, the magnitude of TiO_2-Ag, Ag-dye and dye-TiO_2 interfaces controls the charge transfer kinetics. An increase in dipping time minimizes the dye-TiO_2 interface and FRET (TiO_2 - Ag) dominates. This may cause a relative increase in dye-electrolyte interface and that triggers a recombination pathway for

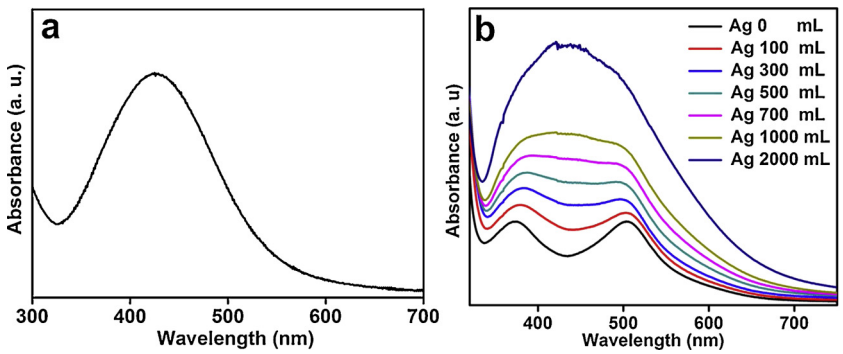

Fig. 5. Absorbance spectrum of (a) Ag NP (b) dye with increasing concentration of Ag NPs.

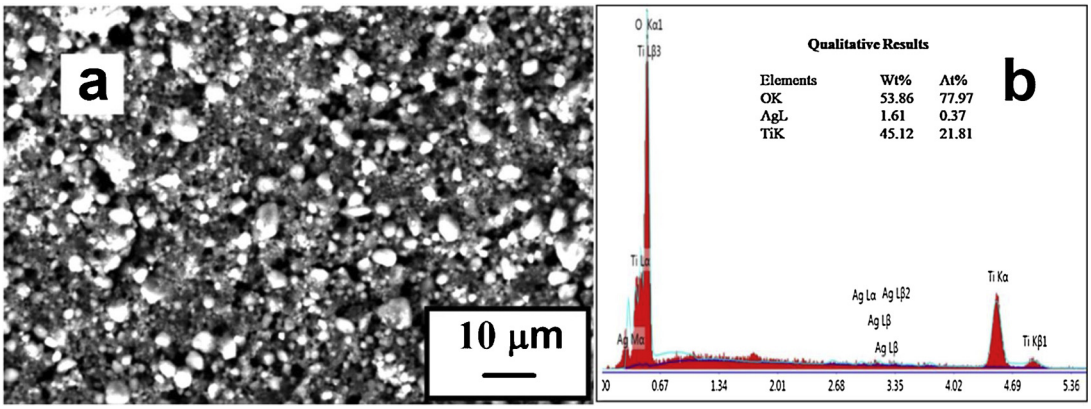

Fig. 6. (a) SEM image of Ag-TiO_2 photoanode (b) EDAX of Ag-TiO_2-30 photoanode.

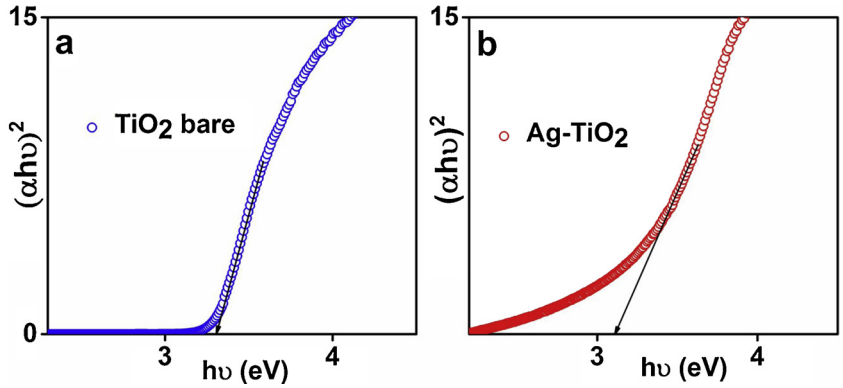

Fig. 7. Tauc plot of (a) TiO_2 (b) Ag-TiO_2 photoanode.

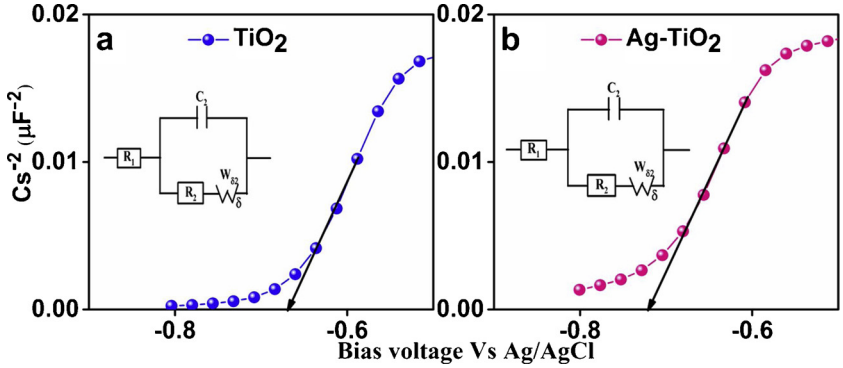

Fig. 8. Mott-Schottky plot of (a) TiO_2 (b) Ag-TiO_2.

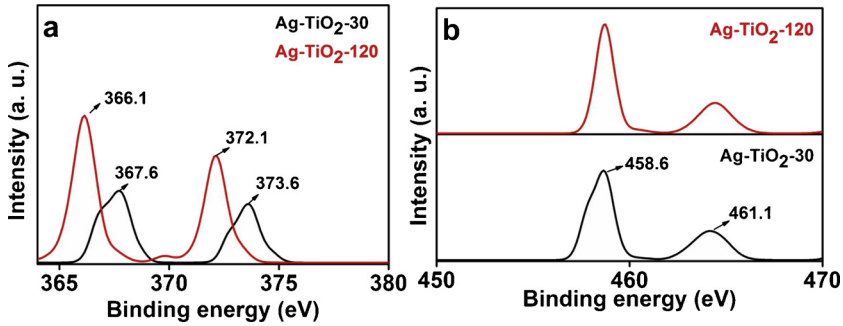

Fig. 9. XPS spectra of (a) Ag 3d and (b) Ti 2p.

Table 1
Surface atomic concentration determined from XPS.

Name of the sample	O1s atomic%	Ti 2p atomic%	Ag 3d atomic%
Ag-TiO_2-30	47.42	12.33	0.76
Ag-TiO_2-120	44.93	16.00	1.18

electrons from dye to electrolyte. This may be the reason why increased dipping time shows a lowering in R_2 value. The current voltage characteristics shown by photoelectrodes with different dipping time supports this assumption. Ag-TiO_2-30 is the optimum for exploiting the plasmonic effects along with minimising loss mechanisms at the photoanode. The increased electron transfer due to LSPR and reduced electron-hole recombination at the Ag-TiO_2-30 photoanode accounts for the high value of R_2 (23.9 Ω) as compared to R_2 (8.9 Ω) of bare TiO_2.

The stability studies (Fig. 11) of Ag-TiO_2-30 photoanode show decrease in efficiency over a period of 100 h, but Voc remains almost unchanged indicating the stability of the photoanode. The decrease in efficiency of the device with time could be due to corrosive effect of the electrolyte on dye and counter electrode leading to lesser photocurrent [32].

However decrease in efficiency with increase in dipping time can be attributed to the presence of excess Ag on the TiO_2 surface which may be oxidised and corroded by the electrolyte [33]. The excess of Ag in the TiO_2 film is quantified using XPS (Table 1) and EDAX spectra obtained for Ag-TiO_2-60 and Ag-TiO_2-120 (Fig. S2 in SI). The excess of Ag NP on the surface reduces the sensitization of the TiO_2 by the N719 dye by affecting the TiO_2-Dye interface, a vital parameter in light harvesting in DSSC. An alternate possible mechanism responsible for decrease in efficiency is associated with energy transfer which has been explained in this investigation.

PL studies are an indispensible tool in determining the charge transfer/recombination dynamics which are crucial in controlling the photoelectrical properties and hence performance of solar devices. The fate of the charge carriers (electron hole pairs) can be studied to a large extent as PL emissions arise from recombinations of free carriers. The PL emissions (Fig. 12a) show that the Ag-TiO_2 has diminished PL intensity compared to bare TiO_2. The PL emission of Ag-TiO_2 decreases with increase in dipping time from 30 to 120 min. The higher PL intensity of bare TiO_2 shows the rapid recombination of photogenerated charge carriers whereas a low PL emission indicates lesser electron-hole recombination favourable for improved charge transport. This lowering of PL intensity in Ag-TiO_2 is attributed to the formation of Schottky barrier at Ag and TiO_2 interface retarding the electron hole recombination processes [34]. In this investigation we unravel another possibility of reduced PL intensity due to the non-radiative energy transfer from TiO_2 to plasmonic metals (Silver in this case) due to FRET (Förster Resonance Energy Transfer) mechanism. FRET involves depletion of the excited state of the semiconductor due to the presence of metal in the vicinity leading to PL quenching [35]. The resonance energy transfer from TiO_2 to Ag NP is further justified by the overlap of

Table 2
Solar Cell performance using different Ag-TiO_2 photoanodes.

Sample	V_{oc} (V)	J_{sc} (mA/cm^2)	Fill Factor (FF) %	Efficiency η %
TiO_2	0.752	11.69	55.4	4.85
Ag-TiO_2-30	0.737	13.33	66.6	6.69
Ag-TiO_2-60	0.726	10.64	62.0	4.79
Ag-TiO_2-120	0.707	9.25	69.3	4.53

Table 3
Electrochemical Impedance (EIS) parameters of bare TiO_2 and Ag-TiO_2.

Sample	R_1 (ohm)	R_2 (ohm)	R_3 (ohm)
TiO_2	2.9	8.9	4.8
Ag-TiO_2-30	2.6	23.9	4.2
Ag-TiO_2-60	3.0	19.1	4.9
Ag-TiO_2-120	2.1	14.7	3.5

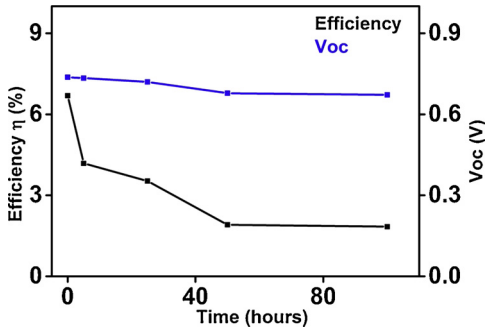

Fig. 11. Stability studies Ag-TiO_2 -30 photoanode.

emission spectrum of $TiO_2$with the Ag NP absorption spectrum as shown in Fig. 12(b). The Förster radius R_0 that is the distance at which probability of energy transfer is 50% is calculated using the standard equation [36].

$$R_0 = 0.211\,[k^2 n^{-4} Q_D J]^{1/6} \quad (1)$$

Where k^2 is the relative orientation of the dipoles of donor and acceptor in space and taken to be 2/3, n is the refractive index of the medium taken to be 1.4, Q_D is the quantum yield of TiO_2 (P25 Degussa) is 0.14 [37], J is the overlap integral between TiO_2 emission and Ag NP absorption. From the calculation using Eq. (1), R_0 is found to be 3.88 nm which is in the acceptable range of FRET mechanism of 1–10 nm [38].

Further evidence for FRET is provided by the lifetime measurements as shown in Fig. 13 to ratify the energy transfer from semiconducting nanoparticles (TiO_2) to Ag NP. Time correlated single photon counting (TCSPC) study was performed using a pulsed excitation of 370 nm. The time resolved fluorescence decay curves of bare TiO_2 and Ag-TiO_2 with various dipping times were measured. The red dots correspond to the

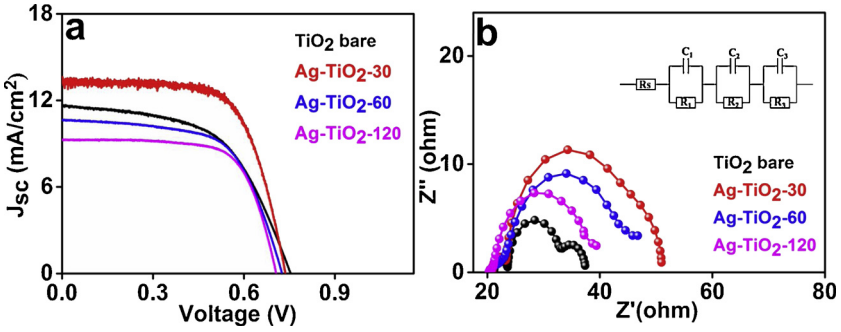

Fig. 10. (a) Current voltage curves (b) Nyquist plot of bare TiO_2 and Ag-TiO_2 with different dipping time.

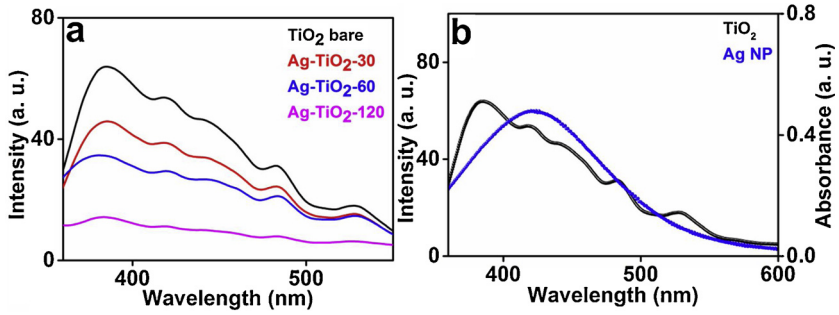

Fig. 12. (a) PL quenching with various dipping times (b) TiO_2–Ag Overlap curve.

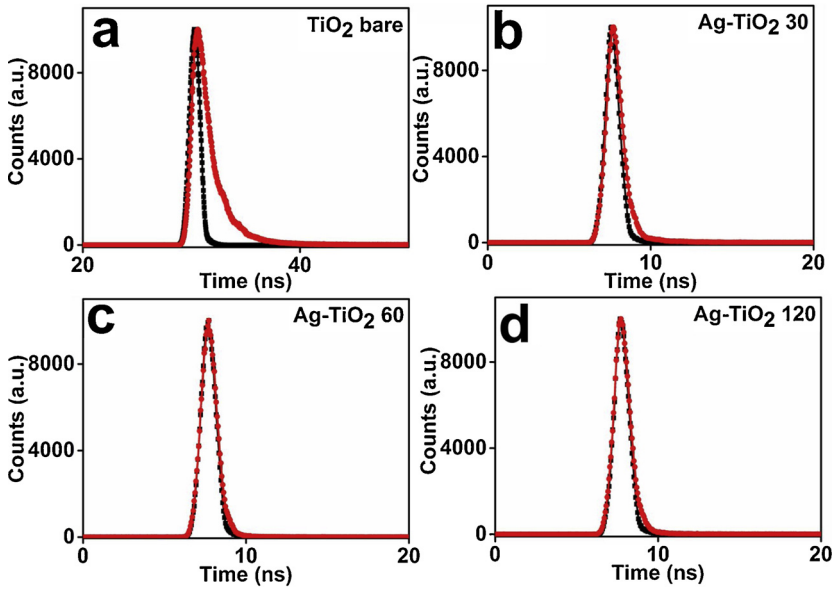

Fig. 13. Lifetime decay curve of (a) TiO_2 bare (b) Ag-TiO_2-30 (c) Ag-TiO_2-60 (d)Ag-TiO_2-120.

Table 4
Lifetimes and transfer efficiency table.

Sample	τ_{avg} (ns)	FRET efficiency (%)
Bare TiO_2	0.227	–
Ag- TiO_2-30	0.119	47.6
Ag- TiO_2-60	0.071	68.8
Ag- TiO_2-120	0.065	71.2

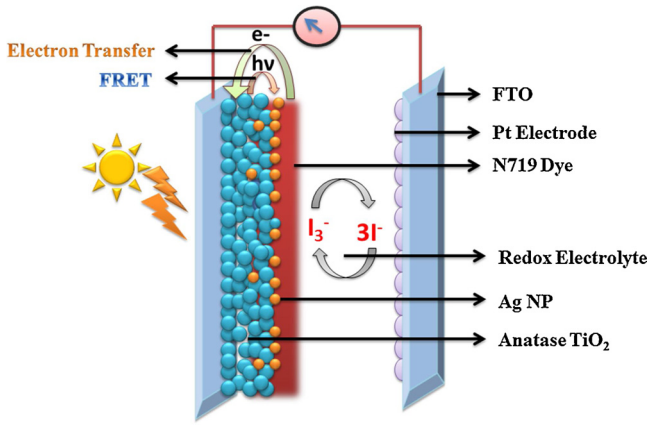

Scheme 1. Schematic illustration of working of Ag-TiO_2 photoanode DSSC.

decay and black dots correspond to the instrument response curve. The decay profiles were fitted with a two- exponential function as reported elsewhere [39].

$$I(t) = \alpha_1 \exp(-t/\tau_1) + \alpha_2 \exp(-t/\tau_2) \quad (2)$$

The obtained decay times have been presented in Table 4. The shortening of lifetime of the TiO_2 (in the presence of Ag NP) is a clear indication of FRET occurring between the donor –acceptor pair.

The FRET efficiency is calculated from the relative fluorescence lifetime of the donor (TiO_2) in the absence (τ_D) and presence (τ_{DA}) of the acceptor (Ag NPs) using the formula.

E= E= 1 − $\tau_{DA/\tau D}$ 1- (τ_{DA}) / (τ_D) where E is the efficiency of energy transfer.

The energy transfer efficiency increases with increase in dipping time of photoanode in Ag NP colloid which leads to increase in silver content in the photoanodeas shown in Fig. S2 in SI. This increase of acceptor concentration is responsible for the rise of transfer efficiency from 47.6 to 71.2% abiding by the basic characteristics of a FRET mechanism [40]. The working of the DSSC with a modified electrode along with charge and energy transfer mechanism has been presented in Scheme 1.

FRET is generally perceived as a loss mechanism in TiO_2-Ag hybrid structures [41–43]. Similarly quenching of fluorescent intensity of molecular probes in metal-fluroprobe hybrid systems via energy and electron transfer, being the major pathways, has been reported by Rahman et al [44]. In this work we have investigated the solar cell performance with respect to SPR effect of Ag NPs in Ag-Dye interface and energy transfer at TiO_2-Ag interface and observed their effect on

solar cell performance. At an optimum dipping time SPR effect dominates the scenario by generating enough electron hole pairs for strengthened solar to electricity conversion as seen in Ag-TiO_2-30.However as dipping time increases the amount of silver nanoparticles in the photoanode increases leading to more TiO_2-Ag NP interaction with energy transfer becoming dominant process over LSPR thereby reducing the efficiency of the cell.

4. Conclusion

Silver nanoparticles were synthesized using leaf extract of guava through a simple, a green protocol. The silver modified TiO_2 was used as photoanode in dye sensitized solar cell and its performance studied and analysed. The UV absorption studies, bandgap measurements, Mott-Schottky plots, current-voltage studies and PL spectra were used as characterization tools in this study. The nano silver was incorporated into the TiO_2 with dip coating method for 30 min, 60 min and 120 min. The optimised performance was attained by 30 min dipping of the bare TiO_2 photoanode. The Ag-TiO_2-30photoanode effectively improves the solar cell performance from 4.85% to 6.69%. The improvement is due to the enhanced current density J_{sc} from 11.69 to 13.33 mA/cm^2. The silver nanoparticles act as performance boosters by enhancing dye absorption in the visible region and suppressing loss mechanism by forming barrier at the semiconductor/ electrolyte interface. Finally the Ag-TiO_2 photoanode shows a decent stability above 100 h confirming the credibility of the device for commercial applications. This remarkable light harvesting by Ag-TiO_2photoanodeis credited to reduction in band gap, surface plasmon effect of silver nanoparticles and reduction in losses due to electron hole recombination, thereby emphasising its prospective role in low cost solar devices. At the same time resonance energy transfer with increasing silver nanoparticle colloid dipping plays a dominant role suppressing the efficiency of the solar cell. The interplay of electron and energy transfer with increased dipping time of silver nanoparticles has been explained using FRET parameters and lifetime measurements. The charge and energy transfer phenomena at the semiconductor-Ag NP-Dye photoanode interface lead to different solar light harvesting in the various hybrid structures. This complementary role of charge and energy transfer can be suitably optimised to get plasmonic solar cells with superior efficiencies in the near future.

Acknowledgements

Authors Rajita and Nijisha would like to acknowledge University Grants Commission (UGC), Government of India, for the support under Faculty Development Programme and research fellowship respectively. Authors Niveditha, Bhabhina and Sindhu acknowledge Council of Scientific and Industrial Research (CSIR) for research fellowship and funded project (No.03 (1285)/13/EMR-II). The authors would like to acknowledge Sophisticated Test and Instrumentation Centre (STIC), Cochin University of Science and Technology for TEM measurements and Sophisticated Analytical Instrument Facility (SAIF), IIT Madras for lifetime measurements. Amrita Centre for Nanosciences and Molecular Medicine (ACNSMM), Kochi is acknowledged for XPS analysis.

Appendix A. Supplementary data

Supplementary data associated with this article can be found, in the online version, at https://doi.org/10.1016/j.materresbull.2019.02.017.

References

[1] P.V. Kamat, Meeting the clean energy demand: nanostructure architechtures for solar energy conversion, J. Phys. Chem. C 111 (2007) 2834–2860.
[2] Michael Grätzel, Conversion of sunlight to electric power by nanocrystalline dye-sensitized solar cells, J. Photochem. Photobiol. A 164 (2004) 3–14.
[3] B.E. Hardin, H.J. Snaith, M.D. McGehee, The renaissance of dye-sensitized solar cells, Nat. Photonics 6 (2012) 162–169.
[4] S. Ito, T.N. Murakami, P. Comte, P. Liska, C. Grätzel, M.K. Nazeeruddin, M. Grätzel, Fabrication of thin film dye sensitized solar cells with solar to electric power conversion efficiency over 10%, Thin Solid Films 516 (2008) 4613–4619.
[5] S. Meng, E. Kaxiras, Electron and hole dynamics in dye-sensitized solar cells: influencing factors and systematic trends, Nano Lett. 10 (2010) 1238–1247.
[6] G. Calogero, P. Calandra, A. Irrera, A. Sinopoli, I. Citro, G. Di Marco, A new type of transparent and low cost counter-electrode based on platinum nanoparticles for dye-sensitized solar cells, Energy Environ. Sci. 4 (2011) 1838–1844.
[7] X. Dang, J. Qi, M.T. Klug, Po-Y. Chen, D.S. Yun, N.X. Fang, P.T. Hammond, A.M. Belcher, Tunable localized surface plasmon enabled broadband light harvesting enhancement for high-efficiency panchromatic dye-sensitized solar cells, Nano Lett. 13 (2013) 637–642.
[8] J.R. Cole, N.J. Halas, Optimized plasmonic nanoparticle distributions for solar spectrum harvesting, Appl. Phys. Lett. 89 (2006) 153120–153123.
[9] H.A. Atwater, A. Polman, Plasmonics for improved photovoltaics devices, Nat. Mater. 9 (2010) 205–212.
[10] N.C. Jeong, C. Prasittichai, J.T. Hupp, Photocurrent enhancement by surface plasmon resonance of silver nanoparticles in highly porous dye sensitized solar cells, Langmuir 27 (2011) 14609–14614.
[11] M. Ihara, K. Tanaka, K. Sakaki, I. Honma, K. Yamada, Enhancement of the absorption coefficient of ruthenium (II) dye in dye sensitized solar cells by a silver island film, J. Phys. Chem. B 101 (1997) 5153–5157.
[12] S. Sardar, S. Ghosh, H. Remita, P. Kar, B. Liu, C. Bhattacharya, P. Lemmens, S.K. Pal, Enhanced photovoltage in DSSC; synergistic combination of a silver modified TiO_2 photoanode and a low cost counter electrode, RSC Adv. 6 (2016) 33433–33442.
[13] S. Buda, S. Shafie, S.A. Rashid, H. Jaefer, N.F.M. Sharif, Enhanced visible light absorption and reduced charge recombination in AgNP plasmonic photoelectrochemical cell, Results Phys. 7 (2017) 2311–2316.
[14] K. Guo, M. Li, X. Fang, X. Liu, B. Sebu, Y. Zhu, Z. Hu, X. Zhao, Preparation and enhanced properties of dye sensitized solar cells by surface plasmon resonance of Ag nanoparticles in nanocomposite photoanode, J. Power Sources 230 (2013) 155–160.
[15] P. Nibelayim, G. Kawamura, W.K. Tan, H. Muto, A. Matsuda, Systematic characterisations of the effect of Ag@TiO_2 nanoparticles on the performance of plasmonic dye-sensitized solar cells, Sci. Rep. 7 (2017) 1–12.
[16] U.K. Parashar, V. Kumar, T. Bera, P.S. Saxena, G. Nath, S.K. Srivastava, R. Giri, A. Srivastava, Study of mechanism of enhanced antibacterial activity by green synthesis of silver nanoparticles, Nanotechnology 22 (2011) 1–13.
[17] R. Rajita, P. Nijisha, C.V. Niveditha, S. Sindhu, Natural dyes from red amaranth leaves as light harvesting pigments for dye sensitized solar cells, Mater. Res. Bull. 90 (2017) 156–161.
[18] L. Christensen, S. Vivekanandhan, M. Misra, A.K. Mohanty, Biosynthesis of silver nanoparticles using murrayakoenigii (curry leaf): an investigation on the effect of broth concentration in reduction mechanism and particle size, Adv. Mat. Lett. 2 (2011) 429–434.
[19] W.E. Erwin, H.F. Zarick, E.M. Talbert, R. Bardhan, Light trapping in mesoporous solar cells with plasmonic nanostructures, Energy Environ. Sci. 9 (2016) 1577–1601.
[20] W. Fan, M.K.H. Leung, Recent Development of plasmonic resonance-based photocatalysis and photovoltaics for solar utilization, Molecules 21 (2016) 1–26.
[21] J. Li, X. Chen, N. Ai, J. Hao, Q. Chen, S. Strawf, Y. Shi, Silver nanoparticle doped TiO_2 nanofiber dye sensitized solar cells, Chem. Phys. Lett. 514 (2011) 141–145.
[22] T. Solaiyammal, S. Muniyappan, B.G.T. Keerthana, S.S. Nemala, P. Bhargava, P. Murugakoothan, Green synthesis of Ag and the effect of Ag on the efficiency of TiO_2 based dye sensitized solar cell, J. Mater. Sci: Mater. Electron 28 (2017) 15423–15434.
[23] Y.H. Jang, Y.J. Jang, S.T. Kochuveedu, M. Byun, Z. Lin, D.H. Kim, Plasmonic dye-sensitized solar cells incorporated with Au-TiO_2 nanostructures with tailored configurations, Nanoscale 6 (2014) 1823–1832.
[24] S.U. Lim, A. Pandikumar, H.N. Lim, R. Ramraj, N.M. Huang, Boosting photovoltaic performance of dye sensitized solar cells using silver nanoparticle decorated N,S-Co-doped-TiO_2 photoanode, Sci. Rep. 11922 (2015) 1–14.
[25] N. Yao, J. Huang1, K. Fu, X. Deng, M. Ding, S. Zhang, X. Xu1, L. Li, Reduced interfacial recombination in dye-sensitized solar cells assisted with NiO:Eu3+,Tb3+ coated TiO_2 film, Sci. Rep. 6 (2016) 1–9.
[26] K.G. Deepa, P. Lekha, S. Sindhu, Efficiency enhancement in DSSC using metal nanoparticles: a size dependent study, Sol. Energy 86 (2012) 326–330.
[27] J. Du, J. Qi, D. Wang, Z. Tang, Facile synthesis of Au@TiO_2 core-shell hollow spheres for dye-sensitized solar cells with remarkably improved efficiency, Energy Environ. Sci. 5 (2012) (2012) 6914–6918.
[28] M.A.K.L. Dissannayake, J.M.K.W. Kumari, G.K.R. Senadera, C.A. Thotowatthage, Efficiency enhancement in plasmonic dye-sensitized solar cells with TiO_2photoanodes incorporating gold and silver nanoparticles, J. Appl. Electrochem. 46 (2016) 47–58.
[29] E. Diaz-de-Cero, V. Verardo, A.M.G. Caravaca, A.F. Gutierrez, A.G. Carretero, Determination of polar compounds in guava leaves infusions and ultrasound aqueous extract by HPLC-ESI-MS, J. Chem. 2015 (2015) 1–9.
[30] Z. Tian, L. Wang, L. Jia, Q. Li, Q. Song, S. Su, H. Yang, A novel biomass coated Ag–TiO_2 composite as a photoanode for enhanced photocurrent in dye sensitized solar cells, RSC Adv. 3 (2013) 6369–6376.
[31] Q. Wang, J.–E. Moser, M. Grätzel, Electrochemical impedance spectroscopic analysis of dye-sensitized solar Cells, J. Phys. Chem. B 109 (2005) 14945–14953.
[32] G. Boschloo, A. Hagfeldt, Characteristics of the iodine/triodide redox mediator in dye-sensitized solar cells, Acc. Chem. Res. 42 (2009) 1819–1826.
[33] S.P. Lim, A. Pandikumar, N.M. Huang, H.N. Lim, Enhanced photovoltaic performance of silver@titania plasmonic photoanode in dye-sensitized solar cells, RSC

Adv. 4 (2014) 38111–38118.
[34] S.P. Lim, A. Pandikumar, N.M. Huang, H.N. Lim, G. Gu, T.L. Ma, Promotional effect of silver nanoparticles on the performance of N-doped TiO_2 photoanode based dye sensitized solar cells, RSC Adv. 4 (2014) 48236–48244.
[35] J. Chen, S. Shen, P. Guo, M. Wang, J. Su, D. Zhao, L. Guob, Plasmonic Ag@SiO_2 core/shell structure modified g-C_3N_4 with enhanced visible light photocatalytic activity, J. Mater. Res. 29 (2014) 64–70.
[36] S. Sardar, P. Kar, H. Remita, B. Liu, P. Lemmens, S.K. Pal, S. Ghosh, Enhanced charge separation and FRET at heterojunctions between semiconducting nanoparticles and conducting polymer nanofibers for efficient solar light harvesting, Sci. Rep. 5 (2015) 1–14.
[37] M. Lunz, A.L. Bradley, Concentration dependence of Förster resonant energy transfer between donor and acceptor nanocrystal quantum dot layers: effect of donor-donor interactions, Phys. Rev. B 83 (2011) 1–10.
[38] Suparna Sadhu, Krishna Kanta Haldar, Amitava Patra, Size dependent resonance energy transfer between semiconductor quantum dots and dye using FRET and kinetic model, J. Phys. Chem. C 114 (2010) 3891–3897.
[39] N. Serpone, A. Salinaro, Terminology, relative photonic efficiencies and quantum yields in heterogeneous photocatalysis. Part I: Suggested protocol, Pure Appl. Chem. 71 (1999) 303–320.
[40] L. Dworak, V.V. Matylitsky, T. Ren, T. Bashe, T. Wachtveit, Acceptor concentration dependence of förster resonance energy transfer dynamics in dye-quantum dot complexes, J. Phys. Chem. C 118 (2014) 4396–4402.
[41] J. Zhou, F. Ren, S. Zhang, W. Wu, X. Xa, Y. Liu, C. Jiang, SiO_2–Ag-SiO_2-TiO_2 multi-shell structures: plasmon enhanced photocatalysis with wide spectral response, J. Mater. Chem. A 1 (2013) 13128–13138.
[42] D.B. Ingram, S. Linic, Water splitting on composite plasmon – metal/semiconductor photoelectrodes: evidence for selective plasmon induced formation of charge carriers near the semiconductor surface, J. Am. Chem. Soc. 133 (2011) 5202–5205.
[43] E. Liu, L. Kang, Y. Yang, T. Sun, X. Hu, C. Zhu, H. Liu, Q. Wang, X. Li, J. Fan, Plasmonic Ag deposited TiO_2 nano-sheet film for enhanced photo-catalytic hydrogen production by water splitting, Nanotechnology 25 (2014) 1–10.
[44] Dewan S. Rahman, Sanhita Deb, Sujit Kumar Ghosh, Relativity of electron and energy transfer contributions in nanoparticle-induced fluorescence quenching, J. Phys. Chem. C119 (2015) 27145–27155.

Materials Research Express

PAPER

Metal photocatalysis by red and black nano-gold colloids: a rational design through green pathway

Materials Research Express

RECEIVED
5 January 2019

REVISED
16 April 2019

ACCEPTED FOR PUBLICATION
29 April 2019

PUBLISHED
10 May 2019

PAPER

Metal photocatalysis by red and black nano-gold colloids: a rational design through green pathway

Rajita Ramanarayanan, Bhabhina Ninnora Meethal, Nijisha Pullanjiyot, Niveditha C V and Sindhu Swaminathan

Department of Nanoscience & Technology, University of Calicut, Kerala- 673635, India

E-mail: sindhus@uoc.ac.in

Keywords: black gold, induced aggregation, nanostructures, self-assembly

Abstract

The unique electronic and chemical property of colloidal gold nanoparticles in aqueous solution is being extensively studied for the development of new generation nanoscale devices. In this work, gold colloids of different colour, morphology and size were synthesized using leaf extract of guava (*Psidium guajava*) under ambient conditions. The role of leaf extract of *Psidium guajava* as a reducing, stabilising and aggregation inducing agent was explored in this study. Two different coloured gold colloids, red and black, were formed with increasing the leaf extract concentration. The red coloured colloids are monodisperse whereas black colloids showed aggregate structures in TEM analysis. Black coloured gold aggregates show broadband absorption due to interparticle plasmonic coupling. In addition to this, the near field enhancement contributed by these colloidal aggregates generates high energy electrons and promote intra-band transition. These properties are responsible for the improved optical and photocatalytic behaviour shown by the black gold colloids compared to monodispersed red gold colloids. Bio-inspired gold aggregates by this fast and green approach is suitable for various sensing and optoelectronic applications. The synthesis strategy, characterization and photocatalytic application of nanoscale gold particles self-assembled into an aggregate structure has been discussed in this work.

1. Introduction

The synthesis of coloured gold colloids has fascinated human mind and captured the attention of the scientific community due to its extremely appealing nature [1]. Gold nanoparticles have shown tremendous application in catalysis, biotechnology, medicine, industry and solar cells because of their unique optical, electrical and catalytic properties [2]. To utilise and optimise the various physical and chemical properties it is necessary to control theirshape, size, structure, composition and dielectric environment [3, 4].

The plasmonic gold nanoparticles (AuNPs) characterized by their strong interaction with resonant photons due to surface plasmon resonance (SPR) have seen a burst of research activity in the area of synthesis and functionalization of nanoparticles to get desired structures with novel functionalities [5]. Due to these versatile properties, colloidal solutions of gold have different colours in visible spectrum depending on their respective sizes, shapes and morphologies.

The ruby red colour symbolised colloidal gold solutions containing uncoagulated particles with diameters less than 40 nm supported by a sharp absorption band around 530 nm [6]. SPR peak could be systematically tuned by changing the size and structure of AuNPs which could be used to design unique nanostructures that interact with the entire solar spectrum. An important development in this regard is assembly of nanoparticles into aggregates of different shapes and sizes by employing various strategies like *insitu* formation of gold aggregates and induced formation of already formed gold nanoparticles by external agents [7–12]. Further, black coloured stable gold nanoparticles have been reported by Liu *et al* [13] which show broadband absorption and interesting 3D morphology synthesized using reverse emulsion system. The highlight of this paper is the rarely

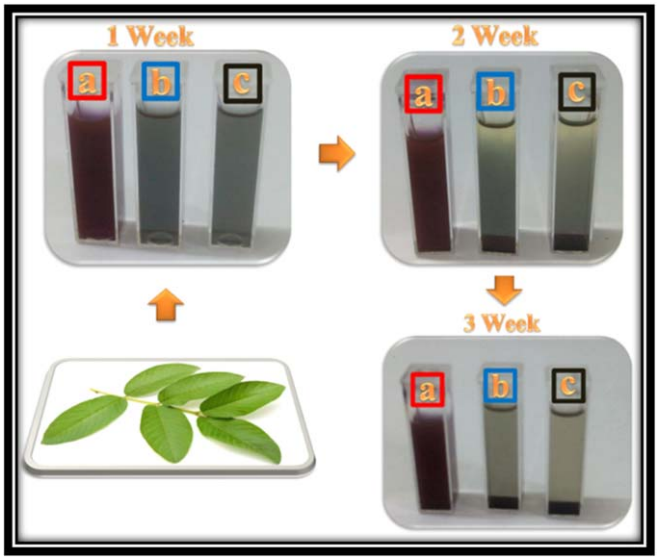

Figure 1. Guava leaf and synthesised gold nanoparticles (a) Au1 (b) Au2 (c) Au3.

reported synthesis of black gold colloid using green chemistry approach. In the recent times green chemistry methods have been used extensively used for the synthesis of metal nanoparticles because of their eco-friendly approach [14–16]. Inspite of many reports on green synthesis of gold nanoparticles [17–21] there is plenty of scope for research owing to the rich biodiversity of plants. The increase in size of gold nanoparticles by changing the concentration of reducing agent has been reported previously using tri-sodium citrate [22]. The multiple role of leaf extract of *Psidium guajava* as a reducing, stabilising and aggregation inducing agent has been explored in this investigation.

Psidium guajava, the common guava belonging to Myrtaceae, is a small tree widely cultivated in tropical and subtropical regions around the world. It is a popular fruit grown in most of the parts of India. The guava leaves are rich source of phytochemicals and have been explored for bio-inspired synthesis of metal nanoparticles [23]. This paper reports a very fast synthesis (almost instantaneous) of monodisperse red gold nanoparticles and black gold aggregates with a simple lab procedure having high rate of reproducibility and reliability for large scale productions in future.

2. Experimental section

2.1. Materials and methods

The fresh mature leaves of guava were washed, cut into small pieces and dried in air for some time to remove excess of water. Leaf extract was prepared by boiling and stirring the leaves in distilled water following the same procedure as reported in our previous work [24]. 1 mM of $HAuCl_4$ (Sigma-Aldrich) was used as precursor solution for nanoparticle synthesis.

For synthesis of gold nanoparticles 1 ml (Au1), 2 ml (Au2) and 3 ml (Au3) of extract were added to 3 ml of 1 mM of $HAuCl_4$ solution and stirred for two minutes at room temperature to ensure uniform mixing. The instant colour change of the pale yellow gold salt solution implies the formation of gold nanoparticles.The sample Au1 shows reddish pink colour whereas samples Au2 and Au3 show black colour indicating variation from Au1 (figure 1).

To study photocatalytic activity, 1 ml of gold nanoparticle solution was added to 20 ml of 20 ppm Methylene Blue (MB) dye in distilled water. The mixture was stirred under dark condition to reach absorption-desorption equilibrium for 10 min After reaching the equilibrium, about 4 ml of the dye solution was taken to study the decrease in MB concentration by monitoring the principal peak intensity using a UV–vis Spectrophotometer. Then the mixture is illuminated by 300 W Xenon lamp and the concentration of the dye is monitored after 30 and 60 min.

2.2. Characterisation of gold nanoparticles

The UV–vis spectrophotometer (T90, PG Instruments) was used to measure the nature of absorbance of the nanoparticles due to surface plasmon resonance (SPR) in the visible range of the solar spectrum. Fourier transforms infrared spectra (FTIR) of leaf extracts and different gold nanoparticles were measured using

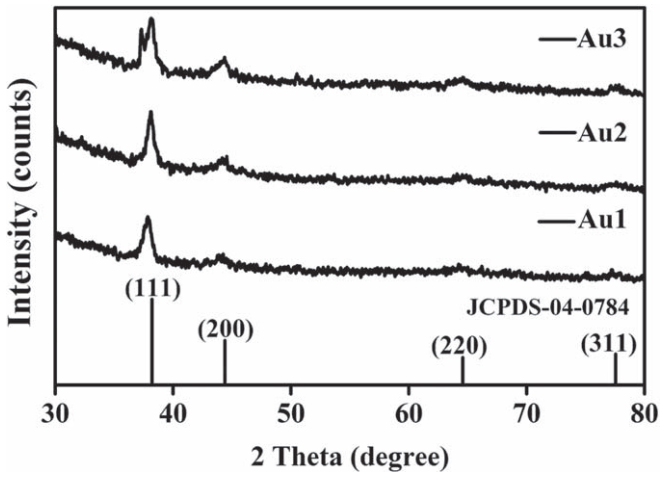

Figure 2. XRD of gold colloids drop-casted on glass substrate.

PerkinElmer Spectrum Two FTIR spectrometerin the wavenumber range of 4000–450 cm^{-1}. X-ray diffraction (XRD) measurements were performed using Rigaku Miniplex–x Ray diffractometer with monochromatic Cu-Kα radiation ($\lambda = 1.54$ Å), scanned in the 2θ range of 30° to 80. The size of the synthesized nanoparticles was determined by transmission electron microscopy (TEM) Jeol/ JEM 2100 using LaB6 source operated at 200 kV. Dynamic light scattering (DLS) measurements were conducted using Malvern (Nano-S90) for size distribution of the colloidal systems. The fluorescent measurements were conducted using PerkinElmer (LS55) in the visible range. The photocatalytic measurements were conducted using photocatalytic reactor (LZCX-XE) using 300 W Xenon Lamp.

3. Results and discussion

3.1. XRD measurements

Structure and crystallinity of Au nanoparticles are confirmed using XRD measurements by dropcasting them on a glass substrate. The diffraction peaks can be indexed to the (111), (200), (220) and (311) reflections of the cubic structure of the metallic gold, confirming its crystalline structure (figure 2). The minor peaks (200) and (311) are not clear due to the amorphous nature of the glass substrate.

The biomass residues present in the guava leaf extract are responsible for the extra peak at 38° in Au3 sample [25]. From the XRD measurements, crystallite size (D) was found using Debye–Scherrer formula

$$D = 0.9\lambda/\beta \text{ Cos } \theta \quad (1)$$

where λ is the wavelength of x-ray radiation, β is the full width at half maximum and θ is the Bragg angle. The crystallite size calculated for the samples vary from 11.6 nm to 13.7 nm for Au1, Au2 and Au3 due to the difference in size/shape of the samples.

3.2. TEM and DLS measurements

In order to identify the effect of concentration of reducing agent on the size of Au NPs, TEM images (figure 3) were obtained along with the SAED pattern. The presence of bright circular rings in SAED pattern corresponds to various crystal planes of face centric cubic structure of gold nanoparticles implying the polycrystalline nature [26]. The Au1NPs showed well separated quasi-spherical sized particles with an outer coating due to the biomolecules of the reducing agent adsorbed onto the gold surface. Consequently the organic layer acts as a barrier providing electrostatic repulsion and a steric hindrance between Au NPs thus preventing individual particles from coagulating. The closer view shows about 4–5 nanoparticles in each nanostructure in Au2 and about 10–15 nanoparticles in each aggregate of Au3. The individual nanoparticles in the aggregate are smaller than Au1 nanoparticles (figure 4(a)). The increase in reducing agent causes decrease in size of individual nanoparticles which is in agreement with the literature available on green synthesis of gold nanoparticles [27]. There is almost no gap between adjacent particles which indicates that there is a strong cross-linking interaction directing the nanoparticles into self-assembled aggregates.

The DLS measurements reveal the hydrodynamic diameters of AuNPs and aggregates (figure 4(b)). The DLS diameters are usually bigger than TEM data but give an idea of the distribution. The Au1 colloid shows a narrow

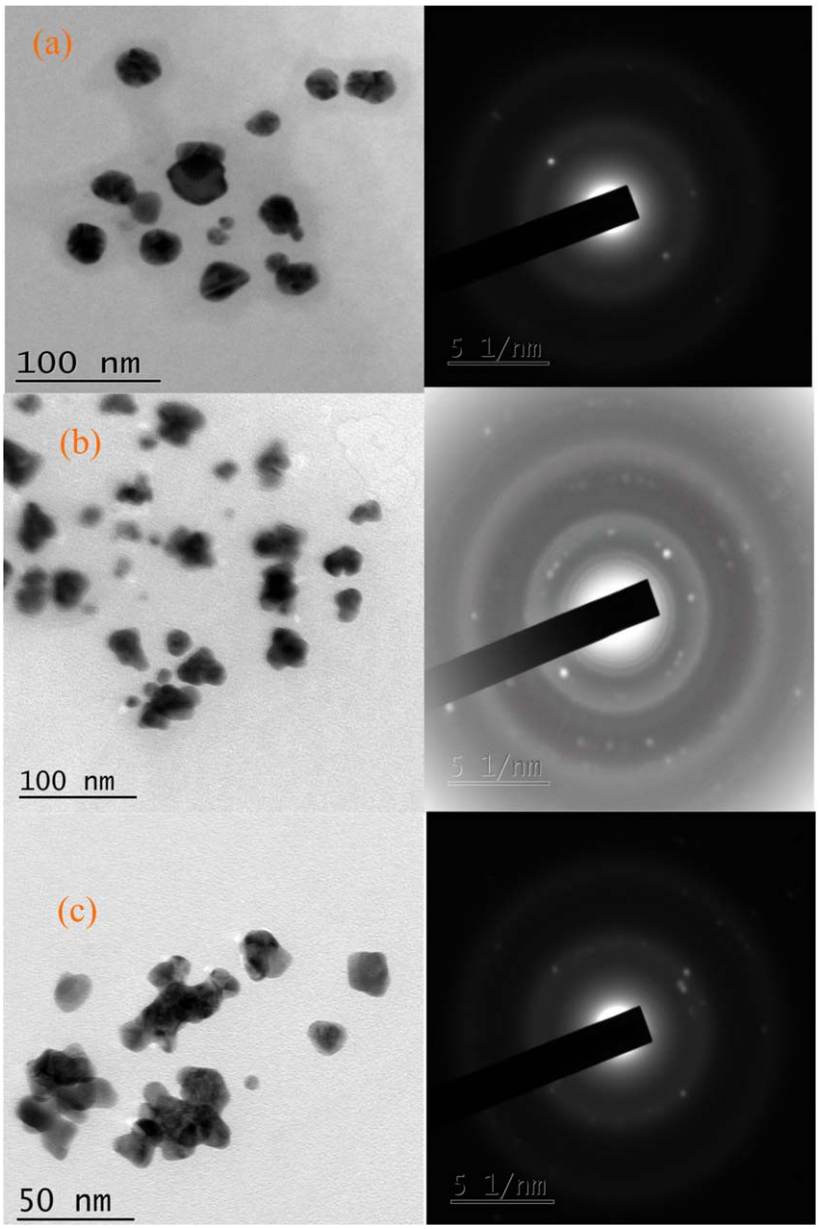

Figure 3. TEM images and SAED pattern of (a) Au1 (b)Au2 (c) Au3.

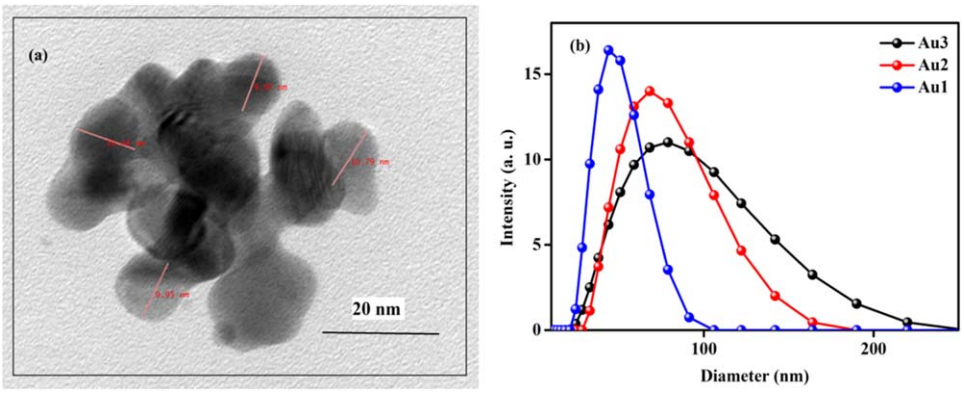

Figure 4. (a) Aggregate structure of Au3 (b) DLS size distribution of Au 1, Au2, Au3.

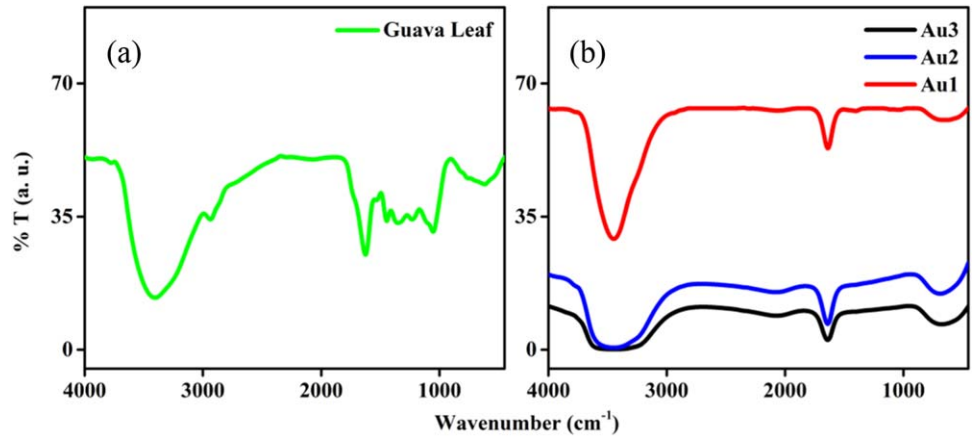

Figure 5. FTIR spectra of (a) Guava leaf extract (b) Au1, Au2 and Au3.

Table 1. Comparison on the sizes obtained from DLS and TEM with Au concentration in Au1, Au2 and Au3.

Name	Concentration in mol L^{-1}	Hydrodynamic size from DLS (nm)	Average size from TEM images (nm)
Au 1	$4.47 \times^{\circ} 10^{-7}$	43	26.2
Au 2	$1.12 \times^{\circ} 10^{-7}$	49	38.6
Au 3	$3.80 \times^{\circ} 10^{-8}$	59	52.7

distribution indicating mono-disperse particles of similar sizes. The distribution broadens gradually for Au2 and Au3, as size increases from isolated nanoparticles to self-assembled aggregates.

The concentration of nanoparticles in solution was obtained using a method reported by Liu *et al* [28]. The average number of gold atoms per nanoparticle was calculated using the equation

$$N = 0.523\frac{\rho D^3}{M.} \tag{2}$$

where, ρ and M correspond to the density of fcc gold and atomic mass respectively. D is the average size of the nanoparticle obtained from TEM measurements (table 1). Substituting N in the equation below, the molar concentration of the nanoparticle solution is estimated.

$$C = \frac{N_{tot}}{N\ V\ N_a} \tag{3}$$

where N_{tot} and N_a corresponds to the total number of gold salt present in the solution and Avogadro number respectively. V is the volume of the reaction solution. The concentration of the samples Au1, Au2, Au3 have been shown in table 1.

Comparison of DLS and TEM size measurements show DLS size higher than TEM size for all the three samples. The variation of the average size of Au3 is minimal whereas Au1 shows a marked variation from the DLS measurements. DLS is an intensity dependent measurement where hydrodynamic radius varies with the polydispersity, solvent nature and close proximity of the nanoparticles. The higher concentration of Au1 could be the possible reason of more nanoparticles lying close to each other affecting the accuracy of DLS measurement.

3.3. FTIR measurements

The FTIR spectra of the guava leaf extract and of the synthesized Au NPs have been shown in figure 6. FTIR peaks at 3422 (OH), 2927(OH), 1619 (C=O), 1221 and 1063 (C–O) and 611(R–CH) cm^{-1}represent the various functional groups present in the guava extract (figure 5(a)). The synthesized Au NPs show peaks at 3449 (OH), 1640 (C=O), 1036 (C–O) and 666 (R–CH) cm^{-1}corresponding to different peaks present with the extract after reduction. The binding of carboxylic moiety to the nanoparticle surface is expressed by the disappearance of the band at 2927 cm^{-1} in figure 5(b) corresponding to OH stretching vibration of carboxylic group. In both FTIR spectra the OH peak at around 3100–3400 cm^{-1} is dominant due to the presence of OH groups in gallic acid, flavonoids and eugenol present in the extract of guava leaf [29, 30]. In the case of mono-disperse Au1 gold nanoparticles, the peak is sharper due to the consumption of OH groups in the reduction process. The broad

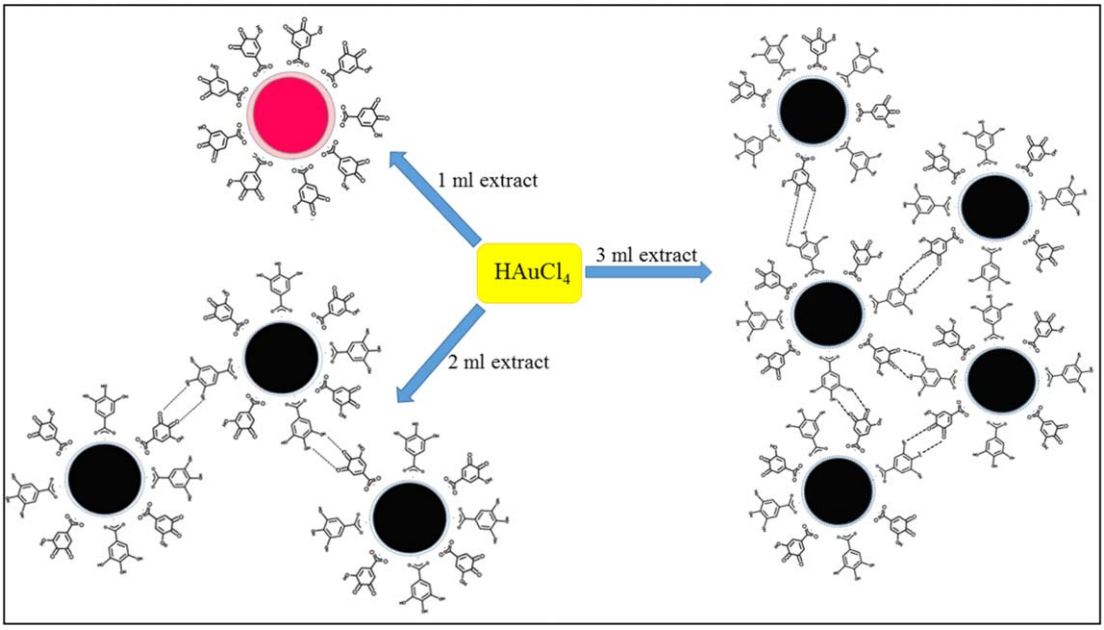

Figure 6. Schematic of self-assembled Au nanostructures through hydrogen bonding of the capping agent.

absorption band in 3100–3400 cm^{-1} in Au2 and Au3 could be due to the intermolecular hydrogen bonded network of phenolic groups present on the surface of the nanoparticle.

On the basis of FTIR analysis a mechanism is being proposed for the self-assembly of gold nanoparticles. The phytochemicals gallic acid and quercetin (flavonoid) are reported to show aggregation of Au NPs when their quantity as reducing agent is increased [31, 32]. Both of these phytochemicals contain hydroxyl and carboxyl groups responsible for hydrogen bonding with similar groups of the adjacent molecules. Here the hydroxyl groups in the gallic acid are presumed to take part in the reduction of gold ions to metallic gold by undergoing oxidation to its quinine analogue and the carboxylic acid bind to the surface of the Au nanoparticles by taking the role of a capping agent to keep the system stabilized. The gold nanoparticles generally will have surface functional groups yielding a negative charge resulting in repulsive inter-particle forces ensuring colloidal stability. In the case of Au1, the decrease in pH of the medium (from pH 5 of the extract to pH 3 of the colloid) shows that most of the gallic acid underwent two electron oxidation to corresponding quinone form yielding better stability. With further addition of the extract both gallic acid and its quinone form co-exists in the solution. The strong intermolecular and intra-molecular hydrogen bonding between these two are likely to be responsible for the formation of aggregates and consequently lesser stability of Au2 and Au3. In the schematic diagram (figure 6) Au1 has been shown capped by quinone form but Au2 and Au3 is represented using both quinone and gallic acid and the hydrogen bonding has been depicted. Thus at higher concentration of the extract the repulsive forces decreases, inter-particle distance becomes narrower through hydrogen bonding to form self-assembled aggregates. A similar work, where increase in capping agent causing formation of aggregated nanostructures has been reported by Sen *et al* [33]. The capping agent in that work was MPA and colour of aggregated nanostructures was light blue. As guava leaf is rich in various phytochemicals, we are able to obtain unique black coloured gold aggregates due to the synergetic effect of the reducing and capping agents present in the leaf extract. The proposed model is further justified as the size of the aggregates increases with increased concentration of the extract.

3.4. Optical studies

The reduction of precursor salt can be visually assessed by the instant change of colour from pale yellow precursor solution to red or black depending on the concentration of plant extract added. The formation of nanoparticles was confirmed from UV–vis absorbance spectrum (figure 7(a)) as it is a conventional method to probe the stability,surface chemistry and aggregation behaviour of the AuNPs formed. The monodispersed Au1 nanoparticles exhibit a well defined sharp peak around 539 nm showing good agreement with the reported SPR band of Au NP [34].

Broad peaks with reduced intensity had been observed with increasing extract quantity indicating the formation of aggregates in solution. The dense organic molecules present in the extract adsorbed on the surface of Au NPs significantly change the interface conditions leading to a sharp decrease in the intensity of SPR

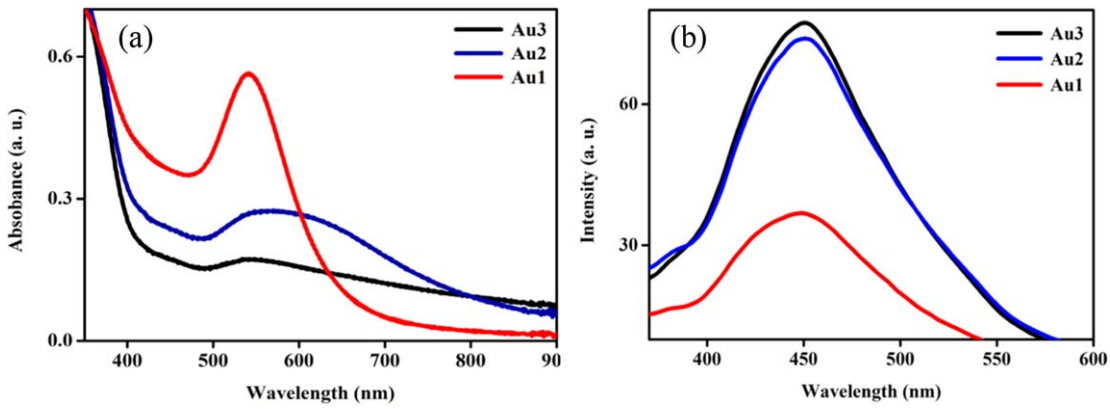

Figure 7. (a) UV–vis spectra of the gold colloids (b) PL spectra of Au1, Au2 and Au3 colloids.

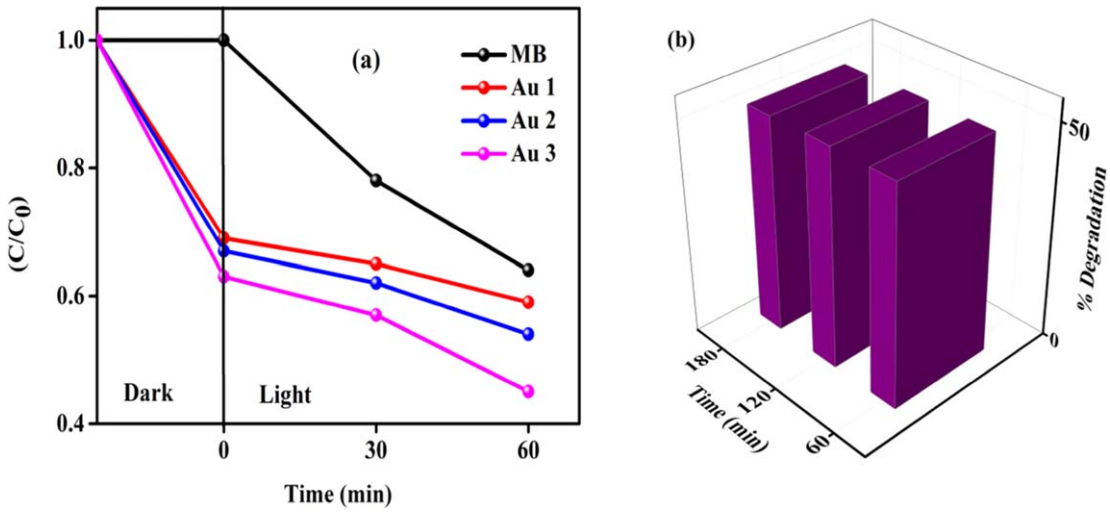

Figure 8. (a) Photocatalytic activity of Au1, Au2 and Au3 colloids and (b) Reuse study of best sample Au3.

absorption. The broadening in SPR is due to the damping of the SPR caused by the combined effect of increase in particle size and shape of Au NPs in colloidal solutions. The formation of gold particle assembly leads to an increase in dielectric constant of the surrounding medium, hence shifting the plasmon peak to a lower energy [35].The Au1 shows very good stability for few weeks and Au2 and Au3 show stability for a week at room temperature, but they are stable for a longer period when kept at 4 °C.

The PL studies conducted at an excitation wavelength of 340 nm showed that all the Au colloids were found to be luminescent in the visible range showing peak around 450 nm (figure 7(b)). The luminescent emission of guava extract in the above range is likely to responsible for the fluorescent emission of the gold colloids.The aggregates, Au2 and Au3 showed higher PL emission when compared to monodisperse Au1. Thefluorescent properties of the gold colloids can be exploited as nanosensor, detectors and as fluorescent probe in cancer cell imaging applications [36–38].

3.5. Photocatalytic studies

To understand the photocatalytic activity of the gold colloids, degradation of MB dye, the plot of C/C_0 versus time was drawn as shown in figure 8 where C_0 is the initial concentration and C is the concentration of MB dye at regular intervals. The self-degradation is observed in pure MB dye under illumination due to the presence of dissolved oxygen in water [39] . Further it is seen that Au3 nanoparticles degrade MB dye to about 55% after 60 min as compared to 47% for Au2 and 41% for Au1 nanoparticles. There are previous reports on dye degradation by metal nanoparticles synthesized using green protocol which have used spherical nanoparticles as electron relay between Sodium borohydride and dyes for faster degradation [40–42]. Similarly there are reports using only nanoparticles for dye degradation similar to our report [43–45]. However our investigation shows

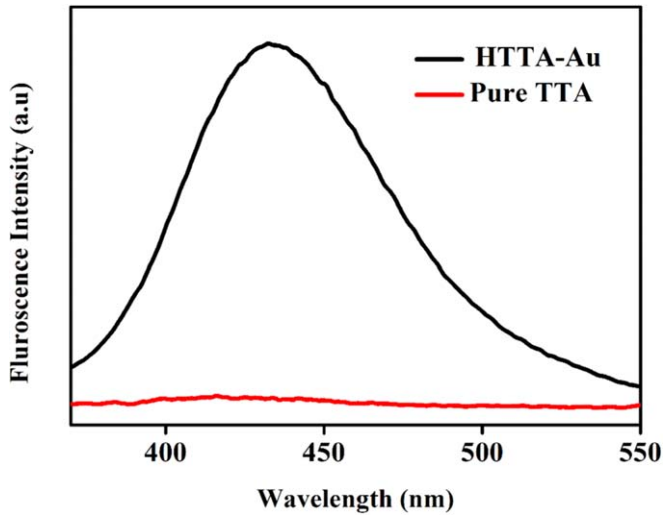

Figure 9. Graph showing formation of hydroxyl radicals in TTA in the presence of light upon addition of gold nanoparticles.

Table 2. Comparison of degradation times of methylene blue dye using gold nanoparticles.

Sample	Catalytic efficiency	References
Au-HaP (gold hydroxyapatite) nanocomposite	15% MB degraded in 100 min	[49]
Biosynthesized Au nanoparticles with sodium borohydride as catalyst.	85% MB degraded in 40 min	[50]
Sodium dodecyl sulfate (SDS) Au nanoparticles	75.3% MB degraded in 8 h	[51]
Black gold nanoaggregates	55% MB degraded in 60 min	Present work

good photoresponse within 1 h for pure metal nanoparticles due to the presence of superstructures as compared to previous works with a very low concentration of the photocatalyst used for degradation. The gold aggregates synthesized in this work exhibit better photocatalytic behaviour compared to monodisperse red colloids. In monodisperse noble metal nanoparticles electron-hole pairs are generated due to Surface Plasmon Resonance (SPR), but are insufficient enough to promote photocatalysis properly due to their high recombination rates compared to semiconductors. But this scenario can be improved by designing plasmonic superstructures/ aggregates with good light harvesting properties due to their special properties like near field enhancement and broadband absorption spectra compared to isolated particles. The close proximity of gold nanoparticles in an aggregate is responsible for strong broadband absorption due to Plasmon Resonance coupling thereby improving the light harvesting of Au2 and Au3 aggregates. Further, the near field enhancement increases photon flux many fold in a small area prompting highly energetic electrons undergoing intra-band transitions above the Fermi level simultaneously generating vacant states below Fermi level. These excited electrons along with the holes generated react with the adsorbed methylene blue dye molecules to drive catalytic reactions [46, 47].

Among the aggregates, Au3 with the lowest concentration of nanoparticles in solution shows the highest activity which may be due to having more exposed surfaces compared to Au2 in agreement with the previous reports [48].

The stability or reusability of the photocatalyst is a deciding factor to test its possibility in commercial applications. The time dependent stability studies observed through three consecutive cycles showed good stability and nearly same photocatalytic efficiency for Au3 as shown in figure 8(b). A comparative study of gold nanoparticles utilised for the degradation of MB dye by various groups has been presented in table 2. It is seen that in the current study, the best sample Au3 shows good performance as catalyst in the absence of sodium borohydride in the degradation of MB dye.

The quantification of reactive oxygen species generated is done using a fluorescent probe method. Terephthalic acid (TTA), a non-fluorescent probe molecule, is used to estimate the formation of hydroxyl radicals. TTA on addition with photocatalyst is converted into 2-hydroxy terephthalate (HTTA) radicals which exhibits fluorescence indicating the presence of hydroxyl radicals [39]. This is confirmed from the photoluminescence (PL) study, where TTA exhibits high PL emission after being exposed to light in the presence of gold nanoparticles (figure 9).

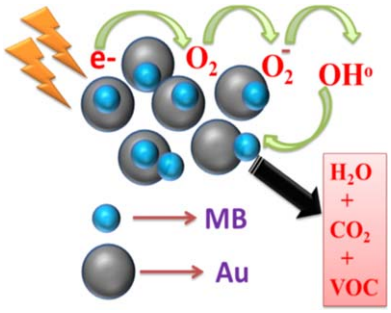

Figure 10. Scheme of photocatalytic degradation of MB dye on Au3 surface.

The scheme of the photocatalysis mechanism is shown in figure 10. The light induced surface plasmons excite the electrons on the metal surface to higher energy levels. These excited energetic electrons react with oxygen molecules in the dye solution to form superoxide radicals which further converted into hydroxyl radicals as follows.

$$e^- + O_2 \rightarrow O_2^-$$
$$O_2^- + HO_2^\circ + H^+ \rightarrow H_2O_2 + O_2$$
$$H_2O_2 \rightarrow 2OH^\circ$$

These hydroxyl radicals are highly reactive oxygen species and degrade the MB dye to water, carbon dioxide and volatile organic compounds (VOC). The quantification of these hydroxyl free radicals using terephthalic acid probe molecules confirms its presence (figure 9).

4. Conclusions

An environment friendly, green approach has been used to synthesize red and black gold colloids with different size and morphologies using the leaf extract of guava tree. The phytochemicals present in the extract acts as a reducing, capping and aggregation inducing agent for the gold nanostructures in the red and black colloids. At lower extract concentration red colloids with near spherical particles around 20–30 nm are obtained. But as the concentration of leaf extract is increased, black colloids having aggregates composed of sizes between 40–60 nm are formed. The colour change that occurs from aggregation leads to varied optical properties offering possibilities for diverse applications in optoelectronics. At lower extract concentration most of the gallic acid is oxidized to its quinone form by reducing the gold ions to form stable red colloids. Formation of black gold aggregates at high extract concentration is contributed by the strong intermolecular and intra-molecular hydrogen bonding between gallic acid and its quinone present in the medium. The use of green technology in water purification has been demonstrated through photocatalytic degradation of Methylene Blue dye by nanomolar concentrations of gold colloids. Tunability of various physical and optical properties by varying the size and shape of metallic colloids are likely to open up new directions in several domains of current research and technologies.

Acknowledgments

Rajita and Nijisha would like to acknowledge University Grants Commission (UGC), Government of India, for the support under Faculty Development Programme and research fellowship respectively. Bhabhina, Niveditha and Sindhu acknowledge Council of Scientific and Industrial Research (CSIR) for research fellowship and funded project (No.03 (1285)/13/EMR-II).The authors acknowledge Sophisticated Test and Instrumentation Centre (STIC) Cochin University of Science and Technology (CUSAT) for TEM analysis.

ORCID iDs

Sindhu Swaminathan https://orcid.org/0000-0002-9197-7508

References

[1] Turkevich J, Stevenson P C and Hiller J 1951 A study of the nucleation and growth processes in the synthesis of colloidal gold *Discuss. Faraday Soc.* **11** 55–75
[2] Ghosh S K and Pal T 2007 Inter-particle coupling effect on the surface plasmon resonance of gold nanoparticles: from theory to applications *Chem. Rev.* **107** 4797–862
[3] Kelly K L, Coronado E, Zhao L L and Schatz G C 2003 The optical properties of metal nanoparticles: the influence of size, shape and dielectric environment *J. Phy. Chem.* **107** 668–77
[4] Jain P K, Lee K S, El-Sayed I H and El-Sayed M A 2006 Calculated absorption and scattering properties of gold nanoparticles of different size, shape and composition: application in biological imaging and medicine *J. Phys. Chem.* B **110** 7239–48
[5] Gambinossi F, Mylon S E and Ferri J K 2015 Aggregation kinetics and colloidal stability of functionalized nanoparticles *Adv. Colloid Interface Sci.* **222** 332–49
[6] Turkevich J 1985 Colloidal gold. part 2 *Gold Bull.* **18** 125–31
[7] Westcott S L, Oldenburg S J, Lee T R and Halas N J 1999 Construction of simple gold aggregates with controlled plasmon—plasmon interactions *Chem. Phys. Lett.* **300** 651–5
[8] Chegel Y, Rachkov O, Lopatynsk A, Ishihava S, Yanchuk I, Nemoto Y, Hill J P and Ariga K 2012 Gold nanoparticles aggregation ;drastic effect of cooperative functionalities in a single molecule conjugate *J. Phys. Chem.* C **116** 2683–90
[9] Yang C, Sui H, Li X, Han J, Luo X, Zhang X, Sun H, Sun H C, Zhou Y and Yang B 2013 Gold nanoparticle superstructures with enhanced photothermal effect *Cryst Eng. Comm.* **15** 3490–7
[10] Chen C C, Kuo P L and Cheng Y C 2009 Spherical aggregates composed of gold nanoparticles *Nanotechnology* **20** 1–7
[11] Raliya R and Biswas P 2015 Environmentally benign bio-inspired synthesis of Au nanoparticles, their self-assembly and agglomeration *RSC Adv.* **5** 42081–7
[12] Liao J, Zhang Y, Yu W, Xu L, Ge C, Liu J and Gu N 2003 Linear aggregation of gold nanoparticles in ethanol *Colloids Surf.* A **223** 117–83
[13] Liu D, Zhou F, Li C, Zhang T, Zhang H, Cai W and Li Y 2015 Black gold: plasmonic colloidosomes with broadband absorption self-assembled from monodispersed gold nanospheres by using a reverse emulsion system *Angew. Chem. Int. Ed.* **54** 9596–600
[14] Akhtar M S, Panwar J and Yun Y S 2013 Biogenic synthesis of metallic nanoparticles by plant extracts *ACS Sustainable Chem. Eng.* **1** 591–602
[15] Mittal A K, Chisti Y and Banerjee U C 2013 Synthesis of metallic nanoparticles using plant extract *Biotechnol. Adv.* **31** 346–56
[16] Sharma V K, Yngard R A and Lin Y 2009 Silver nanoparticles: green synthesis and their antimicrobial activities *Adv. Colloid Interface Sci.* **145** 83–96
[17] Smitha S L, Philip D and Gopchandran K G 2009 Green synthesis of gold nanoparticles using *Cinnamomum zeylanicum* leaf broth spectrochim *Acta A Mol Biomol. Spectrosc.* **74** 735–9
[18] Sadaghi B, Mohammadzadeh M and Babakhani B 2015 Green synthesis of gold nanoparticles using *Stevia rebaudiana* leaf extracts: characterization and their stability *J. Photochem. Photobiol. B Biol.* **148** 101–6
[19] Kasthuri J, Veerapandian S and Rajendiran N 2009 Biological synthesis of silver and gold nanoparticles using apiin as reducing agent colloids and surf *B Biointerfaces* **68** 55–60
[20] Tamuly C, Hazarika M, Ch Borah S, Das M R and Boruah M P 2013 *In situ* biosynthesis of Ag, Au and bimetallic nanoparticles using piper pedicellatum C.DC: green chemistry approach *Colloids and Surf. B Biointerfaces* **102** 627–34
[21] Stankus D P, Lohse S E, Hutchison J E and Nason J A 2011 Interactions between natural organic matter and gold nanoparticles stabilized with different organic capping agents *Environ. Sci. Technol.* **45** 3238–44
[22] Ji X, Song X, Li J, Bai Y, Yang W and Peng X 2007 Size control of gold nanocrystals in citrate reduction: the third role of citrate *J. Am. Chem. Soc.* **129** 13939–48
[23] Raghunandan D, Basavaraja S, Mahesh B, Balaji S, Manjunath S Y and Venkataraman A 2009 Biosynthesis of stable polyshaped gold nanoparticles from microwave-exposed aqueous extracellular anti-malignant guava (Psidium guajava) leaf extract *Nano Biotechnol.* **5** 34–41
[24] Rajita R, Nijisha P, Nivedita C V and Sindhu S 2017 Natural dyes from red amaranth leaves as light harvesting pigments for dye sensitized solar cells *Mater. Res. Bull.* **90** 156–61
[25] Gurunathan S, Raman J, Malek S N A, John P A and Vigenswary S 2013 Green synthesis of silver nanoparticles using *Ganoderma neo-japonicum* Imazeki: a potential cytotoxic agent against breast cancer cells *Int. J. Nanomedicine* **8** 4399–413
[26] Ndeh N T, Maensiri S and Maensiri D 2017 The effect of green synthesized gold nanoparticles on rice germination and roots *Adv. Nat. Sci.: Nanosci. Nanotechnol.* **8** 035008–017
[27] Huang X, Wu H, Liao X and Shi B 2010 One-step, size controlled synthesis of gold nanoparticles at room temperature using plant tannin *Green Chem.* **12** 395–9
[28] Liu X, Atwater M, Wang J and Huo Q 2007 Extinction coefficient of gold nanoparicles with different sizes and different capping agents colloids and surf *B Biointerfaces.* **58** 3–7
[29] Parashar U K, Kumar V, Bera T, Saxena P S, Nath G, Srivastava S K, Giri R and Srivastava A 2011 Study of mechanism of enhanced antibacterial activity by green synthesis of silver nanoparticles *Nanotechnology* **22** 1–13
[30] Diaz-de-Cero E, Verardo V, Caravaca A M G, Gutierrez A F and Carretero A G 2015 Determination of polar compounds in guava leaves infusions and ultrasound aqueous extract by HPLC-ESI-MS *J. Chem* **2015** 1–9
[31] Yoosaf K, Ipe B I, Suresh C H and Thomas K G 2007 *In situ* synthesis of metal nanoparticles and selective naked eye detection of lead ions from aqueous media *J. Phys. Chem.* C **111** 12839–47
[32] Rawat K A and Kailasa S K 2014 Visual detection of arginine, histidine and lysine using quercetin functionalized gold nanoparticles *Microchim. Acta* **181** 1917–29
[33] Sen T and Patra A 2009 Formation of self-assembled Au nanoparticles and the study of their optical properties by steady state and time resolved spectroscopies *J. Phys. Chem.* C **113** 13125–32
[34] Shankar S, Jaiswal L, Aparna R S L and Prasad R G S V 2014 Synthesis, characterization,*in vitro* biocompatibility and antimicrobial activity of gold, silver and gold silver alloy nanoparticles prepared from lansium domesticum fruit peel extract *Mater. Lett.* **137** 75–8
[35] Galleto P, Brevet P F, Girault H H, Antoine R and Broyer M 1999 Enhancement of the second harmonic response by adsorbates on gold colloids: the effect of aggregation *J. Phys. Chem.* B **103** 8706–10
[36] Zhang J, Zhou C, Yu M and Liu J 2012 Different sized luminescent gold nanoparticles *Nanoscale* **4** 4073–83
[37] Huang C C, Yang Z, Lee K H and Chang H T 2007 Synthesis of highly fluorescent gold nanoparticles for sensing mercury(II) *Angew. Chem. Int. Ed.* **46** 6824–8

[38] He H, Xie C and Ren J 2008 Non-bleaching fluorescence of gold nanoparticles and its applications in cancer cell imaging *Anal. Chem.* **80** 5951–7
[39] Bhabhina N M, Rajita R and Sindhu S 2018 Surface modification of oxygen-deficient ZnO nanotubes by interstitially incorporated carbon: a superior photocatalytic platform for sustainable water and surface treatments *Appl. Nanosci.* **8** 1545–555
[40] Vidhu V K and Philip D 2014 Catalytic degradation of organic dyes using biosynthesized silver nanoparticles *Micron* **56** 54–62
[41] Umamaheswari C, Lakshmanan A and Nagarajan N S 2018 Green synthesis, characterization and catalytic degradation studies of gold nanoparticles against congo red and methyl orange *J. Photochem. Photobiol.* C **178** 33–9
[42] Nakkala J R, Mata R, Raja K, Chandra V K and Sadras S R 2018 Green synthesized silver nanoparticles: catalytic dye degradation, *in vitro* anti-cancer activity and *in vivo* toxicity in rats *Mater. Sci. Eng.* C **91** 372–81
[43] Vanaja M, Paulkumar K, Baburaja M, Rajeshkumar S, Gnanagobitha G, Malarkodi C, Sivakavinesan M and Annadurai G 2014 Degradation of methylene blue using biologically synthesized silver nanoparticles *Bioinorg. Chem. Appl.* **2014** 1–8
[44] Selvam G G and Sivakumar K 2015 Phycosynthesis of silver nanoparticles and photocatalytic degradation of methyl orange dye using silver (Ag) nanoparticles synthesized from Hypnea musciformis (Wulfen) J.V.Lamouroux *Appl. Nanosci* **5** 617–22
[45] Jyothi K and Ajeet S 2016 Green synthesis of nanostructured silver particles and their catalytic application in dye degradation *J. Gen. Engg. Bio.* **14** 311–7
[46] Ke S, Kan C, Liu J and Cong B 2013 Controlled assembly of gold nanorods using tetrahydrofuran *RSC Adv.* **3** 2690–6
[47] Christopher P, Xin H and Linic S 2011 Visible light enhanced catalytic oxidation reactions on silver plasmonic nanostructures *Nature Chem.* **3** 467–72
[48] Yang J, Li Y, Zu L, Tang L, Liu G, Qin Y and Shi D 2015 Light concentrating plasmonic Au superstructures with significantly visible light enhanced catalytic performance *ACS Appl. Mater. Interfaces* **7** 8200–8
[49] Mondal S, Reyes M E D A and Pal U 2017 Plasmon induced enhanced photocatalytic activity of gold loaded hydroxyapatite nanoparticles for methylene blue degradation under visible light *RSC Adv.* **7** 8633–45
[50] Mata R, Bhaskaran A and Sadras S R 2015 Green-synthesized gold nanoparticles from Plumeria alba flower extract to augment catalytic degradation of organic dyes and inhibit bacterial growth *Particuology* 1–9
[51] Kumar B and Cumbal L 2014 SDS coated gold nanocatalyst for degradation of methylene blue IX congreso de *Ciencia Y Tecnología Espe* 59–62 ISSN: 1390-4663